EXPERIMENTAL AND ANALYTICAL INVESTIGATION OF THREE-DIMENSIONAL INVISCID EFFECTS IN TURBOMACHINERY

PENNSYLVANIA STATE UNIVERSITY

PREPARED FOR
NAVAL SEA SYSTEMS COMMAND

22 MAY 1974

EXPERIMENTAL AND ANALYTICAL INVESTIGATION OF THREE-DIMENSIONAL INVISCID EFFECTS IN TURBOMACHINERY

Robert W. Howells, Jr.

Technical Memorandum
File No. TM 74-161
May 22, 1974
Contract No. N00017-73-C-1418

Copy No. 6

The Pennsylvania State University
Institute for Science and Engineering
APPLIED RESEARCH LABORATORY
Post Office Box 30
State College, PA 16801

NAVY DEPARTMENT

NAVAL SEA SYSTEMS COMMAND

REPORT DOCUMENTATION PAGE

READ INSTRUCTIONS
BEFORE COMPLETING FORM

1. REPORT NUMBER
TM 74-161

2. GOVT ACCESSION NO.

3. RECIPIENT'S CATALOG NUMBER

4. TITLE (and Subtitle)
EXPERIMENTAL AND ANALYTICAL INVESTIGATION OF THREE-DIMENSIONAL INVISCID EFFECTS IN TURBOMACHINERY

5. TYPE OF REPORT & PERIOD COVERED
M.S. Thesis, May 1976

6. PERFORMING ORG. REPORT NUMBER
TM 74-161

7. AUTHOR(s)
Robert W. Howells, Jr.

8. CONTRACT OR GRANT NUMBER(s)
N00017-73-C-1418

9. PERFORMING ORGANIZATION NAME AND ADDRESS
The Pennsylvania State University
Applied Research Laboratory
P. O. Box 30, State College, PA 16801

10. PROGRAM ELEMENT, PROJECT, TASK AREA & WORK UNIT NUMBERS

11. CONTROLLING OFFICE NAME AND ADDRESS
Naval Sea Systems Command
Department of the Navy
Washington, D. C. 20362

12. REPORT DATE
May 22, 1974

13. NUMBER OF PAGES
159 pages & figures

14. MONITORING AGENCY NAME & ADDRESS (if different from Controlling Office)

15. SECURITY CLASS. (of this report)
Unclassified, Unlimited

15a. DECLASSIFICATION DOWNGRADING SCHEDULE

16. DISTRIBUTION STATEMENT (of this Report)

Approved for public release, distribution unlimited, per NSSC (Naval Sea Systems Command), 6/12/74.

17. DISTRIBUTION STATEMENT (of the abstract entered in Block 20, if different from Report)

18. SUPPLEMENTARY NOTES

ANALYTICAL INVESTIGATION	POTENTIAL FLOW
BLADE GEOMETRY	ROTOR
INVISCID EFFECTS	THREE-DIMENSIONAL EFFECTS
LIFTING SURFACE	TURBOMACHINERY

19. KEY WORDS (Continue on reverse side if necessary and identify by block number)

20 ABSTRACT (Continue on reverse side if necessary and identify by block number)

A relatively simple, rapid method for predicting the three-dimensional flow effects in turbomachinery of arbitrary configuration was investigated. Although the two-dimensional cascade is a satisfactory approximation for the design and analysis of some types of turbomachines, the flow through devices such as propeller pumps, inducers, and fans for turbofan engines may deviate significantly. No solution exists for the complete, unified three-dimensional flow problem, but analyses which include the effect of three-dimensional

DD FORM 1 JAN 73 1473 EDITION OF 1 NOV 65 IS OBSOLETE

20. **ABSTRACT** (continued)

flows have been developed. These typically involve lengthy numerical solutions for specialized cases and are not optimum for design nor for a unified study of three-dimensional flow trends.

A three-dimensional lifting surface theory was used to predict the potential flow around blades, represented by line vortices and sources, spanning an annulus. Other investigators have generally assumed arbitrary singularity distributions; representation of an actual blade geometry by the model is unique here.

A rotor was designed, built, and tested (with air as the test medium) for comparison with the theory. Three unique features mark the experiment. Static pressure distributions on a rotating blade were measured. The effect of blade dihedral on these pressures was also measured. Instrumentation using a pressure transducer in the rotating system was designed and built.

Deviation from cascade predictions caused by the three-dimensional flow effects is found to be significant for some turbomachines such as propeller pumps. No theory was developed, but variation of the experimental blade pressure distributions caused by dihedral was found to be considerable. These results are important for their direct effect on performance as well as for their secondary effect, for example on the boundary layer.

ACKNOWLEDGMENTS

The author wishes to express his appreciation to Dr. B. Lakshminarayana, Professor of Aerospace Engineering, for his guidance throughout this work. Special thanks are also due to many of the employees of the Applied Research Laboratory for their help on various aspects of the experimental program, which was carried out at the Garfield Thomas Water Tunnel. George Gurney was helpful in the instrumentation development and Mark McBride in blade manufacture.

The research reported herein was sponsored by the Applied Research Laboratory (ARL) of The Pennsylvania State University, which operates under contract with the U.S. Naval Sea Systems Command.

TABLE OF CONTENTS

TABLE OF CONTENTS (continued)

LIST OF TABLES

LIST OF FIGURES

LIST OF FIGURES (continued)

LIST OF FIGURES (continued)

LIST OF FIGURES (continued)

LIST OF FIGURES (continued)

LIST OF SYMBOLS

$A_{j,p}$	constants used to specify radial variation of a source line
B	blade span
C	blade chord length
CF	centrifugal force
C_L	section lift coefficient (based on inlet dynamic head $\frac{1}{2}\rho W_1^2$)
C_{PT}	total pressure coefficient
C_{PTL}, C'_{PTL}	measured total pressure losses in the AFRF
C_p, C_{ps}	blade static pressure coefficient $[(p - p_\infty)/\frac{1}{2}\rho W_1^2]$
C/S	solidity of blade row
C_t	tip clearance
C'_t	normalized tip clearance ($= C_t/B$)
c	non-dimensional blade chord length (C/r_T)
F_v, F_s	factors defined by Equations (3) and (6), respectively
f_c	a function which specifies camber line coordinate
$G_{\ell,j}$	influence coefficient for unit vortex (Equation 20)
H	Head rise
$\underline{i}$	unit vector in angular direction
J_m	the m-th order Bessel function of the first kind
JVS	the number of singularities (source or vortex) per blade
$\underline{j}$	unit vector in radial direction
K_{mn}, K_{kn}	the n-th eigen value corresponding to the m-th (or k-th) order Bessel function
k	an integer multiple of the number of blades ($k = \ell \cdot NB$)
$\underline{k}$	unit vector axial direction
LE	leading edge
ℓ	any integer variable, calculation points

LIST OF SYMBOLS (continued)

m	the order of a Bessel function
m_L	the largest value of m for which the eigen value is estimated within 1% accuracy by the polynomial approximation
m_{LAST}	the maximum value of m to be calculated
NB	the number of blades
n	the number of an eigen value
n_{LAST}	the maximum value of n to be calculated
P	the degree of the polynomial which specifies the radial variation of a source line
p	blade static pressure
P_∞	ambient pressure
P_c	centrifugally induced pressure
P_{01}	pressure on axis of rotation of AFRF
P_{02}	a known reference pressure
P_{SB}	static pressure on a blade at a specified orifice
P_{S_∞}	static pressure upstream of blade row
P_{TB}	total pressure on a blade referred to the relative frame
Q, Q_j	non-dimensional strength of a radial source line (normalized by $1/r_T W_1$)
q	local non-dimensional source strength for a continuous source distribution (normalized by $1/r_T W_1$)
Re	Reynold's number based on local chord length
r	radial position coordinate
S	spacing between blades ($2\pi r/NB$)
$S_{\ell,j}$	influence coefficient for unit source (Equation 22)
t	trailing edge
$\underline{U}$	non-dimensional induced perturbation velocity vector ($iu_\theta + \underline{j}u_\eta + \underline{k}u_\zeta$)

LIST OF SYMBOLS (continued)

u	component of the non-dimensional perturbation velocity vector
$\underline{V}$	non-dimensional resultant absolute velocity vector
v	component of non-dimensional resultant velocity vector
V_B	local velocity relative to the blade
V_{REF}	reference velocity for AFRF
$\underline{V}_\infty$	local free stream inlet velocity vector
$\underline{W}_m$	non-dimensional cascade mean velocity vector (normalized by $1/W_1$)
W_1	inlet relative velocity
w	non-dimensional component of cascade mean velocity vector
x	axial position coordinate
Y_m	the m-th order Bessel function of the second kind
y	tangential position coordinate ($= r\theta$)
Z_m, Z_k	a factor defined by Equation 4
α_I	angle of incidence (between chord line and inlet velocity vector)
Γ, Γ_j	non-dimensional strength of a radial vortex line (normalized by $1/r_T W_1$)
γ	local non-dimensional vortex strength for a continuous vorticity distribution (normalized by $1/r_T W_1$)
ζ	non-dimensional axial position coordinate (x/r_T)
ζ_j	the axial position of the j-th vortex (same for each blade i)
η	non-dimensional radial position coordinate (r/r_T)
θ	angular or tangential position coordinate (radians)
$\theta_{i,j}$	the angular position coordinate of the j-th vortex representing the i-th blade
λ	stagger angle (measured between C and ζ, Figure 1)
μ	dihedral angle (Figure 53)
ν	hub/tip radius ratio (r_H/r_T)

LIST OF SYMBOLS (continued)

ξ	non-dimensional chordwise position coordinate ($\xi = [\zeta^2+(\eta\theta)^2]^{1/2}$)
ρ	density of the fluid
ϕ_v, ϕ_s	velocity potential due to a series of radial vortex lines and source lines respectively (non-dimensional)
ϕ	flow coefficient ($V_\zeta/\omega r_T$)
ψ	blade loading coefficient ($gH/\Omega^2 r^2$)
$\bar{\psi}$	mass averaged (hub to tip) loading coefficient ψ
Ω, ω	rotational speed of the blades (radians/sec)

Superscripts

'	first derivative
*	refers to the continuous singularity modification of the three-dimensional theory
$\overline{\ }$	refers to the location of a centroid of the area under a singularity distribution plot

Subscripts

H	refers to the blade hub
i	refers to the i-th blade
j	refers to the j-th singularity for any blade
ℓ	specifies the calculation points on a profile surface
M	refers to mid-radius of blade
m	refers to the m-th order Bessel function
n	refers to the n-th eigen value
s	refers to a source or source system
T	refers to the blade tip
v	refers to a vortex or vortex system

LIST OF SYMBOLS (continued)

Subscripts (continued)

x, ζ	refers to the axial direction
η	refers to the radial direction
θ	refers to the angular, or tangential direction
$(\ )_2$	refers to a two-dimensional theory
$(\ )_3$	refers to the three-dimensional theory

ABSTRACT

A relatively simple, rapid method for predicting the three-dimensional flow effects in turbomachinery of arbitrary configuration was investigated. Although the two-dimensional cascade is a satisfactory approximation for the design and analysis of some types of turbomachines, the flow through devices such as propeller pumps, inducers, and fans for turbofan engines may deviate significantly. No solution exists for the complete, unified three-dimensional flow problem, but analyses which include the effect of three-dimensional flows have been developed. These typically involve lengthy numerical solutions for specialized cases and are not optimum for design nor for a unified study of three-dimensional flow trends.

A three-dimensional lifting surface theory was used to predict the potential flow around blades, represented by line vortices and sources, spanning an annulus. Other investigators have generally assumed arbitrary singularity distributions; representation of an actual blade geometry by the model is unique here.

A rotor was designed, built, and tested (with air as the test medium) for comparison with the theory. Three unique features mark the experiment. Static pressure distributions on a rotating blade were measured. The effect of blade dihedral on these pressures was also measured. Instrumentation using a pressure transducer in the rotating system was designed and built.

Deviation from cascade predictions caused by the three-dimensional flow effects is found to be significant for some turbomachines such as propeller pumps. No theory was developed, but variation of the

experimental blade pressure distributions caused by dihedral was found to be considerable. These results are important for their direct effect on performance as well as for their secondary effect, for example, on the boundary layer.

CHAPTER I

INTRODUCTION

1.1 Statement of the Problem

The flow through an axial turbomachine is always three-dimensional to some degree. However, since no unified theory for predicting the complete three-dimensional flow through a turbomachine exists, practical methods of design and analysis presently rely heavily upon two-dimensional approximate techniques. Generally, a description of the mean flow is obtained by a two-dimensional inviscid theory such as potential flow analysis. Corrections to this flow may be applied to account for other effects such as viscosity, finite hub/tip ratio and other three-dimensional flows. However, when a turbomachine blade designed by two-dimensional methods is operated in a three-dimensional annular flow field, the actual performance of the blade differs from the design specifications. If the three-dimensional effects are small, a simplified two-dimensional approximation may be adequate; in many turbomachines the three-dimensional effects cannot be neglected, and no comprehensive method for design or analysis exists.

Large three-dimensional effects occur, for example, in turbomachinery such as marine propellers, rocket pump inducers, and turbofan engine fans. Such devices typically have a few blades of high solidity, a low hub/tip ratio, and large stagger angles. Furthermore, the chord may be comparable to the hub diameter and the blades may overlap. Thus, the effects due to hub and annulus walls and interference between radial locations may be large. When the flow is highly three-dimensional, blade performance is expected to deviate significantly from two-dimensional predictions. Morelli and Bowerman (1) have shown that for a single-bladed propeller pump the discrepancy between the experimentally measured and two-dimensional theoretical pressure distribution was considerable.

The inviscid three-dimensional effects arise from constraints due to hub and annulus walls; radially varying blade loading; radial variation in blade blockage; dihedral, sweep and twist of the blade, etc. In addition, viscous effects induce three-dimensionality in the flow. These are caused by blade boundary layer, secondary flow and annulus wall boundary layer. In order to meet the demands for more efficient turbomachinery blading operating with higher loading and to predict performance more accurately, the fundamental details of the three-dimensional flow through a turbomachine must be better understood. The present work has been limited to an investigation of the three-dimensional potential flow in axial turbomachinery. Specifically, the differences between the predictions of two-dimensional and three-dimensional theories and the influence of machine configuration have been considered. The objective of this thesis is to predict the extent of the three-dimensional inviscid effects and to verify them experimentally.

In some turbomachinery blade rows, especially in liquid handling machinery, the blade elements are designed to have dihedral (analogous to dihedral in aircraft wings) for hydrodynamic reasons (e.g. cavitation). Dihedral may also arise from the design and manufacturing considerations due to blade twist and stack up of the blade sections. Since there has been little investigation of the effect of blade dihedral, experimental measurements for blades with dihedral were conducted. Although no mathematical theory was developed to describe the effect of dihedral, a qualitative discussion and interpretation of data for blades with dihedral has been included. The variation of experimental blade pressure distribution caused by dihedral is found to be considerable.

1.2 Background and Summary of Previous Work

1.2.1 Two-Dimensional Theory. The types of two-dimensional analyses for the flow through a turbomachine may be classified as blade-to blade, meridional plane, and channel methods. Referring to the cylindrical coordinate system shown in Figure 1, these analyses calculate the flow properties on surfaces approximately parallel to the plane formed by the ζ and θ axes, the ζ and η axes, and the θ and η axes, respectively. In each analysis, the flow calculated on any given two-dimensional surface is assumed to be independent of the flow on any other similar surface. Generally, these analyses are inviscid and irrotational.

An example of a blade-to-blade analysis is the two-dimensional rectilinear cascade, or strip theory approximation. Assuming that the stream surfaces through a blade row are concentric cylinders of constant radius, the intersection of any cylinder with the blade row may be developed into a plane in which the blade row appears as an infinite, periodic set of two-dimensional profiles, or cascade. It is assumed that the performance of a blade profile is the same whether it is operating in an annular, three-dimensional flow field or in a plane, two-dimensional flow field. Since the analysis is applied to each cylindrical section of the blade independently, it neglects the effects of the hub and annulus walls, radial velocities, and the interference between radial strips. Schlichting (2) and Scholz (3) developed

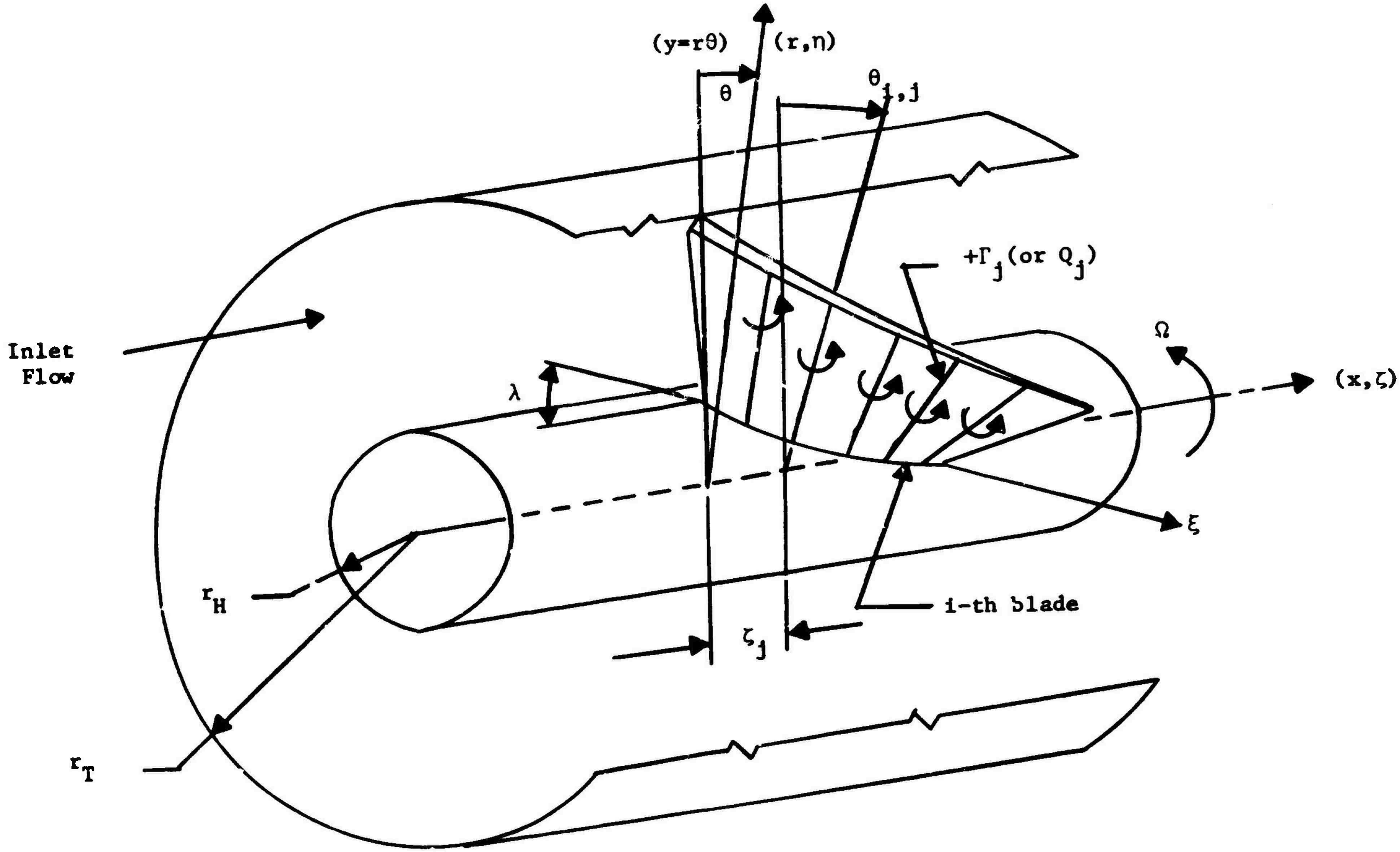

Figure 1. Coordinate System Definition and Blade Theoretical Model.

two-dimensional potential flow solutions based on the method of distributed discrete singularities, where vortices, sources, and sinks were utilized to construct the flow about a two-dimensional blade profile. The cascade theory becomes exact as the hub/tip ratio approaches unity and/or the number of blades approaches infinity. In such configurations, the blade bound vortices are nearly parallel to each other; thus, the induced radial velocities are small. In practice, the accuracy of the cascade theory has been well established for machines with many low solidity blades and hub/tip ratios greater than about 0.7.

The axisymmetric simplified radial equilibrium, actuator disk, and streamline curvature theories are essentially meridional solutions. Although the latter two allow radial velocities, the flow is assumed to be uniform in the tangential direction, and a circumferentially averaged value of the fluid properties is predicted. Thus, such techniques are accurate only for machines with many closely packed blades.

To improve the accuracy of the two-dimensional methods, corrections to the mean flow may be utilized to account for some of the real fluid effects. A boundary layer theory presented by Schlichting (4) accounts for the effect of viscosity. Lakshminarayana and Horlock (5) have presented numerous relations for tip clearance effects and secondary flows, while Mellor (6) and Horlock (7, 8) have considered separation effects and outlet angle deviation, respectively. Further, the basic two-dimensional flow solutions have been combined by Katsanis (9) in various ways, depending upon the machine configuration, to obtain an approximation of the three-dimensional flow. This technique is often called a quasi-three-dimensional solution. For example, the actuator disk theory may be used to obtain the radial variation of the inlet and exit velocities, then these velocities are used in the blade-to-blade cascade solution.

All of the methods discussed above are useful for certain limited applications. Machine configurations with high hub/tip ratios and many low solidity blades may be handled with reasonable accuracy. Nevertheless, the underlying assumption of a two-dimensional mean flow field still exists. The inherent three-dimensionality of the basic potential flow used to construct these solutions cannot be neglected for some machine configurations. Hence, three-dimensional methods for analyzing turbomachine flow are required.

1.2.2 Three-Dimensional Theory. There are many factors, some of which are listed below, which cause three-dimensionality of the flow in a turbomachine. Even in an inviscid analysis, such factors as radial variation in blade thickness, hub and annulus wall interference, hub and annulus wall taper, compressibility, tip leakage, and the radial component of the blade forces induce three-dimensionality of the flow. A viscous analysis is further complicated by the addition of hub and annulus wall boundary layers, three-dimensional blade boundary layers, and secondary flows. Further, the turbomachinery flow is highly turbulent.

No analysis is available which deals with the complete three-dimensional viscous problem. Further, the general solution even for the three-dimensional inviscid flow involves severe mathematical difficulties. Some exact and approximate methods have been proposed, but solutions are available only for some simplified cases such as incompressible, axisymmetric, or small perturbation flows. Also, some of these solutions are not valid within the blade row. Wu (10) has formulated a theory for the inviscid three-dimensional flow field due to a finite number of thick blades by reducing the three-dimensional problem to two equivalent two-dimensional problems. However, an exact general solution to the resulting non-linear equations is analytically intractable and the complete numerical solution has not been obtained. Smith and Frost (11) and Marsh (12) have worked on numerical solutions of each of Wu's two-dimensional equations. Smith (13) and Novak (14) have developed solutions for the flow in the hub-to-tip plane by satisfying the equations of motion in an average sense. Since this passage averaging technique assumes a linear variation of properties across the blade passage, it is not accurate for an impeller with only a few blades.

Since a tractable, unified theory for the entire problem of highly three-dimensional flows is lacking and numerical data are scarce, designers need a relatively rapid, approximate method of solution. McCune and Okurounmu (15), McCune (16), and McCune and Dharwadkar (17) have worked in this area and have considered the general inviscid, compressible flow in axial turbomachinery using the lifting surface technique.

Because of the difficulties involved with the exact three-dimensional solution, Tyson (18) modeled a turbomachine blade in incompressible flow by using a single radial vortex line of constant strength spanning an annulus. By solving the resulting Laplace equation with the strength of the vortex line equal to the total circulation of the blade, the three-dimensional flow field was calculated. Rossow (19) extended this technique by including a single radial source line with radially varying strength. Lifting line methods approximate the gross effects of the blade on the flow field and may be adequate if interest lies only in the gross properties of the blade row, which depend on the total circulation. However, the flow details near a lifting line are very different from those near an actual blade. Thus the blade pressure distribution or details of the flow inside the passage cannot be predicted by this method.

In order to more accurately reproduce the flow field due to an actual turbomachine blade, Tamura and Lakshminarayana (20, 21) superposed the basic solutions of Tyson and Rossow to develop a general lifting surface theory for the three-dimensional potential flow around a body or bodies spanning a cylindrical annulus. This theory represents the blade by several discrete radial singularity lines distributed over a helical surface of finite chord as shown in Figure 1. By appropriately locating any number of radial bound vortex lines for generating circulation and source lines for generating thickness, lifting or non-lifting bodies may be modeled. If the body is lifting, it must have radially constant circulation, since the theory does not consider shed vortices, and the series of radial bound vortex lines must have a total circulation equal to the actual blade circulation. They, in a fashion similar to others who have considered three-dimensional vortex theories, did not attempt to relate the singularity distribution to any actual blade geometry.

The lifting surface theories have been successfully used for the design and analysis of unshrouded propellers (e.g. Reference 22). In a shrouded configuration, it becomes necessary to include the constraints due to the annulus walls.

Tamura and Lakshminarayana's (21) theory is adopted here for the prediction of three-dimensional potential flow in turbomachinery. A detailed presentation of the theory and derivation of all equations are given by Tamura and Lakshminarayana (20, 21). The main equations are reproduced and briefly summarized below for completeness. Both a single radial vortex line of a constant strength and a single radial source line of varying strength spanning an annulus are governed by Laplace's equation,

$$\frac{1}{\eta}\frac{\partial}{\partial\eta}\left(\eta\frac{\partial\phi_v}{\partial\eta}\right)+\frac{1}{\eta^2}\frac{\partial^2\phi_v}{\partial\theta^2}+\frac{\partial^2\phi_v}{\partial\zeta^2}=0 \qquad (1)$$

where η, θ, ζ are radial, tangential and axial coordinates and ϕ_v is the non-dimensional perturbation velocity potential. The boundary conditions for the vortex line are 1) the axial and radial velocities vanish at $\zeta \to \pm\infty$, 2) the radial velocity vanishes at the hub and annulus walls, 3) at $\zeta \to \pm\infty$ the tangential velocity distribution is irrotational. Applying these conditions, the solution of Equation (1) is

$$\phi_v = \mp\frac{\Gamma}{4\pi}\left(\theta + 2\sum_{m=1}^{\infty}\frac{\sin m\theta}{m}\sum_{n=1}^{\infty}\exp(\mp K_{mn}\zeta)F_v(K_{mn},\nu)Z_m(K_{mn}\eta)\right) \qquad (2)$$

where the upper and lower signs refer to $+\zeta$, and $-\zeta$ directions, respectively, Γ is the non-dimensional circulation, and where the following quantities have been defined for convenience:

$$F_v(K_{mn},\nu) = \frac{\int_\nu^1 \eta Z_m(K_{mn}\eta)\,d\eta}{\int_\nu^1 \eta Z_m^2(K_{mn}\eta)\,d\eta} \qquad (3)$$

and

$$Z_m(K_{mn}\eta) = J_m(K_{mn}\eta)Y_m'(K_{mn}) - J_m'(K_{mn})\,Y_m(K_{mn}\eta) \tag{4}$$

where J_m, Y_m = m-th order Bessel functions of first or second kind, respectively.

The boundary conditions for the source line are that 1) half of the mass flow due to the source goes to $\zeta = +\infty$ and half to $\zeta = -\infty$, 2) the radial velocity vanishes at the hub and annulus wall, and at $\zeta = \pm\infty$. In addition, a limiting condition for the axial velocity very close to the singularity is used. The solution is thus

$$\phi_s = \frac{1}{4\pi}\left(\pm\frac{2\zeta}{1-\nu^2}\int_\nu^1 Q(\eta)\,d\eta - \sum_{n=2}^{\infty} \exp(\mp K_{on}\zeta)\cdot\frac{F_s(K_{on},\nu)}{K_{on}}\cdot Z_o(K_{on}\eta)\right.$$

$$\left. - 2\sum_{m=1}^{\infty}\cos m\theta \sum_{n=1}^{\infty}\exp(\mp K_{mn}\zeta)\cdot\frac{F_s(K_{mn},\nu)}{K_{mn}}\cdot Z_m(K_{mn}\eta)\right) \tag{5}$$

where

$$F_s(K_{mn},\nu) = \frac{\int_\nu^1 Q(\eta)Z_m(K_{mn}\eta)\,d\eta}{\int_\nu^1 \eta Z_m^{\,2}(K_{mn}\eta)\,d\eta} \tag{6}$$

and $Q(\eta)$ is the non-dimensional source strength at any radii. Unlike the vortex case, the source strength can be radially varying. ϕ_s is the perturbation potential due to the source only.

The solution for an arbitrary number of blades (NB), each represented by an arbitrary number of singularities (JVS), is obtained by superposing the solutions for a single vortex line and/or a single source line given by Equations (2) and (5). The combined solution for the vortex system is

$$\phi_v = \mp \frac{NB}{4\pi} \sum_{j=1}^{JVS} \Gamma_j [\theta + 2 \sum_{\ell=1}^{\infty} \frac{\sin k\,(\theta - \theta_{1,j})}{k} \cdot \sum_{n=1}^{\infty} \exp(\mp K_{kn}(\zeta - \zeta_j)) \cdot F_v(K_{kn},\nu)\, Z_k\,(K_{kn}\eta)]. \tag{7}$$

where $k = \ell \cdot NB$ and where $\theta_{i,j}$ represents the location of j-th vortex representing the i-th blade. Tamura and Lakshminarayana (21) have simplified the summation over i number of blades (NB) so that only $\theta_{1,j}$ remains in the summation over ℓ. Differentiating Equation (7), the tangential, radial, and axial velocity components due to a vortex system can be written as,

$$u_{v\theta} = \mp \frac{NB}{4\pi\eta} \sum_{j=1}^{JVS} \Gamma_j \,[1 + 2 \sum_{\ell=1}^{\infty} \cos k\,(\theta - \theta_{1j}) \sum_{n=1}^{\infty} \exp(\mp K_{kn}(\zeta - \zeta_j)) \cdot F_v(K_{kn},\nu) Z_k(K_{kn}\eta)], \tag{8}$$

$$u_{v\eta} = \mp \frac{NB}{2\pi} \sum_{j=1}^{JVS} \Gamma_j \sum_{\ell=1}^{\infty} \frac{\sin k\,(\theta - \theta_{1j})}{k} \sum_{n=1}^{\infty} \exp(\mp K_{kn}(\zeta - \zeta_j)) \cdot F_v(K_{kn},\nu)\, \frac{\partial Z_k(K_{kn}\eta)}{\partial \eta} \tag{9}$$

and

$$u_{v\zeta} = \frac{NB}{2\pi} \sum_{j=1}^{JVS} \Gamma_j \sum_{\ell=1}^{\infty} \frac{\sin k\,(\theta - \theta_{1j})}{k} \sum_{n=1}^{\infty} K_{kn} \exp(\mp K_{kn}(\zeta - \zeta_j)) \cdot F_v(K_{kn},\nu) \cdot Z_k(K_{kn}\eta), \tag{10}$$

where $u_{v\theta}$, $u_{v\eta}$, $u_{v\zeta}$ are the non-dimensional velocity perturbations in θ, η and ζ directions, respectively, due to a vortex line spanning the annulus.

The combined solution for a system of sources is

$$\phi_s = \frac{NB}{4\pi} \sum_{j=1}^{JVS} [\pm \frac{2(\zeta - \zeta_j)}{1 - \nu^2} \int_{\nu}^{1} Q_j(\eta)\, d\eta$$

$$- \sum_{n=2}^{\infty} \exp(\mp K_{on}(\zeta - \zeta_j)) \frac{F_s(K_{on},\nu,j)}{K_{on}} Z_o(K_{on}\eta)$$

$$- 2 \sum_{\ell=1}^{\infty} \cos k(\theta - \theta_{1j}) \sum_{n=1}^{\infty} \exp(\mp K_{kn}(\zeta - \zeta_j)) \frac{F_s(K_{kn},\nu,j)}{K_{kn}} Z_k(K_{kn}\eta)].$$

(11)

Differentiating gives the velocity components

$$u_{s\theta} = \mp \frac{NB}{2\pi\eta} \cdot \sum_{j=1}^{JVS} \sum_{\ell=1}^{\infty} k \sin k\,(\theta - \theta_{1j})$$

$$\sum_{n=1}^{\infty} \exp(\mp K_{kn}(\zeta - \zeta_j)) \frac{F_s(K_{kn},\nu,j)}{K_{kn}} Z_k(K_{kn}\eta), \tag{12}$$

$$u_{s\eta} = - \frac{NB}{4\pi} \sum_{j=1}^{JVS} [\sum_{n=2}^{\infty} \exp(\mp K_{on}(\zeta - \zeta_j)) \frac{F_s(K_{on},\nu,j)}{K_{on}} \frac{\partial Z_o(K_{on}\eta)}{\partial\eta}$$

$$+ 2 \sum_{\ell=1}^{\infty} \cos k(\theta - \theta_{1j}) \sum_{n=1}^{\infty} \exp(\mp K_{kn}(\zeta - \zeta_j)) \frac{F_s(K_{kn},\nu,j)}{K_{kn}} \frac{\partial Z_k(K_{kn}\eta)}{\partial\eta}]$$

(13)

and

$$u_{s\zeta} = \frac{NB}{4\pi} \sum_{j=1}^{JVS} [\pm \frac{2}{1-\nu^2} \int_{\nu}^{1} Q_j(\eta)d\eta \pm \sum_{n=2}^{\infty} \exp(\mp K_{on}(\zeta-\zeta_j))F_s(K_{on},\nu,j)Z_o(K_{on}\eta)$$

$$\pm 2 \sum_{\ell=1}^{\infty} \cos k(\theta-\theta_{1j}) \sum_{n=1}^{\infty} \exp(\mp K_{kn}(\zeta-\zeta_j))F_s(K_{kn},\nu,j)Z_k(K_{kn}\eta)] , \quad (14)$$

where $u_{s\theta}$, $u_{s\eta}$, $u_{s\zeta}$ are the non-dimensional perturbation velocities in θ, η and ζ directions, respectively, due to a source line spanning the annulus. The upper and lower signs refer to $\zeta - \zeta_j > 0$ and $\zeta - \zeta_j < 0$, respectively, and $k = \ell \cdot NB$ where ℓ is an integer.

The radially variable non-dimensional strength of each source line is described by the P-th degree polynomial,

$$Q_j(\eta) = A_{j,0} + A_{j,1}\eta + \ldots + A_{j,p}\eta^P . \quad (15)$$

By appropriately selecting the constants $A_{j,p}$ and P, an arbitrary radial variation may be obtained.

A computer program based on this discrete singularity method may be used to calculate the three-dimensional potential flow around a body spanning a cylindrical annulus. The flow is assumed to be inviscid, incompressible, and the absolute flow is irrotational. A set of four auxiliary programs computes eigen values and other functions which are then stored on magnetic tape and used as input to the main program.

1.3 Method of Investigation

The general objectives of this work were to develop a further understanding of the three-dimensional flow in turbomachinery, to determine the order of magnitude of the difference between the three-dimensional and widely used two-dimensional solutions, and to define those impeller configurations which require a three-dimensional treatment. The method presented herein is not intended to be a finished three-dimensional design procedure, but rather a study of the order of magnitude of certain isolated three-dimensional flow effects.

To gain insight into the accuracy of the three-dimensional and two-dimensional methods when applied to a highly three-dimensional flow, theoretical and experimental investigations of the flow field in a low hub/tip ratio impeller with a small number of blades of high solidity have been conducted. As mentioned previously, many factors contribute to the three-dimensionality of the flow. The present work was limited to a study of the three-dimensional potential flow effects caused by the interference of the hub and annulus walls and the mutual interference effects of the non-parallel bound vortex elements replacing the blades. In order to isolate the desired effects, the flow was simplified by assuming it to be inviscid, incompressible, and the absolute flow is irrotational. Further, only blades of free vortex design, that is with constant circulation from hub to tip, are considered. No tip leakage is allowed. A radially varying circulation would require shed vortices by the Helmholtz vortex law. Such a trailing vortex system would induce its own three-dimensional flows and obscure the desired effects. As a consequence of these assumptions, the analyses of Tyson (18), Rossow (19) and Tamura and Lakshminarayana (20, 21) were utilized. The computer solution developed by Tamura and Lakshminarayana (20, 21) has been used to calculate the three-dimensional potential flow through a turbomachine impeller with radial blades, no dihedral or sweep, radially constant circulation and a constant hub/tip ratio. The method, which includes the effect of radially varying source strength, is based on the method of distributed singularities, where the blades are replaced by radial line vortices and sources located along the blade camber surface. Before using this numerical solution, it was necessary to establish a method of relating a given blade geometry to a three-dimensional singularity distribution. The Douglas Neumann two-dimensional cascade program by Geising (23) was also used to analyze the flow field. The blade pressure distributions of two actual impeller configurations, one constructed by the present author and the other done by Bowerman (24), have been calculated and measured experimentally. The designer has been provided with guidance as to the validity of the theories under varying machine configurations and with corrections for the difference between the two-dimensional predictions and the actual three-dimensional flow conditions.

Since there has been little investigation of the effect of blade dihedral, an experimental investigation of this effect was undertaken. Although no mathematical theory was developed, a qualitative discussion and interpretation of the data for a blade with dihedral has been included.

Even though this investigation was limited to a two- or three-bladed axial flow propeller pump, the mathematical model and conclusions derived should lead to a better understanding and design of underwater propellers, axial flow inducers, and fans.

CHAPTER II

THEORETICAL ANALYSIS

2.1 Numerical Technique

Various properties of flow fields were examined using two computer solutions based on potential flow theory: the two-dimensional Douglas Neumann cascade program developed by Geising (23), and the three-dimensional discrete singularity program developed by Tamura and Lakshminarayana (21) with some modifications. The Douglas Neumann program, which applies a surface singularity method by distributing sources over the surface of a body in such a way that the flow normal to the surface is either zero or prescribed, closely approximates an exact two-dimensional solution if a sufficient number of points are used to specify the profile shape accurately. Hence, this method was assumed to provide the solution for a profile represented by a continuous vorticity and source distribution. Tamura's program, which represents a body by a distribution of concentrated discrete vortices and/or sources located on the camber line, provided a solution to the three-dimensional flow in an annulus.

Before using the three-dimensional program it was necessary to use a set of auxiliary programs to prepare a magnetic tape containing Bessel functions and other parameters needed for input to this program (21). However, a prerequisite of this procedure is a knowledge of at least the first three eigen values of

$$\frac{J_m'(K_{mn})}{Y_m'(K_{mn})} = \frac{J_m'(K_{mn}\nu)}{Y_m'(K_{mn}\nu)} , \qquad (16)$$

where J_m' = first derivative of the m-th order Bessel function of the first kind,

Y_m' = first derivative of the m-th order Bessel function of the second kind,

K_{mn} = n-th eigen value corresponding to the m-th order Bessel function,

and ν = hub/tip radius ratio.

This equation was shown by Tyson (18) to result from the boundary condition that the radial velocity at the hub and annulus walls must be zero. A polynomial series approximation which was presented by McMahon (25) was programmed by Tamura et al. (26) and used to provide an estimate of the eigen values for Equation (16). This polynomial approximates the eigen values K_{mn} for $m = 0$ to m_{LAST} and $n = 2$ to n_{LAST}, where m_{LAST} and n_{LAST} specify the maximum number of eigen values to be calculated. It is quite accurate for large hub/tip ratios and low values of n, but as the hub/tip ratio decreases and/or n increases accurate values of K_{mn} are found only for lower values of m. The variation of m_L, the maximum m for which the eigen value estimate is accurate to within 1% of the exact eigen value, is shown in Figure 2 as a function of ν and n. For $m > m_L$, the error grows very rapidly. Eigen value estimates for $m > m_L$ and for all $n = 1$ were obtained by extrapolation using the Eigen Value Survey program (20, 21).

The eigen values K_{mn} and hub/tip ratio ν are related by Equation (16). Thus, the set of auxiliary programs for the evaluation of the exact eigen values, Bessel functions, and other parameters must be executed for each different hub/tip ratio to be considered. Since lower hub/tip ratios require more eigen values for convergence of the solution

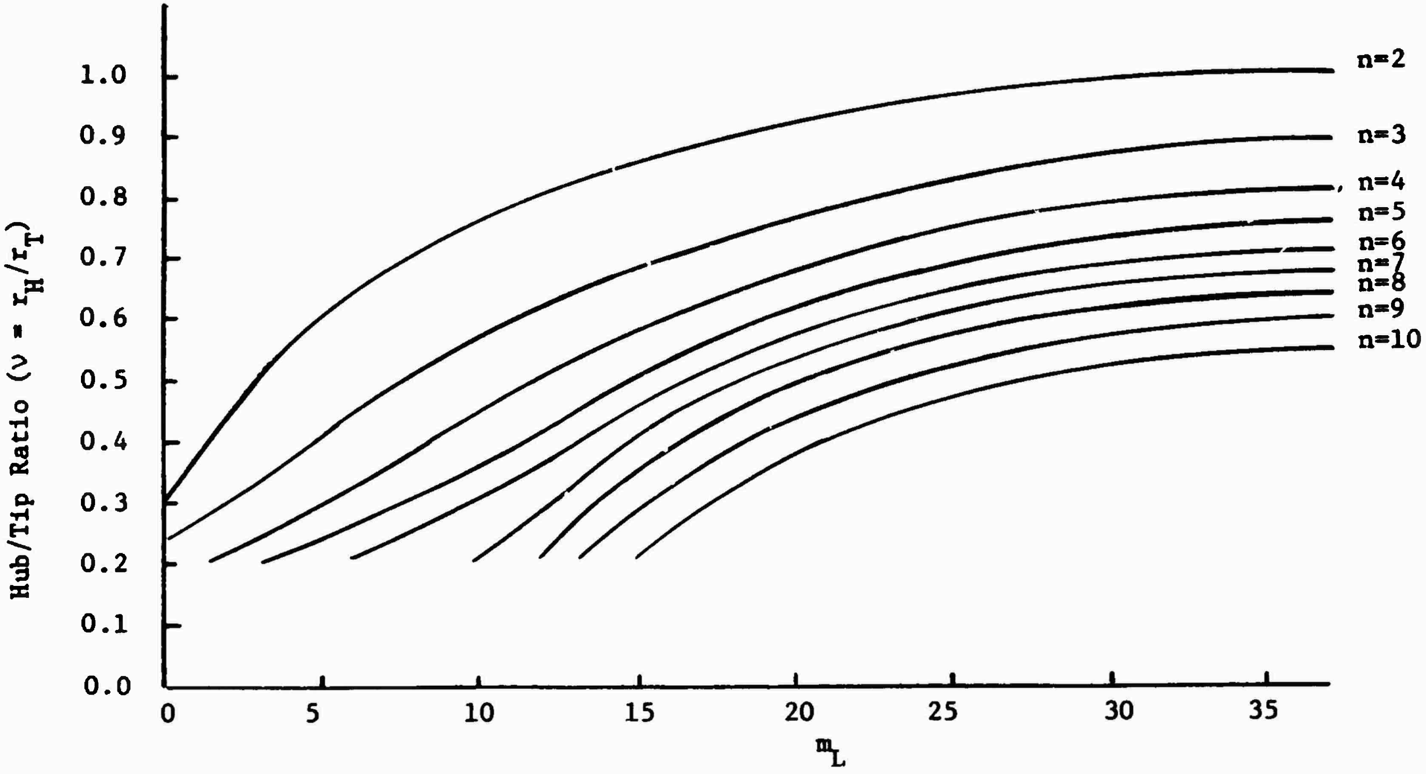

Figure 2. The Maximum Value of m for Which the Eigen Value Estimate is Accurate to Within One Percent of the Exact Eigen Value.

and since fewer may be estimated accurately, the extrapolation process for such cases becomes more lengthy.

Tapes are presently available for three hub/tip ratios: 0.300, 0.442, 0.600. The eigen values for $\nu = 0.442$ are shown in Figure 3.

From a comparison of these three cases, it is evident that the eigen values are the same in some ranges. When $n = 1$, for example, the eigen values for $\nu = 0.300$ and 0.442 are identical (to eight digit accuracy) above $m = 26$, and the eigen values for $\nu = 0.442$ and 0.600 are identical above $m = 48$. Hence, when preparing eigen values in addition to those presently available, the eigen values for higher values of m may in some cases be obtained by a careful analysis of the existing eigen values rather than by the somewhat lengthy numerical calculation.

2.2 The Mathematical Model: Preliminary Investigation

2.2.1 Isolated Radial Singularity Lines Spanning an Annulus.

As a first step in illustrating the three-dimensional potential effects, the flow perturbations due to a single radial vortex and a single radial source line, both of constant strength unity, were calculated by the two-dimensional and three-dimensional theories. The results given in this section are complementary to those provided by Tamura and Lakshminarayana (20) who independently carried out an extensive investigation of the three-dimensional effects due to a single vortex and source spanning an annulus. These singularities were located at $\zeta_j = 0$ and $\theta_{i,j} = 0$, where $i = j = 1$. The induced velocity components were calculated at several points ζ, θ at the hub, mid, and tip radii. A comparison of the two- and three-dimensional predictions is summarized in Table 1. These results are based on average absolute values in the region close to the

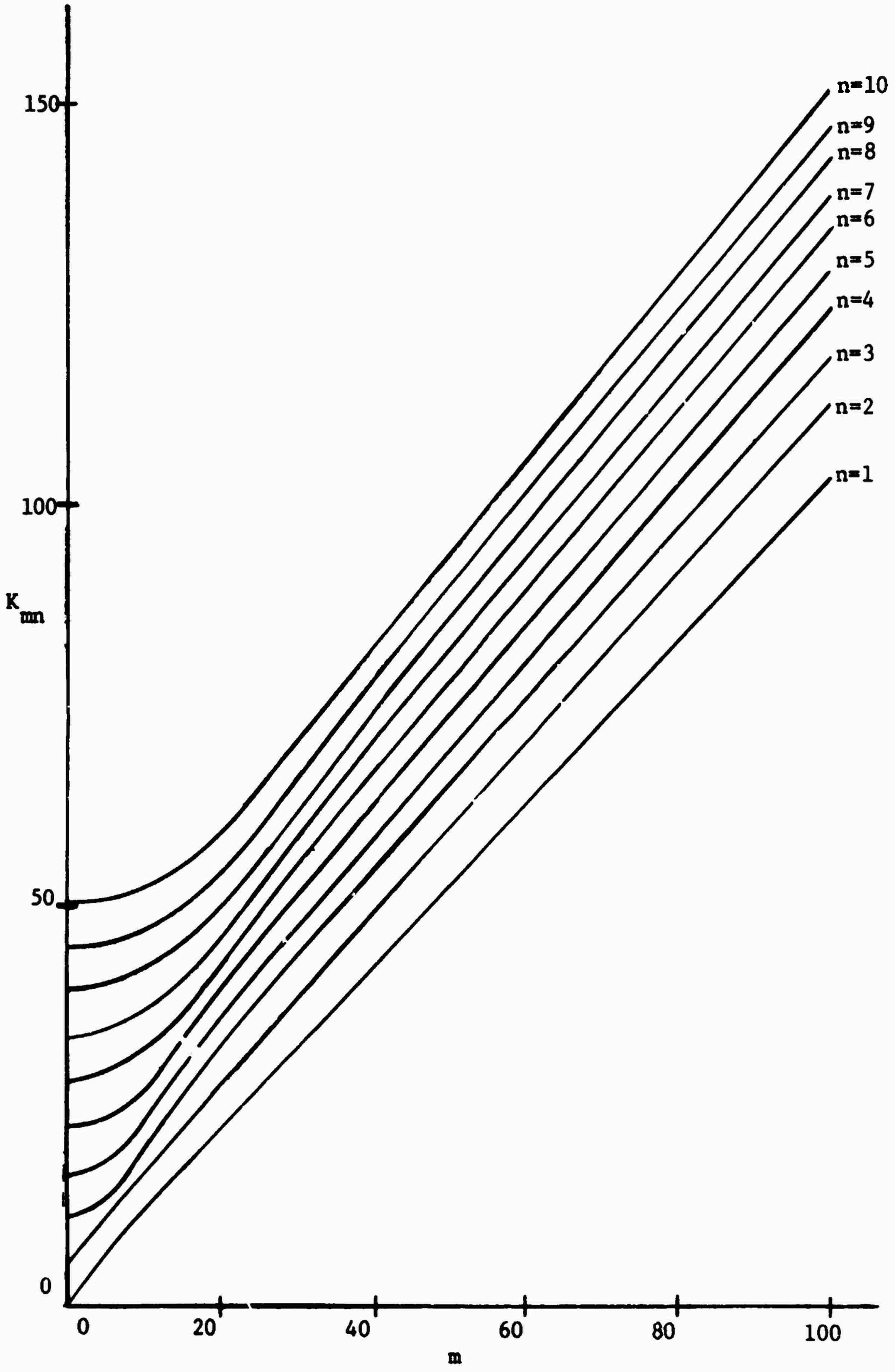

Figure 3. Eigen Values for Hub/Tip Ratio ν = 0.442.

Table 1

COMPARISON OF THE MAGNITUDES OF THE VELOCITY PERTURBATIONS INDUCED BY A SINGLE RADIAL VORTEX AND SOURCE LINE AS PREDICTED BY TWO- AND THREE-DIMENSIONAL THEORIES

	Axial	Tangential	Radial
$\nu = 0.6$			
Hub	$\lvert u_\zeta \rvert_3 < \lvert u_\zeta \rvert_2$	$\lvert u_\theta \rvert_3 > \lvert u_\theta \rvert_2$	$(u_\eta)_3 = 0$
Mid	$(u_\zeta)_3 = (u_\zeta)_2$	$(u_\theta)_3 = (u_\theta)_2$	$\lvert u_\eta \rvert_3 \simeq 0.10 \lvert u_\zeta \rvert_3$
Tip	$\lvert u_\zeta \rvert_3 > \lvert u_\zeta \rvert_2$	$\lvert u_\theta \rvert_3 < \lvert u_\theta \rvert_2$	$(u_\eta)_3 = 0$
$\nu = 0.3$			
Hub	$\lvert u_\zeta \rvert_3 < \lvert u_\zeta \rvert_2$	$\lvert u_\theta \rvert_3 > \lvert u_\theta \rvert_2$	$(u_\eta)_3 = 0$
Mid	$(u_\zeta)_3 \simeq (u_\zeta)_2$	$(u_\theta)_3 \simeq (u_\theta)_2$	$\lvert u_\eta \rvert_3 \simeq 0.15 \lvert u_\zeta \rvert_3$
Tip	$\lvert u_\zeta \rvert_3 > \lvert u_\zeta \rvert_2$	$\lvert u_\theta \rvert_3 < \lvert u_\theta \rvert_2$	$(u_\eta)_3 = 0$

singularity ($\zeta < 0.04$, $\theta < 30^\circ$), where the induced velocities were found to be greatest. Thus, they indicate gross trends and not deviations at any one specific point. In fact, for some cases the local deviation farther away from the singularity is opposite to the gross trends shown. But since the magnitude of the induced velocity at these points is smaller, the dominant effect is that found near the singularity.

The table shows that the tangential velocities predicted by the three-dimensional theory are generally greater at the hub and smaller at the tip than the two-dimensional predictions. Conversely, the three-dimensional theory predicts the axial velocities to be smaller at the hub and greater at the tip. Further, the magnitude of this descrepancy for both the tangential and axial components is generally larger at the hub than at the tip. This is due to the smaller radius of curvature of the hub, and hence, more three-dimensionality of the flow in this region. At the mid-radius, the discrepancy between the two- and three-dimensional predictions is generally negligible, except for regions close to the singularity in the lower hub/tip ratio case.

Significant deviations were observed with the radial velocity. Prediction of radial velocity is beyond the capabilities of the two-dimensional theory; for $\nu = 0.6$, the three-dimensional theory predicts radial velocities at the mid-radius of about 15 percent of the axial velocity. Radial velocities at the hub and tip are required to be zero by the boundary conditions of the three-dimensional theory. Also, the effect of hub/tip ratio variation is most pronounced for the radial velocity. Reduction of the hub/tip ratio from 0.6 to 0.3 caused the radial velocity at mid-radius to increase by about 50%. These results were obtained independently by the present author and Tamura and

Lakshminarayana (20). For a detailed comparison of each of the two- and three-dimensional velocity components, the reader is referred to the numerous graphs presented by the latter.

By refining the calculation to include nine radial locations, the mid-radius was found not to be the point of maximum radial velocities. The variation of the radial velocities induced by a single vortex line versus axial distance is presented in Figures 4 and 5 for $\nu = 0.3$ and $\nu = 0.6$, respectively. Comparing the five radial positions plotted, the maximum radial velocity for any axial position occurs near $\eta = 0.58$ for $\nu = 0.3$ and near $\eta = 0.76$ for $\nu = 0.6$. At radial positions either greater or less than those plotted, the radial velocities must fall to zero to satisfy the wall boundary conditions. Thus, the maximum radial velocity occurs at a radial location somewhat less than the mid-radius. The variation of radial velocity at this maximum position is compared for $\nu = 0.3$ and $\nu = 0.6$ in Figure 6. Similar plots for a single source line of constant strength are shown in Figures 7 and 8. Although somewhat obvious for a radially varying source distribution, these figures show that even a constant source distribution induces significant three-dimensional flows.

The results show that the three-dimensional effects are large for hub/tip ratios below 0.6. Analysis of these flow fields at several radial locations confirms that (a) there are significant differences between the two-dimensional and three-dimensional predictions of induced velocity, and (b) these differences become greater with decreasing hub/tip ratio. Since the pressure distribution over a blade is directly related to the velocity distribution, a significant variation between the blade lift and moment as predicted by the two-dimensional and three-

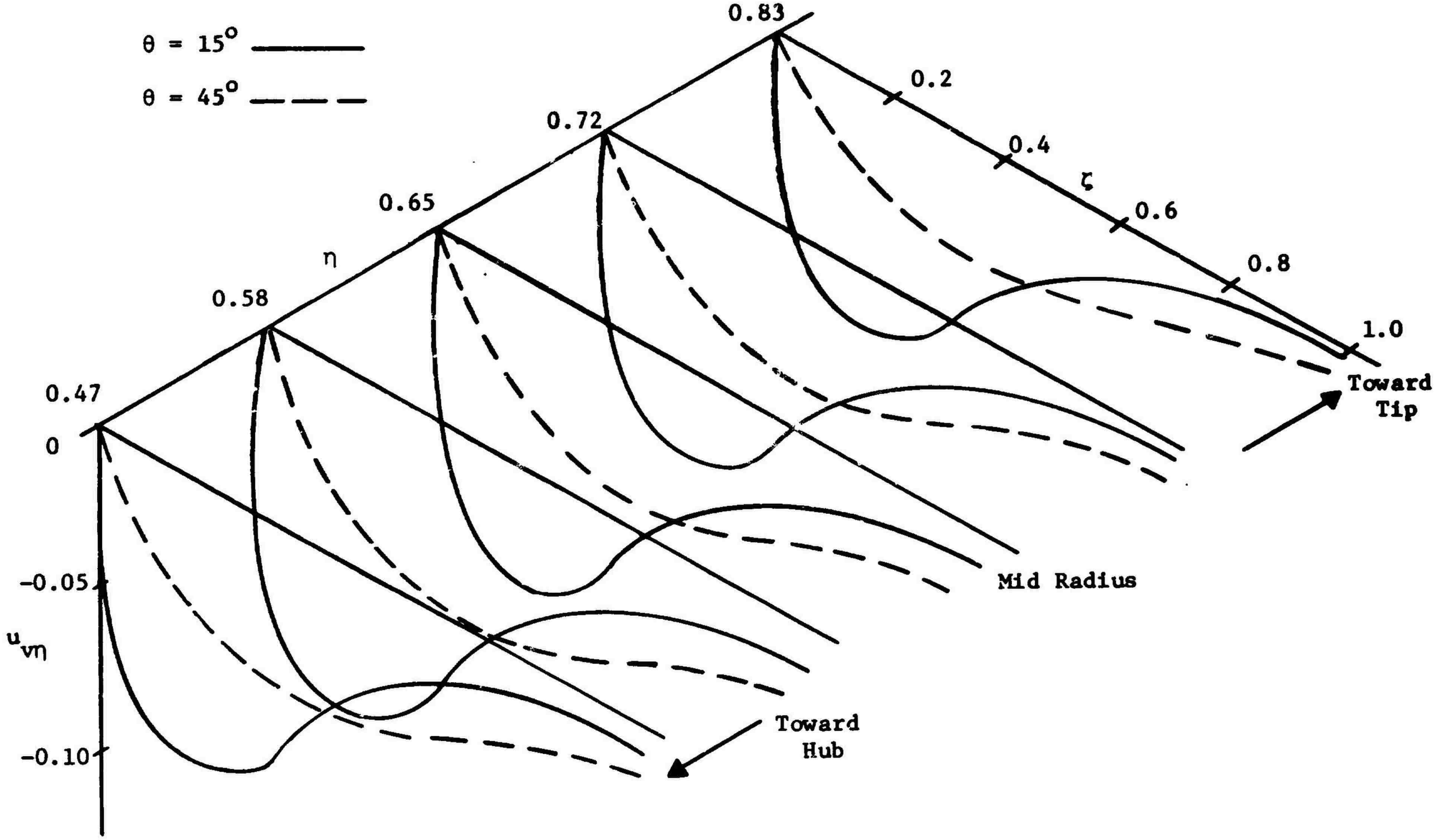

Figure 4. Variation of Radial Velocity Induced by a Single Vortex Line.
(ν = 0.3; Γ = 1.0)

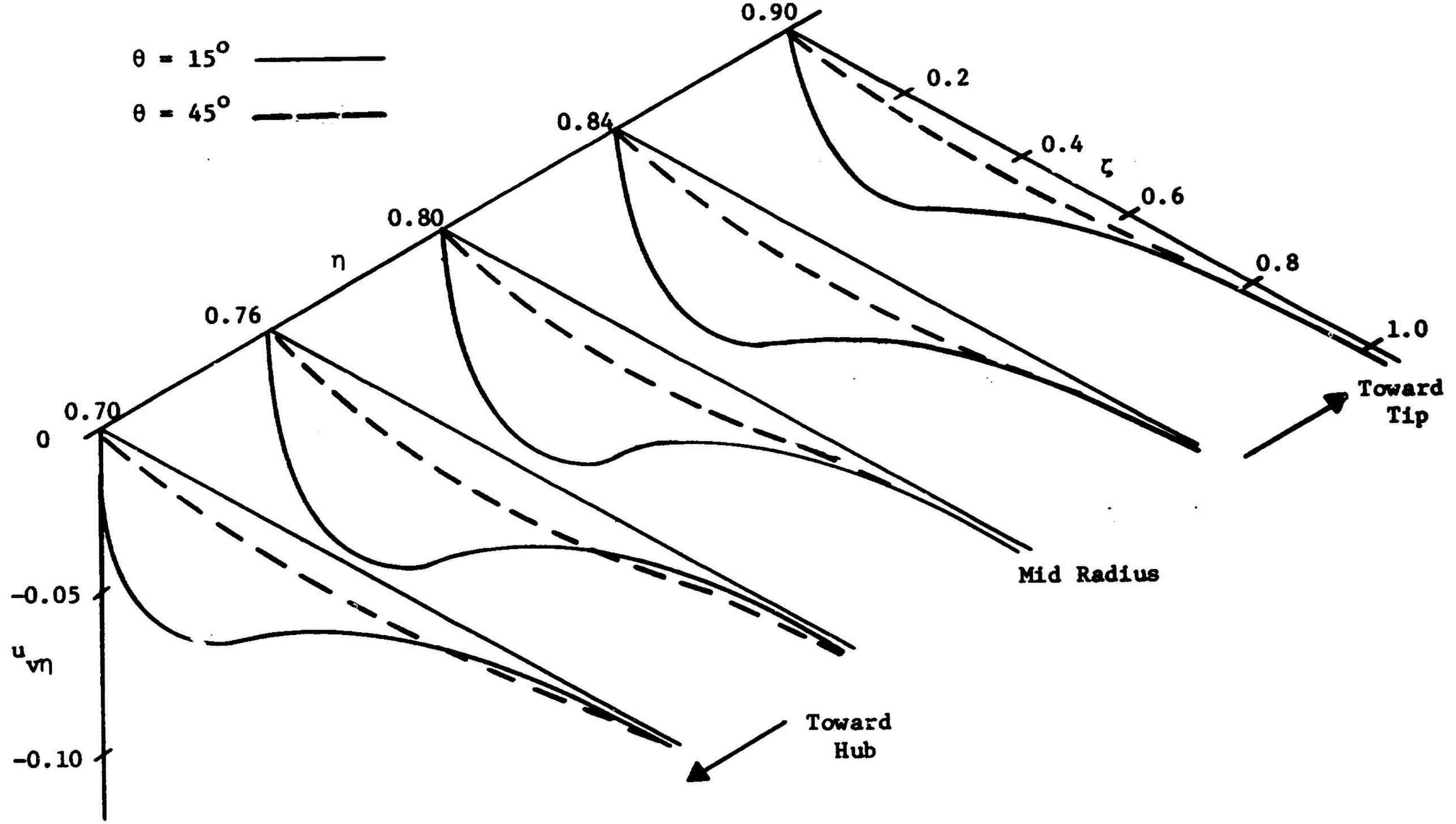

Figure 5. Variation of Radial Velocity Induced by a Single Vortex Line. (ν = 0.6; Γ 1.0)

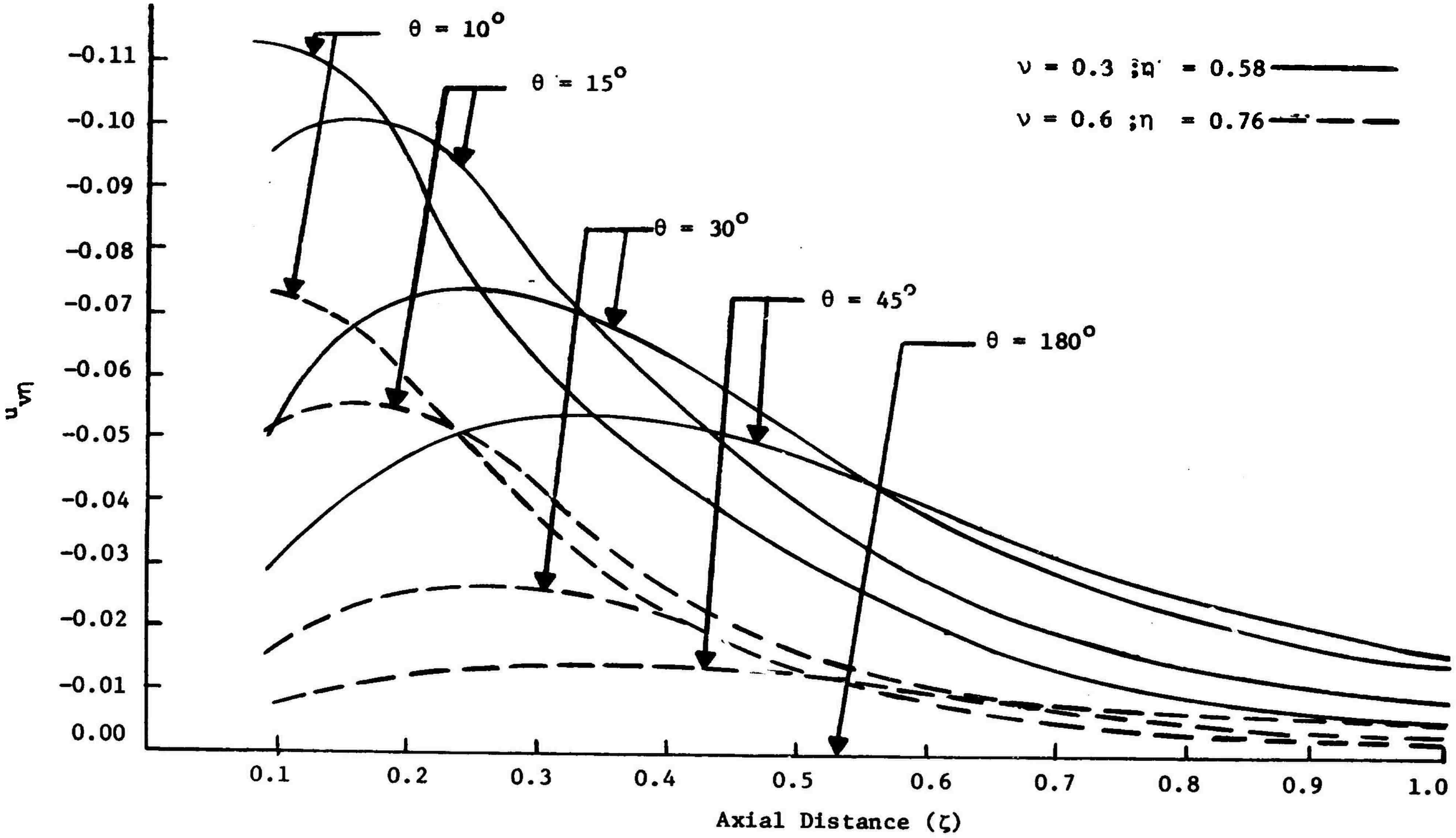

Figure 6. Maximum Three-Dimensional Radial Velocity Distribution Induced by a Single Vortex Line Showing the Effect of Hub/Tip Ratio (Γ = 1.0).

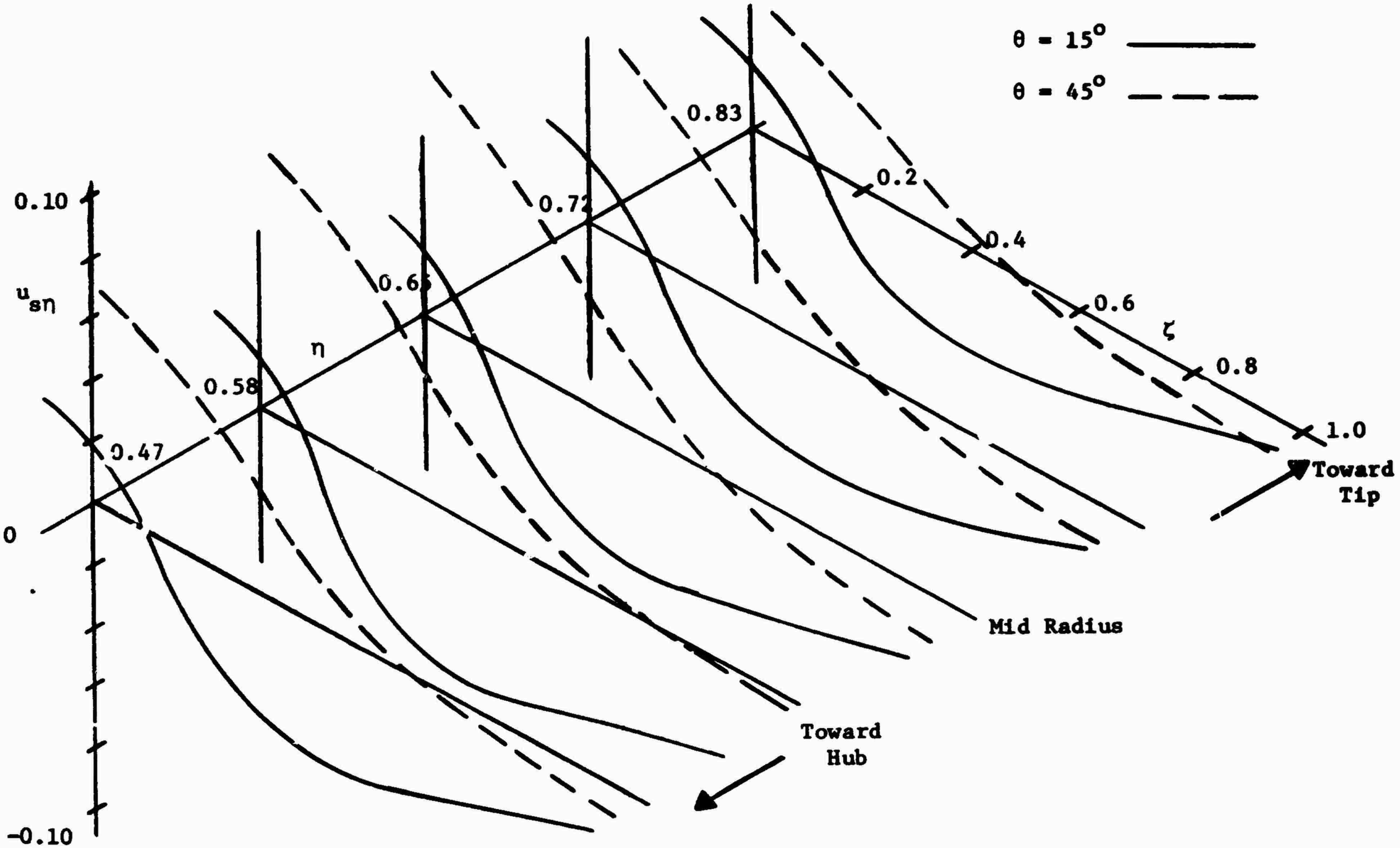

Figure 7. Variation of Radial Velocity Induced by a Single Source Line. (ν = 0.3; Q = 1.0)

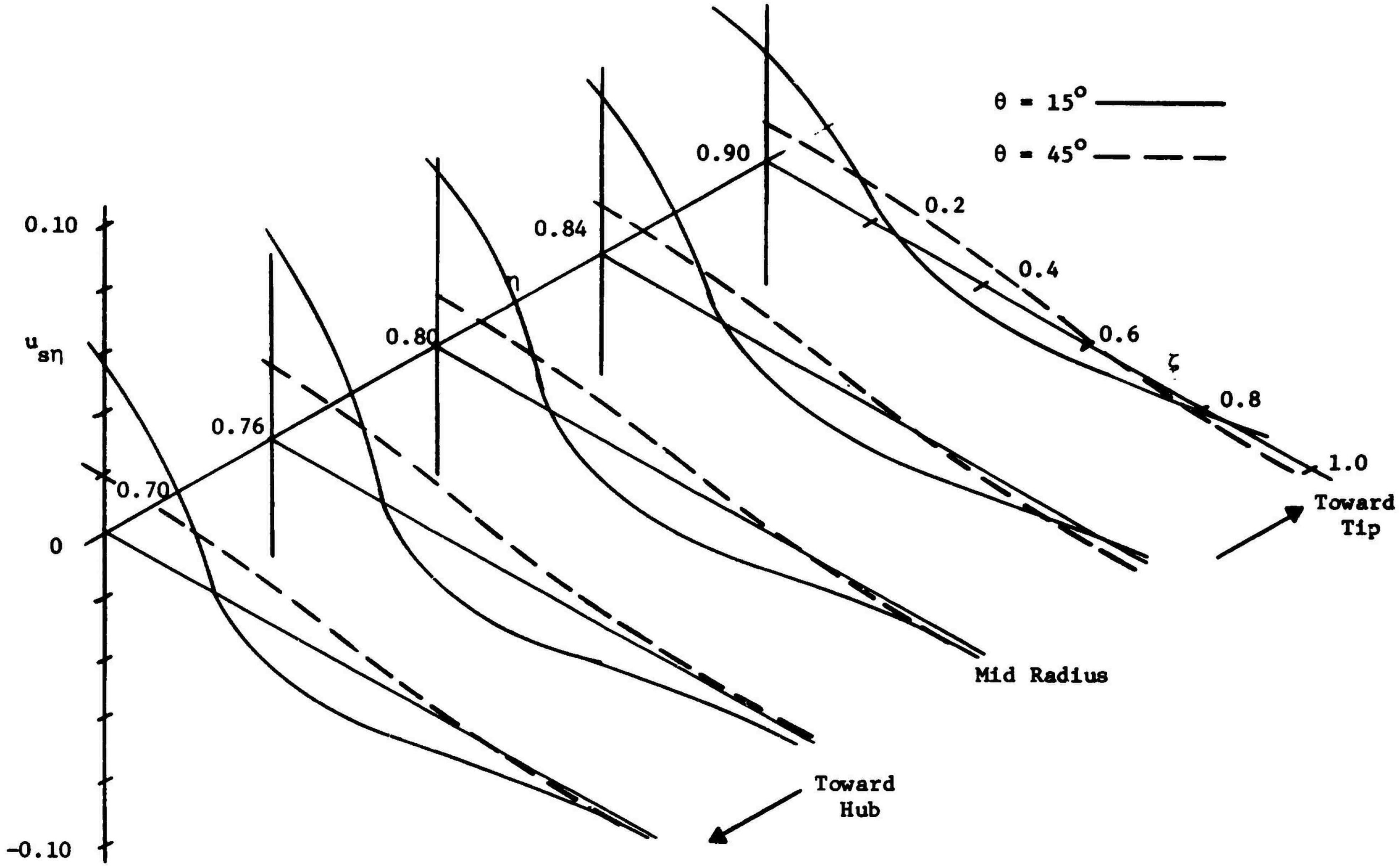

Figure 8. Variation of Radial Velocity Induced by a Single Source Line.
(ν = 0.6; Q = 1.0)

dimensional methods is expected. The results of this analysis agree with similar work done by Tyson (18) and Etter and Van Dyke (27).

2.2.2 Discussion of a Rotor Model. It is known from cascade theory that a two-dimensional blade profile may be represented by appropriate continuous vortex and source distributions. Further, these continuous distributions may be concentrated into a finite number of discrete singularities. For example, a plot of the continuous circulation distribution over a blade profile versus chord may be divided at intervals along the chord into a finite number of strips. That portion of the total circulation represented by the area within each strip may be assumed to be concentrated in a discrete vortex located at the centroid of the area of the strip. A similar procedure applies to the source distribution. This technique often simplifies the solution, yet provides a good approximation of the effects of the blade.

In principle, this technique may be extended by mathematically modeling a three-dimensional turbomachine blade by a distribution of discrete singularity lines spanning an annulus. By using discrete radial vortex and source lines, the effects on the flow of both blade turning and thickness may be represented and the blade performance predicted. However, little work has been done on the practical problem of establishing a method to relate these singularity distributions used in the mathematical model to an actual three-dimensional blade geometry. Thus, the problem was twofold. First, such a relationship between the blade geometry and the singularity strength had to be developed. This was done by equating the slope of the profile surface in both the three-dimensional and the known two-dimensional reference flow. Second, using this representation, the performance was calculated by the three-dimensional theory. The change in tangential velocity, or circulation, was compared with two-dimensionally predicted values.

Analysis of the three-dimensional flow field has been extended to a three-bladed rotor configuration by representing the rotor as a superposition of the fields of three groups of ten radial vortex and source lines each (Figure 1). The flow field of this rotor has been developed for varying hub/tip ratio, varying stagger angle, and by both two-dimensional and three-dimensional methods.

Similar work has been done by Tamura (21) for an arbitrarily chosen vortex and source distribution. In contrast, the work presented herein has attempted to relate the singularity distribution to the geometry of an actual blade configuration. The procedure, results, and conclusions derived from this model are presented in detail in subsequent sections.

A three-dimensional blade geometry is typically specified in terms of standard two-dimensional profiles which are located at several radii. Thus, the problem is to relate this known geometry to the strength of the vortex and source lines used in the three-dimensional mathematical model. Since the two-dimensional profiles are known, it would be convenient to use cascade theory for this purpose. It is clear, in view of the study reported in section 2.2.1, that the vortex and/or source distribution obtained by a cascade method, such as that presented by Schlichting (2), for a given two-dimensional profile will not generate the same profile geometry when utilized in a three-dimensional annular flow model.

In order to gain a qualitative understanding of this three-dimensional effect, consider an airfoil represented by a set of discrete vortices. From cascade theory, the kinematic condition requiring the flow to be tangent to a cambered plate airfoil is

$$(\frac{dy}{dx})_2 = \frac{w_\theta + (u_{v\theta})_2}{w_\zeta + (u_{v\zeta})_2} , \qquad (17)$$

where $(\frac{dy}{dx})_2$ = the slope of the two-dimensional airfoil surface, w_ζ, w_θ = axial and tangential components of the mean velocity, $(u_{v\zeta})_2$, $(u_{v\theta})_2$ = axial and tangential components of the velocity perturbations induced by the two-dimensional vortices $(\Gamma_j)_2$ where $j = 1, \ldots$ JVS. Similarly, if this same vortex distribution which satisfies Equation (2) is used in the three-dimensional flow model such that

$$(\Gamma_j)_2 = (\Gamma_j)_3 \text{ for all } j = 1, \text{JVS} \qquad (18)$$

then the corresponding three-dimensional kinematic condition is

$$(\frac{dy}{dx})_3 = \frac{w_\theta + (u_{v\theta})_3}{w_\zeta + (u_{v\zeta})_3} . \qquad (19)$$

Although a radial perturbation velocity component also exists in the three-dimensional case, this kinematic condition requires that the component of the three-dimensional velocity vector lying in the plane of the specified two-dimensional airfoil section must be tangent to the camber surface. Furthermore, at the hub and tip radii the radial velocity is required to be identically zero by the boundary conditions.

For the same circulation (Γ_j), the induced velocities are different for two-dimensional and three-dimensional case. It is thus clear that the profiles generated in a rectilinear cascade and in a rotor will be different for the same circulation or loading distribution.

Similar arguments for the source distribution imply a three-dimensional profile with greater thickness gradients at the hub and smaller thickness gradients at the tip than that predicted by the two-dimensional theory.

At the mid radius, the situation is more straightforward. Since the two- and three-dimensional velocities induced at the mid radius are at least approximately the same, depending on the hub/tip ratio, the profile generated at mid radius by a given vortex and/or source distribution is the same in both the two- and three-dimensional flows. Hence, this was used as a starting point in obtaining a relation between the known blade geometry and the required singularity distribution for the equivalent discrete case.

2.3 Application of the Theory

2.3.1 Relating the Model to an Actual Blade.

2.3.1.1 *An Equivalent Two-Dimensional Discrete Singularity Representation*. The definition of an equivalent discrete singularity representation for a specified blade geometry must first be established. The method of graphically dividing the area under a plot of the continuous singularity distribution function into discrete singularities as described previously is commonly considered an equivalent representation. Although this technique certainly represents the overall blade characteristics, it is a rather arbitrary procedure and some question existed concerning how accurately it reproduces the details of the flow at each point on the actual blade surface. Since the present work was concerned with comparing specific details of the flow, the blade surface pressure distribution in particular, an alternative method which better defined these surface velocities was desirable.

Conditions established by Falkner (28) for a two-dimensional blade profile were used to determine the distribution of discrete vortices which was considered to be equivalent to a specified continuous vorticity distribution. First, the velocity perturbations induced by both the discrete and continuous vortex distributions at selected points must be equal. Second, the sum of the strengths of the discrete vortices must be equal to the integrated strength of the continuous vorticity distribution. Extending this method to include blade thickness, the discrete and continuous source distribution must also satisfy the first condition. The second condition for this case is that the sum of the source strengths must be zero. This method insures that the flows modeled by both the discrete and continuous distributions will be identical at least at the selected points. Further, since the flow variations over most practical profiles are smooth and continuous, the velocities induced at all intermediate points should be approximately the same also.

2.3.1.2 Influence Coefficient Method. In order to investigate the relationship between a given two-dimensional blade profile and the equivalent discrete vortex and source representation of the three-dimensional turbomachine blade, a variation of Falkner's technique was used. The two-dimensional blade profile at mid radius was decomposed into a staggered, symmetrical thickness at zero incidence, and a lifting, staggered camber line (actually 0.03 in. thick) at incidence (Figure 9). The non-dimensional velocity perturbations induced due to the camber $(\underline{U}_v)_2$ and the thickness $(\underline{U}_s)_2$ at selected points ℓ on the profile surface

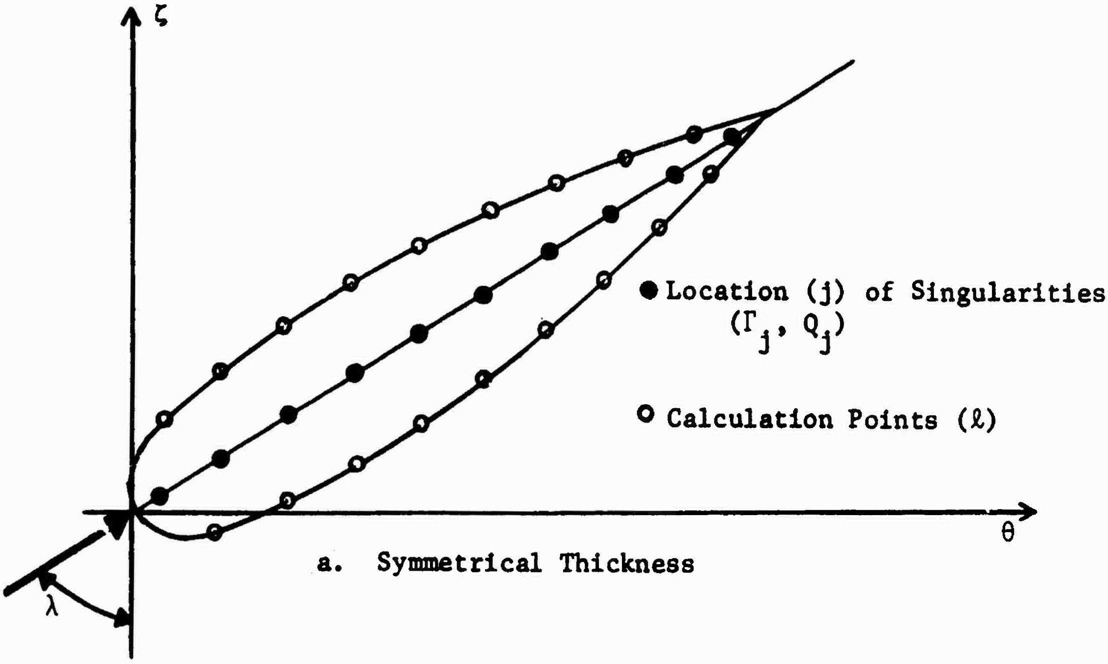

a. Symmetrical Thickness

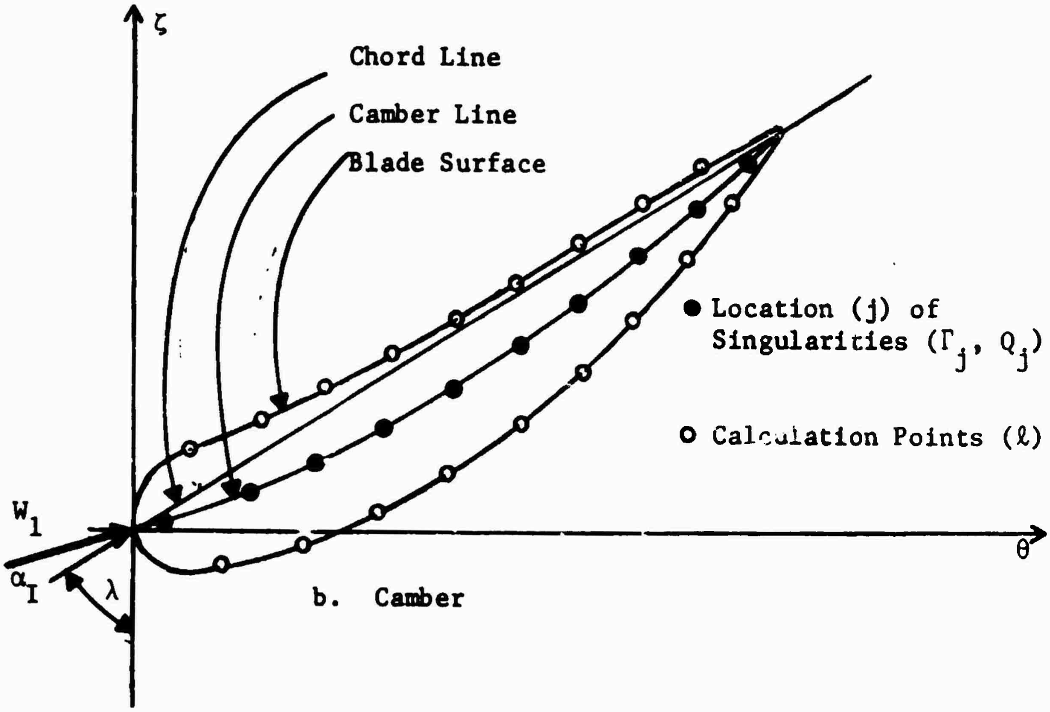

b. Camber

Figure 9. Decomposition of Profile for Influence Coefficient Calculations.

were then calculated using the Douglas Neumann cascade program (23). Location of the calculation points for the velocity perturbations on the profile surface rather than on the camber line provided better accuracy for two reasons. First, the three-dimensional method was found to be unreliable very close to the singularities due to a lack of convergence of the solution. Second, the flow field close to a discrete singularity distribution is different from that due to an equivalent continuous airfoil as discussed further in Paragraph 2.3.3. Also, the two-dimensional circulation $(\Gamma_M)_2$ was calculated. This program was assumed to provide the velocities induced by the continuous two-dimensional vortex and source distribution since the solution approaches the exact solution if a sufficient number of coordinates are specified. Concurrently, the two-dimensional discrete singularity portion of the program reported by Tamura et al. (26) was run for this same geometry, but the strength of each discrete vortex and source was arbitrarily set equal to unity. Thus, the velocity components due to these two-dimensional unit singularities were calculated at the same points ℓ as above, and were defined as influence coefficients $G_{\ell,j}$ and $S_{\ell,j}$ for the vortex and source, respectively. These influence coefficients specify the velocity components induced at a point ℓ due to a unit singularity at a point j. Hence, using the components of the velocity perturbations $(\underline{U}_v)_2$ and $(\underline{U}_s)_2$ and the circulation $(\Gamma_M)_2$ calculated from the Douglas Neumann program, the equivalent two-dimensional discrete vortex $(\Gamma_{jM})_2$ and source $(Q_{jM})_2$ distributions for the mid radius profile were obtained from the following set of matrix equations,

$$\left.\begin{array}{l} u_{v\ell} = \sum_j (G_{\ell,j})_2 (\Gamma_{jM})_2, \\ \\ \sum_j (\Gamma_{jM}) = (\Gamma_M)_2, \end{array}\right\} \begin{array}{ll} \ell = 1, \; . \; . \; . \; N & (20) \\ \\ j = 1, \; . \; . \; . \; N + 1 & (21) \end{array}$$

$$\left.\begin{array}{l} u_{s\ell} = \sum_j (S_{\ell,j})_2 (Q_{jM})_2, \\ \\ \text{and} \quad \sum_j (Q_{jM})_2 = 0. \end{array}\right\} \begin{array}{ll} \ell = 1, \; . \; . \; . \; N & (22) \\ \\ j = 1, \; . \; . \; . \; N + 1 & (23) \end{array}$$

These scalar equations were solved for Γ_j and Q_j using standard FORTRAN scientific subroutines.for matrix inversion. Any number of calculation points may be considered, but the complexity of the inversion process increases rapidly with the size of the matrix. The specific points j and ℓ used in these calculations are presented in Table 2 and Figure 9.

No general rule can be offered for determining the number of singularities needed to get a valid approximation of the real blade flow field. Typically, the required number increases with increasing camber, thickness, and chord, and decreases with increasing distance of the calculation points from the blade surface. The technique used here was to intuitively select a small number of singularities (say 5), and then increase this number as necessary to get a smooth distribution of flow properties. For the cases tested, ten singularities gave a reasonably smooth pressure distribution. Five singularities were considered too few since a pressure distribution with sharp peaks and valleys resulted.

Numerical calculations were carried out using the geometry of the two-bladed rotor described by Bowerman (24). This rotor had a hub/tip

Table 2

DEFINITION OF THE POINTS USED FOR THE INFLUENCE COEFFICIENT CALCULATIONS

ℓ	Velocity Component	Position	j	Singularity Location
1	u_ζ	10% chord (upper surface)	1	5% chord
2	u_θ	10% " "	2	15% "
3	u_ζ	50% " "	3	25% "
4	u_θ	50% " "	4	35% "
5	u_ζ	90% " "	5	45% "
6	u_θ	30% chord (lower surface)	6	55% "
7	u_ζ	30% " "	7	65% "
8	u_θ	70% " "	8	75% "
9	u_ζ	70% " "	9	85% "
			10	95% "

ratio of 0.6, a mid radius stagger angle of 66.4°, and was designed by two-dimensional theory to have a constant circulation at all radii (i.e., free vortex). Since the two-dimensional profiles at the hub, mid, tip and other radii were specified, the influence coefficient method was utilized to determine the discrete vortex distribution at the mid radius $(\Gamma_{jM})_2$ which, due to the free vortex design, also requires

$$(\Gamma_{jM})_2 = (\Gamma_{jH})_2 = (\Gamma_{jT})_2 = (\Gamma_j)_2 \quad . \tag{24}$$

Further, since the two- and three-dimensional solutions are the same at the mid radius,

$$(\Gamma_{jM})_3 = (\Gamma_{jM})_2 = (\Gamma_j)_2 \tag{25}$$

and since the three-dimensional theory considered in this thesis is restricted to constant circulation strength radially, then,

$$(\Gamma_{jM})_3 = (\Gamma_{jH})_3 = (\Gamma_{jT})_3 = (\Gamma_j)_3 \quad . \tag{26}$$

Hence, the three-dimensional velocity perturbations and the profile slopes generated by this value of $(\Gamma_j)_3$ were calculated at several points for the hub and tip sections. From this data, the three-dimensional profiles at hub and tip were constructed graphically and were compared with the given two-dimensional profiles. Due to the large variation of properties near the leading edge and plotting inaccuracy, the accuracy of the profile shape found by this graphical method was poor. However, a definite qualitative trend was discernable. From this comparison of the profiles generated by both the two- and three-dimensional theories for a given discrete vortex distribution, it was determined that the three-dimensional hub profile had a greater camber than the two-dimensional profile, while the three-dimensional tip profile had less camber than the two-dimensional profile.

2.3.1.3 An Equivalent Three-Dimensional Discrete Singularity Representation. The two-dimensional discrete vortex distribution at the mid radius $(\Gamma_{jM})_2$ was determined by requiring that

$$\left(\sum_{j=1}^{JVS} \Gamma_{jM}\right)_2 = (\Gamma_M)_2 \qquad (27)$$

and by equating the velocity perturbations induced by the two-dimensional discrete and continuous vortex distributions at several selected points. Furthermore, the axial and tangential velocity perturbations predicted by both the two- and three-dimensional discrete singularity solutions are the same at the mid radius (Table 1). Hence, the blade profile is accurately specified at the mid radius where the two- and three-dimensional solutions are the same, or

$$(\Gamma_{jM})_3 = (\Gamma_{jM})_2 \quad \text{for } j = 1, JVS \qquad (28)$$

Similarly, for the source distribution,

$$(Q_{jM})_3 = (Q_{jM})_2 \quad \text{for } j = 1, JVS \qquad (29)$$

However, since the two- and three-dimensional solutions are not the same at other radii, it follows from the previous work that, at radii other than the mid radius, a fixed blade geometry will not be represented by the same singularity distribution in both a two-dimensional and three-dimensional flow field. For example, a singularity distribution obtained by cascade methods and corresponding to a specified two-dimensional profile will not generate the same geometry when utilized in a three-dimensional flow. The practical usefulness of the three-dimensional analysis is dependent upon specifying a three-dimensional singularity distribution which will model blade geometry specified in terms of a stack up of two-dimensional profiles. Hence, a relationship between given blade geometry and the required discrete singularity representation at radii other than the mid radius was needed. This was accomplished by equating the slope of the profile surfaces in both the three- and two-dimensional flows. An equivalent $(\Gamma_j)_3$ representing a given profile in a three-dimensional flow must induce three-dimensional velocity perturbations such that the slope of the camber line is the same as in the two-dimensional flow, or

$$\left(\frac{dy}{dx}\right)_2 = \left(\frac{dy}{dx}\right)_3 \tag{30}$$

and

$$\frac{(W_m)_\theta + (u_{v_\theta})_2}{(W_m)_\zeta + (u_{v_\zeta})_2} = \frac{(W_m)_\theta + (u_{v_\theta})_3}{(W_m)_\zeta + (u_{v_\zeta})_3} \tag{31}$$

at several selected points ℓ.

Before applying these techniques to a numerical calculation, some further discussion is needed. Since the three-dimensional theory requires that each vortex line have a constant strength radially, it was necessary to assume that

$$(\Gamma_{jM})_3 = (\Gamma_{jH})_3 = (\Gamma_{jT})_3 \tag{32}$$

Thus, the three-dimensional velocity perturbations induced at the hub and tip (or any other radius) may be calculated since $(\Gamma_{jM})_3$ is known. The influence coefficient technique was applied again here, by using the two-dimensional singularity portion of the computer program of Reference 21. The two-dimensional velocity components at the hub and tip were calculated for unit singularities $(\Gamma_{jH})_2$ and $(\Gamma_{jT})_2$, and these velocity components used as influence coefficients $G_{\ell,j}$ as before. Then, the two-dimensional perturbation velocity components due to the vortices may in general be expressed as,

$$(u_{v\ell})_2 = \sum_{j=1}^{JVS} (G_{\ell,j})_2(\Gamma_j)_2 \qquad (33)$$

By a similar line of reasoning for the source case,

$$(u_{s\ell})_2 = \sum_{j=1}^{JVS} (S_{\ell,j})_2(Q_j)_2 \qquad (34)$$

Substituting the known three-dimensional velocity perturbation components calculated as described above into Equations (33) and (34), then the resulting set of equations may be solved by standard matrix inversion methods for the two-dimensional discrete singularities $(\Gamma_j)_2$ (or $(Q_j)_2$). The results of an example numerical calculation following this procedure are plotted in Figure 10 for vortex and source distributions, respectively, similar to those for the three-bladed rotor described later. Configurations were considered with $(W_m)_\theta$ and $(W_m)_\zeta$, which were assumed to be the same in both the two- and three-dimensional case, adjusted to correspond to a 10° and 80° stagger at zero incidence. The flow field was evaluated at ten points for each of the hub/tip ratios 0.300, 0.442, 0.600. It should be remarked here that the values of $(\Gamma_2 - \Gamma_3)\eta\nu/\Gamma_3$ collapsed into a single curve, as shown in Figure 10, for all values of ν. Hence the three-dimensional effects are inversely proportional to ν. Furthermore, the three-dimensional effects are larger near the hub ($\eta = \nu$) than at the tip ($\eta = 1$). For example for $\nu = 0.4$, $\eta = 0.4$, and $\lambda = 80^\circ$, $(\Gamma_2 - \Gamma_3)/\Gamma_3$ is 18.75 percent, which is appreciable.

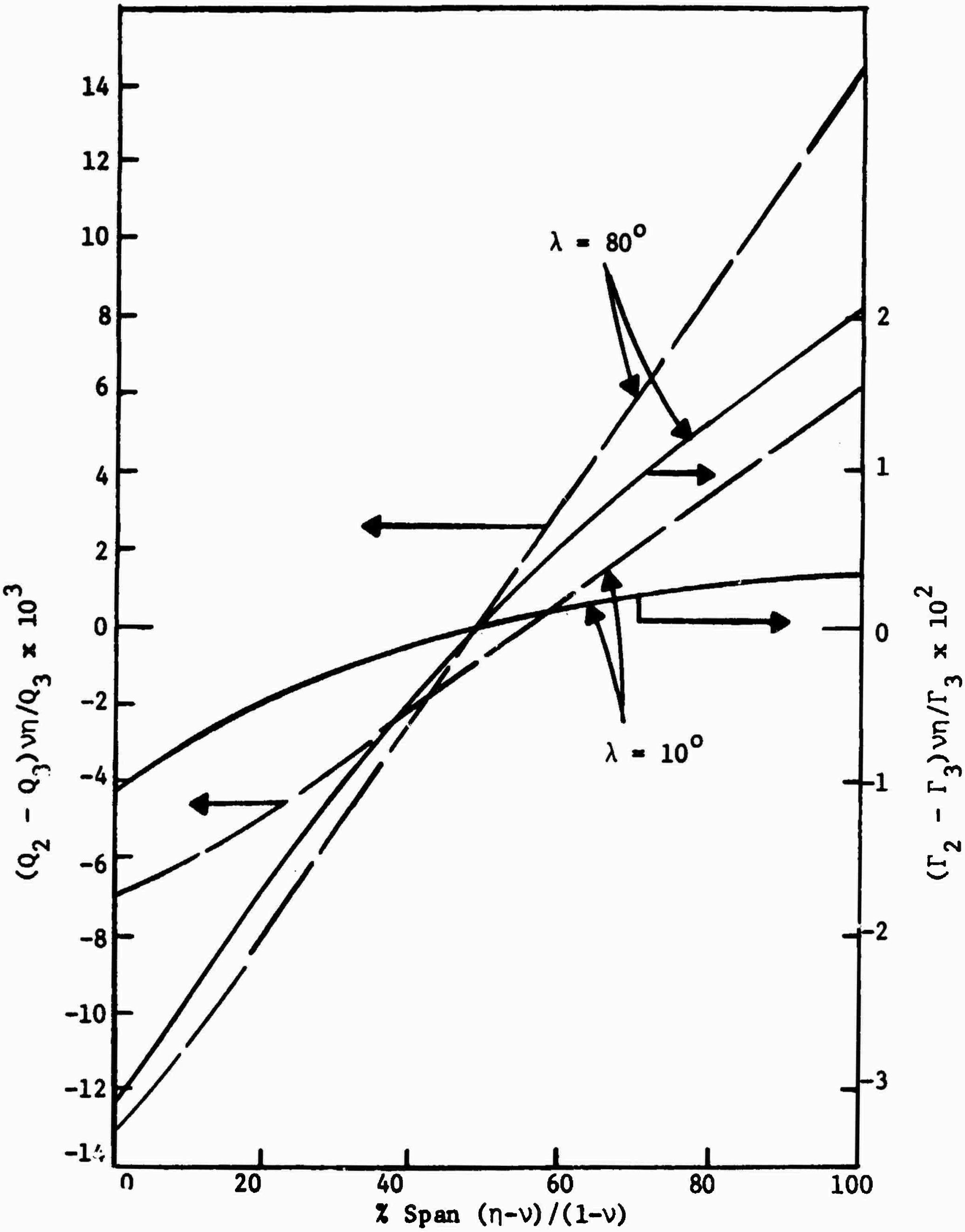

Figure 10. Comparison of Vortex and Source Strengths Required to Generate Same Slope in Both Two- and Three-Dimensional Flow Fields.

The three-dimensional test case investigated herein and described later has a free vortex distribution, but the two-dimensional test case has varying circulation. Nevertheless, the blades used in both cases have the same profile. Near the hub, the three-dimensional effects generate a larger circulation around the blades than in a two-dimensional flow case. This trend is reversed at the tip. This difference is inversely proportional to the hub/tip ratio (ν). These effects are the same for both vortex and source calculations.

In order to calculate the performance of the test rotor, the actual blade profile coordinates at five radial positions along the span as well as the corresponding flow inlet parameters were input to the Douglas Neumann cascade program. Using the calculated two-dimensional velocity perturbations due to the camber and thickness effects at ten points on the profile surface, a set of matrix equations similar to Equations 20 through 23, but employing three-dimensional influence coefficients, were solved to determine the three-dimensional discrete $(\Gamma_{jM})_3$ and $(Q_{jM})_3$. These singularity distributions were then used in the three-dimensional potential flow program to predict the pressure distributions, which will be discussed in a later section.

A basic assumption made in the influence coefficient method as applied here was that the two- and three-dimensional singularities are located at the same coordinates and only the strength of the singularities was assumed to vary. In actuality, not only the strength but also the location of these singularities varies between the two- and three-dimensional theories. However, the effect of the positional variation is proven to be negligible in the Appendix.

2.3.2 Comparison of the Two- and Three-Dimensional Performance Prediction. At this point, a fundamental difficulty which recurs throughout this work must be noted. The designation of free vortex used by Bowerman (24) implies, as it does typically, that the circulation generated by the blade is constant at each radius based on two-dimensional theoretical calculations. In view of what has been qualitatively developed thus far, this does not imply that a constant circulation is actually generated from hub to tip in a three-dimensional flow configuration. Thus, a blade designed two-dimensionally to free vortex conditions is not truly a free vortex blade by three-dimensional criteria. Further complicating the analysis, the three-dimensional theory is restricted to blades which are free vortex by three-dimensional criteria. Hence, some manipulation has been necessary to arrive at meaningful comparisons.

At the mid radius, the velocity perturbations induced by the two- and three-dimensional discrete singularities were required to be equal causing both the profile geometry and performance to be identical. At all other radii considered a more relaxed condition was imposed, however, by requiring only the slope (not magnitude) of the two- and three-dimensional local velocity vectors to be equal. Consequently, the profile slopes in the two- and three-dimensional cases were still required to be the same; but the performance of the profile which is proportional to the change in the magnitude of the tangential velocity, or circulation, was permitted to vary. Using the equivalent three-dimensional singularity representation determined as described in Paragraph 2.3.1, the performance was calculated by both the two- and three-dimensional theories for the blade used by Bowerman (24). The circulation predicted by both theories was then compared.

A plot of the ratio Γ_2/Γ_3 for the Bowerman blade, where $\Gamma_2 = \sum_j \Gamma_{2j}$ and $\Gamma_3 = \sum_j \Gamma_{3j}$, is given in Figure 11. This figure shows that, for a hub/tip ratio of 0.600, the given hub profile operating in a two-dimensional flow generates about 6.7% less circulation than when operating in a three-dimensional flow. Conversely, a tip profile operating in a two-dimensional flow generates about 2.9% more circulation than when operating in a three-dimensional flow. The solutions at mid radius differ only by about 0.6%.

To investigate the effect of variation of the hub/tip ratio, the same procedure was repeated for this same rotor geometry but with a hub/tip ratio of 0.300. For this lower hub/tip ratio, the effect is significantly larger. The circulation in the three-dimensional flow is about 20.0% greater at the hub, about 1.4% less at the mid radius and about 6.8% less at the tip. Notice that, although the solutions are practically the same at mid radius for both cases, the two-dimensional theory predicts larger mid radius values and the smaller hub/tip ratio shows more variation. Figure 12 presents similar data for the blade designed by the author and built for this project, but also includes the effect of stagger angle and space/chord ratio. The important rotor parameters are summarized later. It shows that the two-dimensional theory is probably adequate for low space/chord ratios (S/C). Further, the three-dimensional effects become more significant at higher stagger angles. The performance of the hub of a single-bladed (NB = 1) rotor with a stagger of 71 degrees and hub/tip ratio of 0.3, admittedly a rather exaggerated case, would be about 35% greater than predicted by

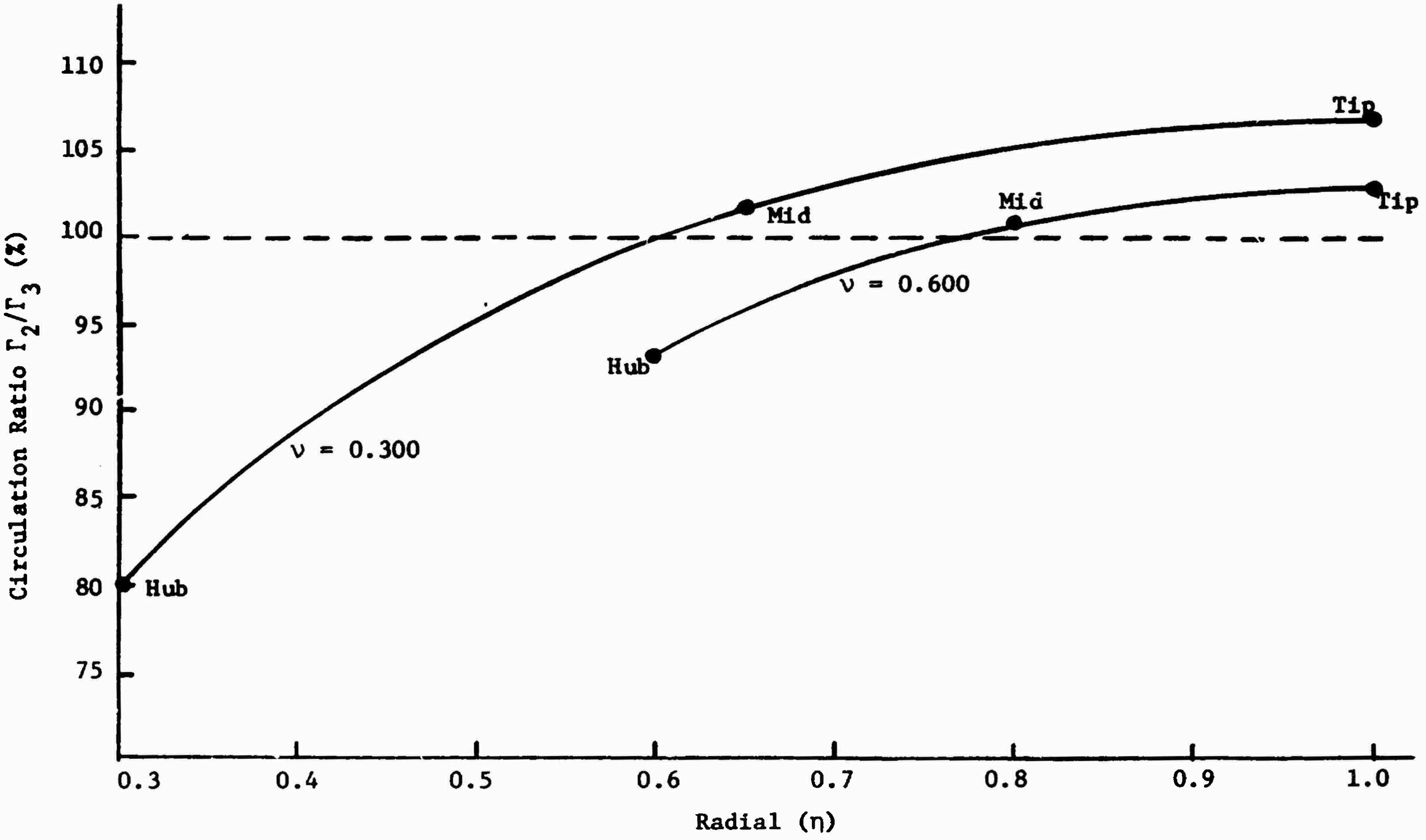

Figure 11. Circulation Ratio to Generate Equal Slopes for Bowerman Blade at Hub/Tip Ratios 0.300 and 0.600.

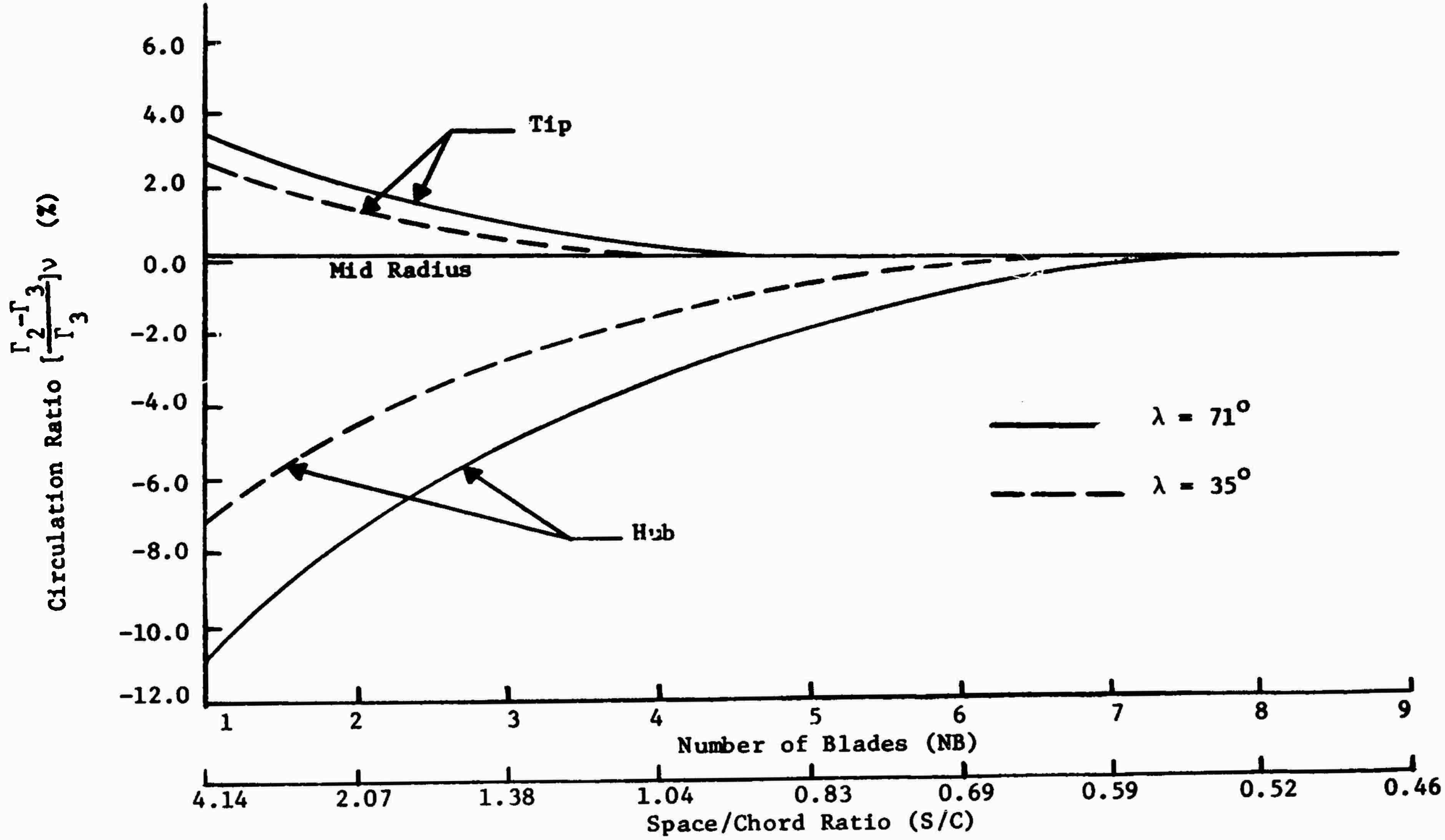

Figure 12. Circulation Ratio (Theoretical) for the Test Rotor Geometry and Variations Thereof.

two-dimensional methods. At the tip, the three-dimensional value would be about 11% less. In either case, the accuracy of the two-dimensional prediction is clearly inadequate. For the actual test rotor, the three-dimensional circulation at the hub is approximately 11.3% greater than the two-dimensional predictions, while at the tip it is approximately 2.3% less. Although the effects are less for this more realistic case, they are still significant.

These results may be interpreted in two distinct, but consistent, ways. First, to mathematically model by three-dimensional theory the hub section of a turbomachine blade which has been specified two-dimensionally, the three-dimensional discrete vortex strength must be greater than that calculated by two-dimensional methods. Conversely, a tip profile must be modeled by a discrete vortex distribution of less strength in the three-dimensional flow. Second, in order to obtain a specified circulation about a turbomachine blade section operating in an actual three-dimensional flow field, the above results show that a two-dimensional hub profile must be designed for a circulation less than the desired value in the actual machine while the tip profile designed by two-dimensional methods must be designed for a circulation greater than the desired value. Thus, the earlier qualitative result has been confirmed.

Although the analysis here assumed a free vortex design, the results may be generalized to relate Γ_2 and Γ_3 generated by a non-free vortex configuration.

The above comparison is based on total circulation, or gross blade performance. A more detailed investigation in the form of pressure distribution versus chord data is needed to give a better understanding of how the three-dimensional effects influence such characteristics as blade lift, moment, and boundary layer growth. This data is presented below for the Bowerman blade geometry.

In Figure 13, the pressure distributions predicted by the two-dimensional cascade and the three-dimensional theories are compared. The experimental data measured by Bowerman is also presented, but discussion will be reserved for Chapter IV. The three-dimensional predictions at each radius agree reasonably well with the two-dimensional predictions near the leading edge on the pressure surface and near the trailing edge on the suction surface. Near the leading edge on the suction surface, the three-dimensional theory predicts a lower pressure and somewhat steeper gradients. Near the trailing edge on the pressure surface, the three-dimensional theory again predicts lower pressures and a somewhat more favorable pressure gradient. C_p distribution on the pressure surface is predicted accurately by three-dimensional theory, especially near the trailing edge.

The Bowerman blade geometry was again used in the calculation of the pressure distribution for a hub/tip ratio of 0.300 so that a comparison of the effect of hub/tip ratio could be made. The technique used was simply to shrink the hub of the annulus, and to extend the root portion of the blade to meet the smaller hub diameter. All of the blade profiles remained at their original radial positions. For example, the tip section ($\eta = 0.95$) for the $\nu = 0.600$ case was also the tip section ($\eta = 0.95$) for the $\nu = 0.300$ case; the hub section ($\eta = 0.65$) for the $\nu = 0.600$ case, although it became the mid radius section for the $\nu = 0.300$ case, was still located at the same radial position ($\eta = 0.65$).

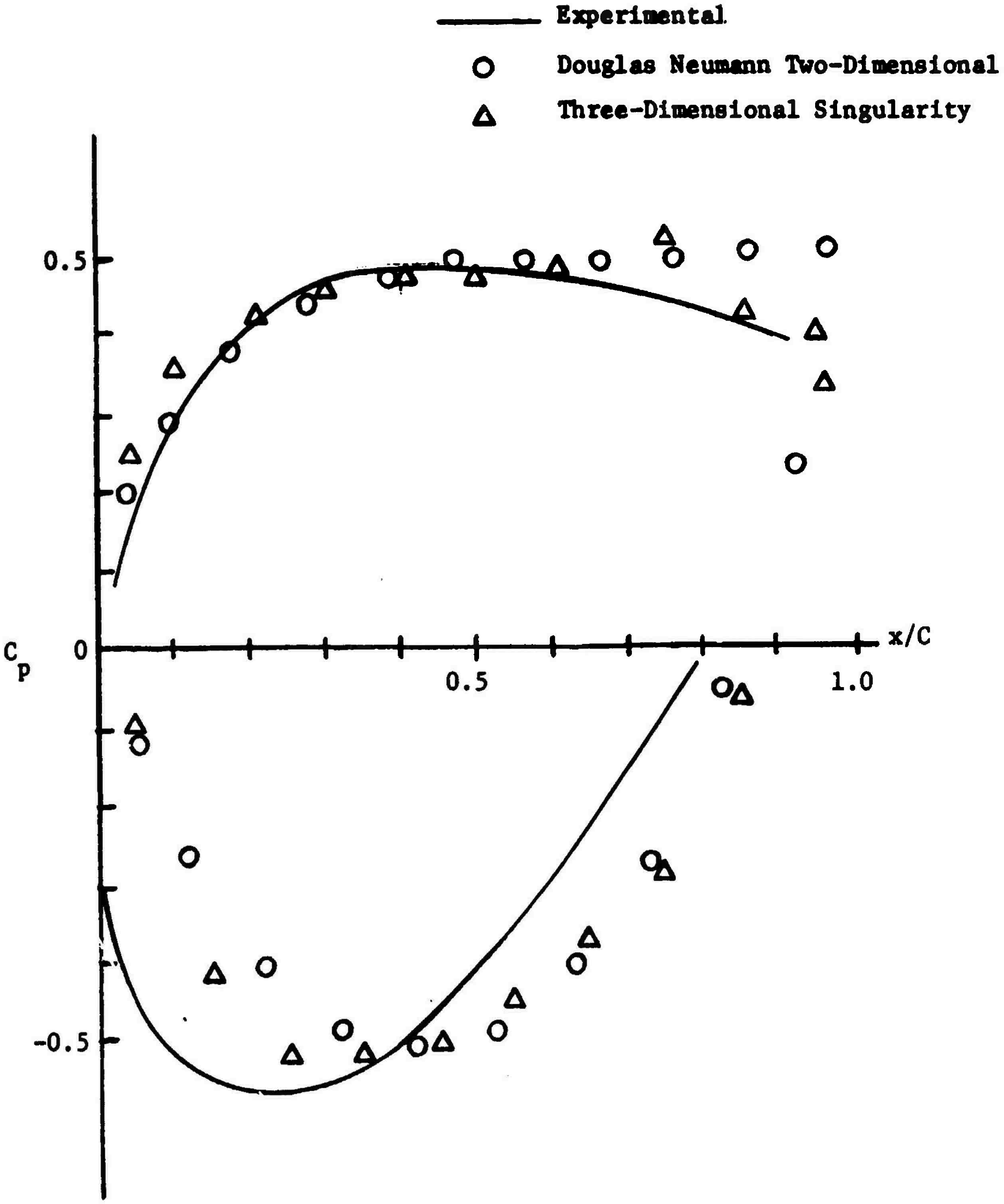

Figure 13a. Blade Static Pressure Coefficient for Bowerman's Blade, $\eta = 0.6$[illegible] (Hub), $\phi_T = 0.284$.

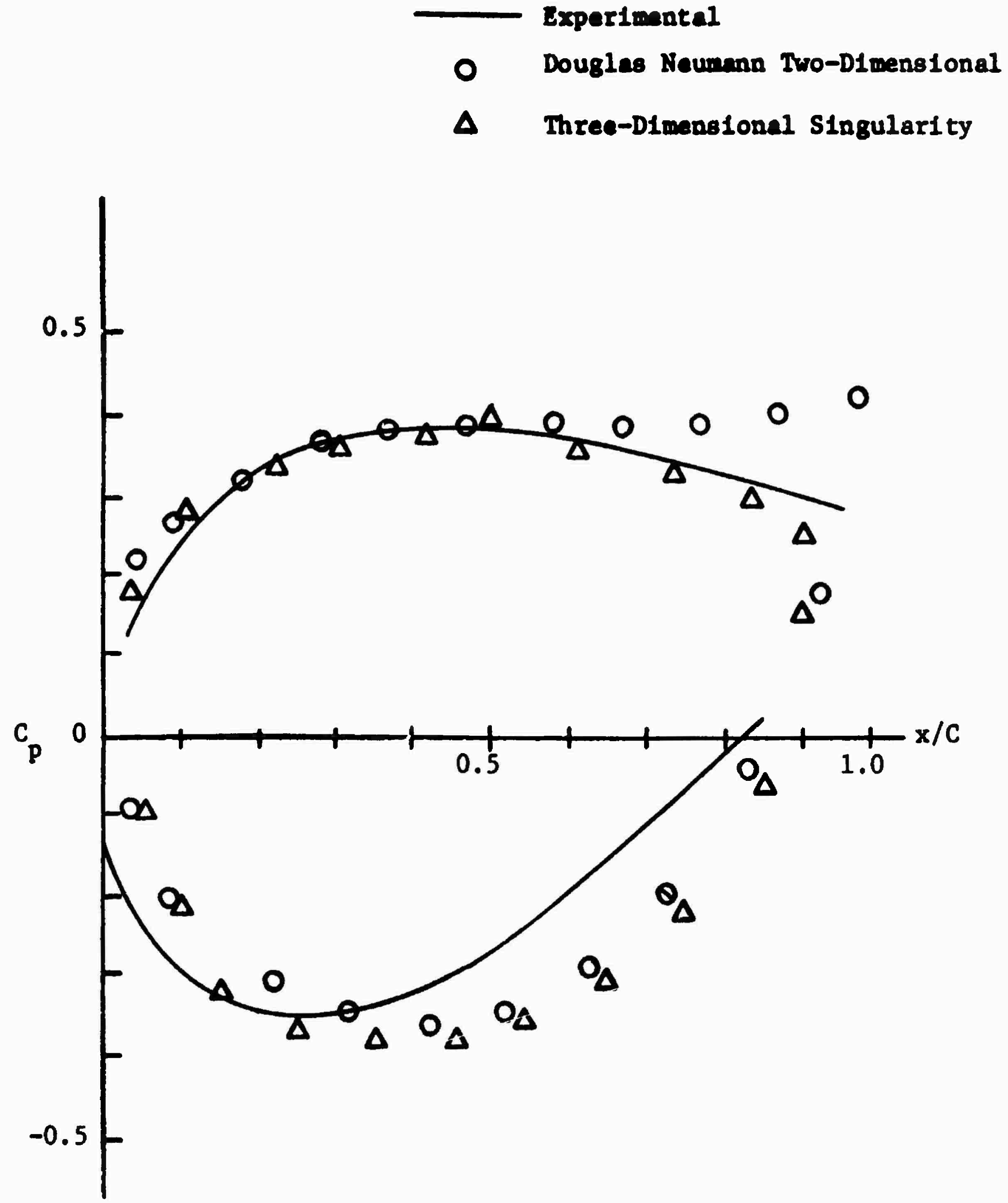

Figure 13b. Blade Static Pressure Coefficient for Bowerman's Blade, $\eta = 0.800$ (Mid-Radius), $\phi_T = 0.284$.

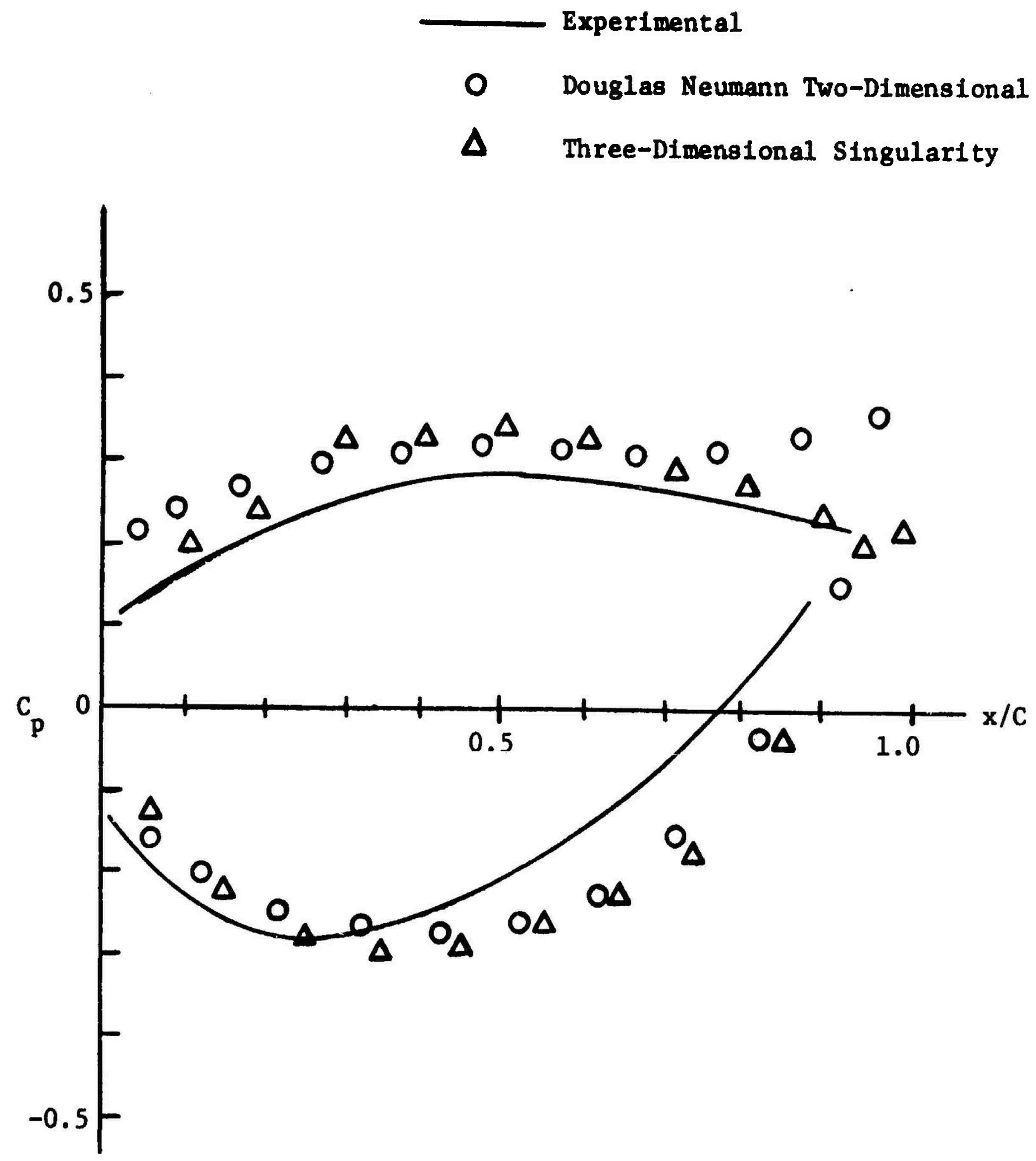

Figure 13c. Blade Static Pressure Coefficient for Bowerman's Blade, $\eta = 0.950$ (Tip), $\phi_T = 0.284$.

Pressure distributions were calculated only for sections lying between $\eta = 0.6$ and $\eta = 1.0$ as before, and the extended portion of the blade between $\eta = 0.3$ and $\eta = 0.6$ was ignored.

The results of this comparison presented in Figure 14 show that the three-dimensional effect is more significant for a low hub/tip ratio configuration. As might have been expected from previous work, since the sections considered are at the mid radius or outboard of it, the performance decreases with the decreasing hub/tip ratio. The decrease in circulation due to three-dimensional effects is larger in the case of a low hub/tip ratio configuration.

Previously, it was shown analytically that a reduction in hub/tip ratio from 0.6 to 0.3 caused the radial velocity perturbations to double near the mid radius. Both the two-dimensional and three-dimensional theoretical predictions of the static pressure distributions on Bowerman's blade agree reasonably well with the experimental data. This indicates that even though radial flows and interference effects are large, their direct influence on the blade pressure coefficient may be less significant.

2.3.3 Three-Dimensional Continuous Singularity Distribution Method

2.3.3.1 Comparison of Discrete and Continuous Cases. It was stated in Paragraph 2.3.1 that the flow field near a camber line due to a series of discrete singularities located on the camber line is different from that due to a continuous distribution. Since sources are used to generate a finite thickness, points of interest are naturally on the surface or in the surrounding flow field. Points inside the profile near the sources are of no practical interest; thus, the discrepancy

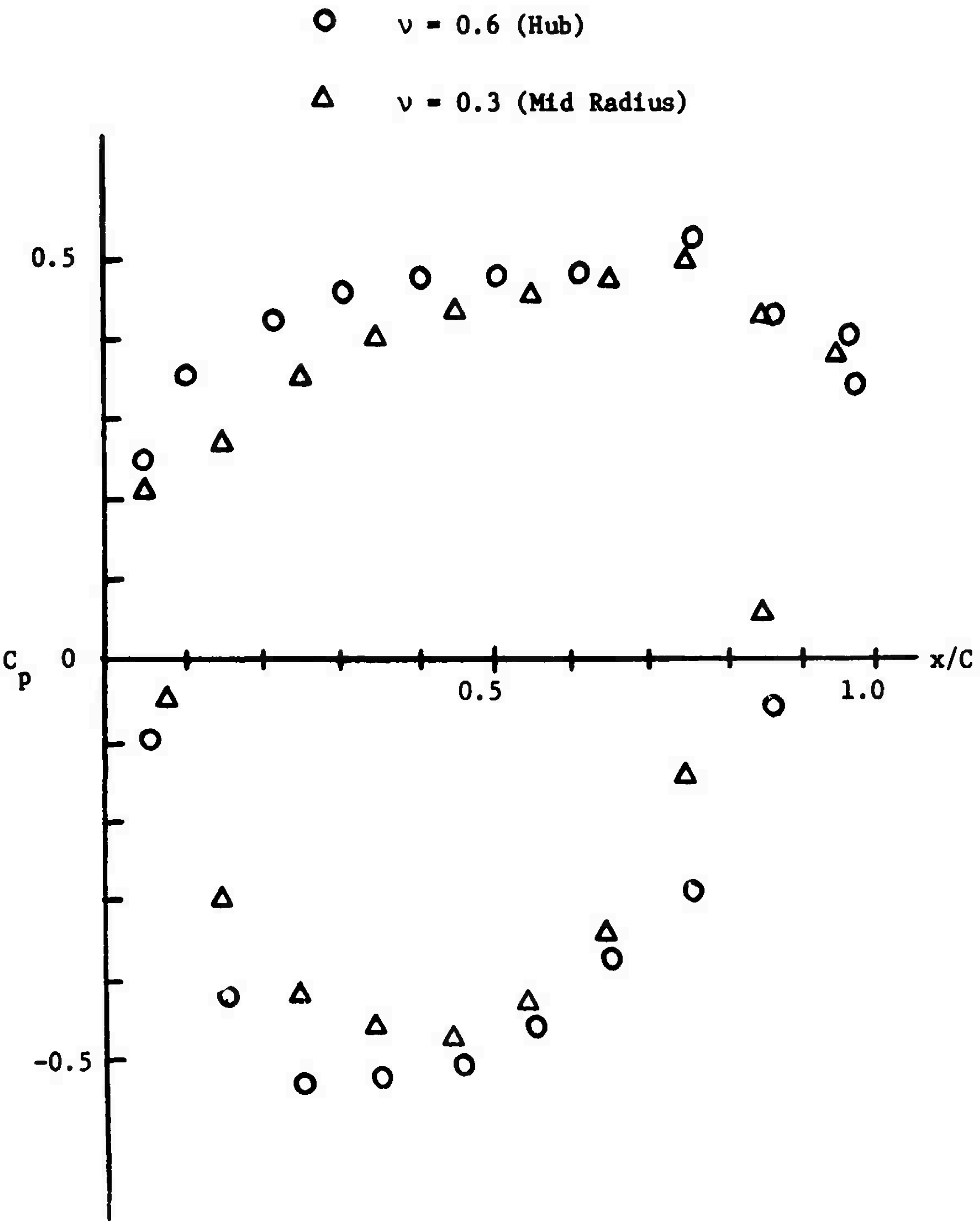

Figure 14a. Effect of Hub/Tip Ratio on Bowerman's Blade as Predicted by Three-Dimensional Singularity Method, $\eta = 0.650, \phi_T = 0.284$.

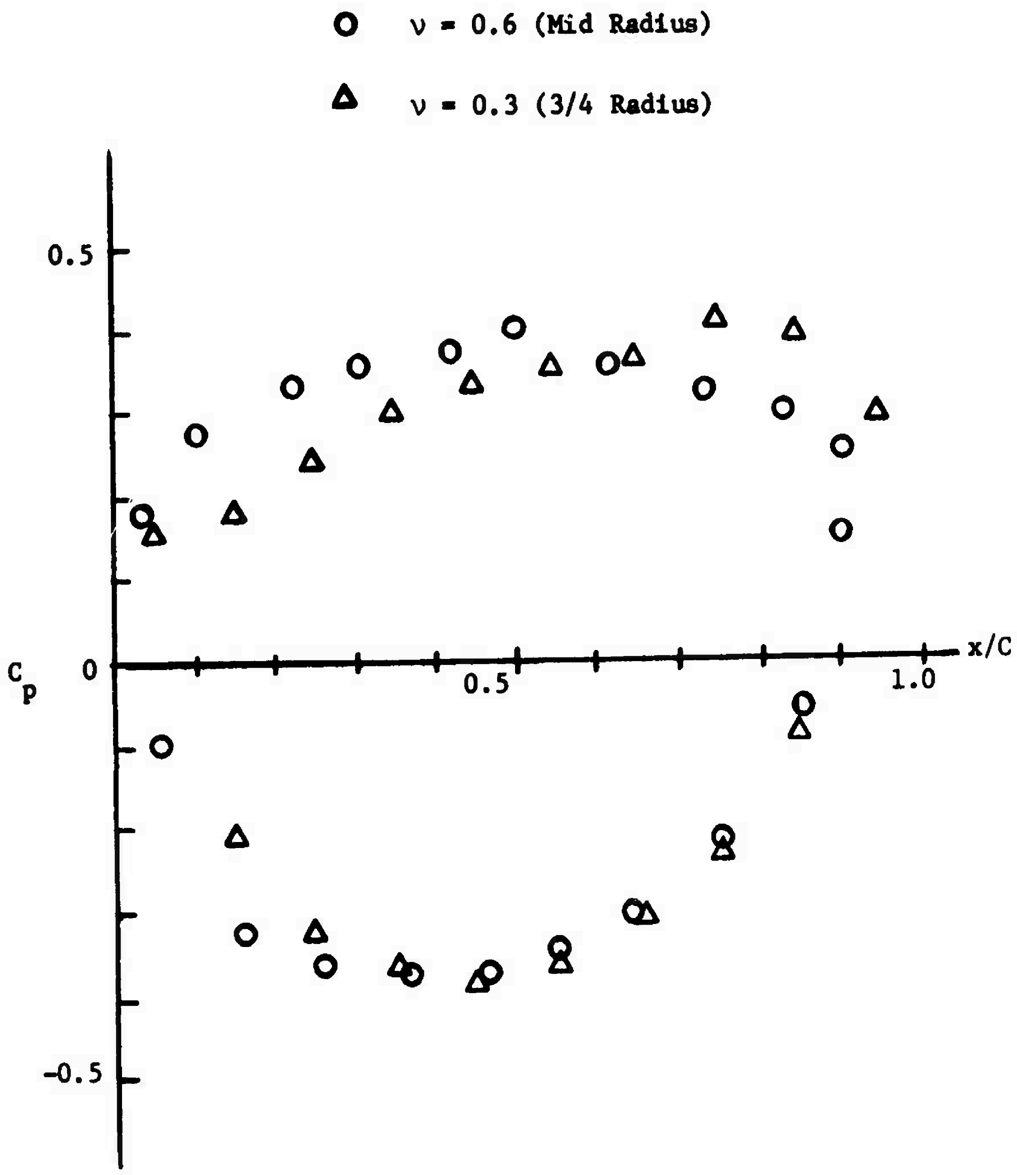

Figure 14b. Effect of Hub/Tip Ratio on Bowerman's Blade as Predicted by Three-Dimensional Singularity Method, $\eta = 0.800, \phi_T = 0.284$.

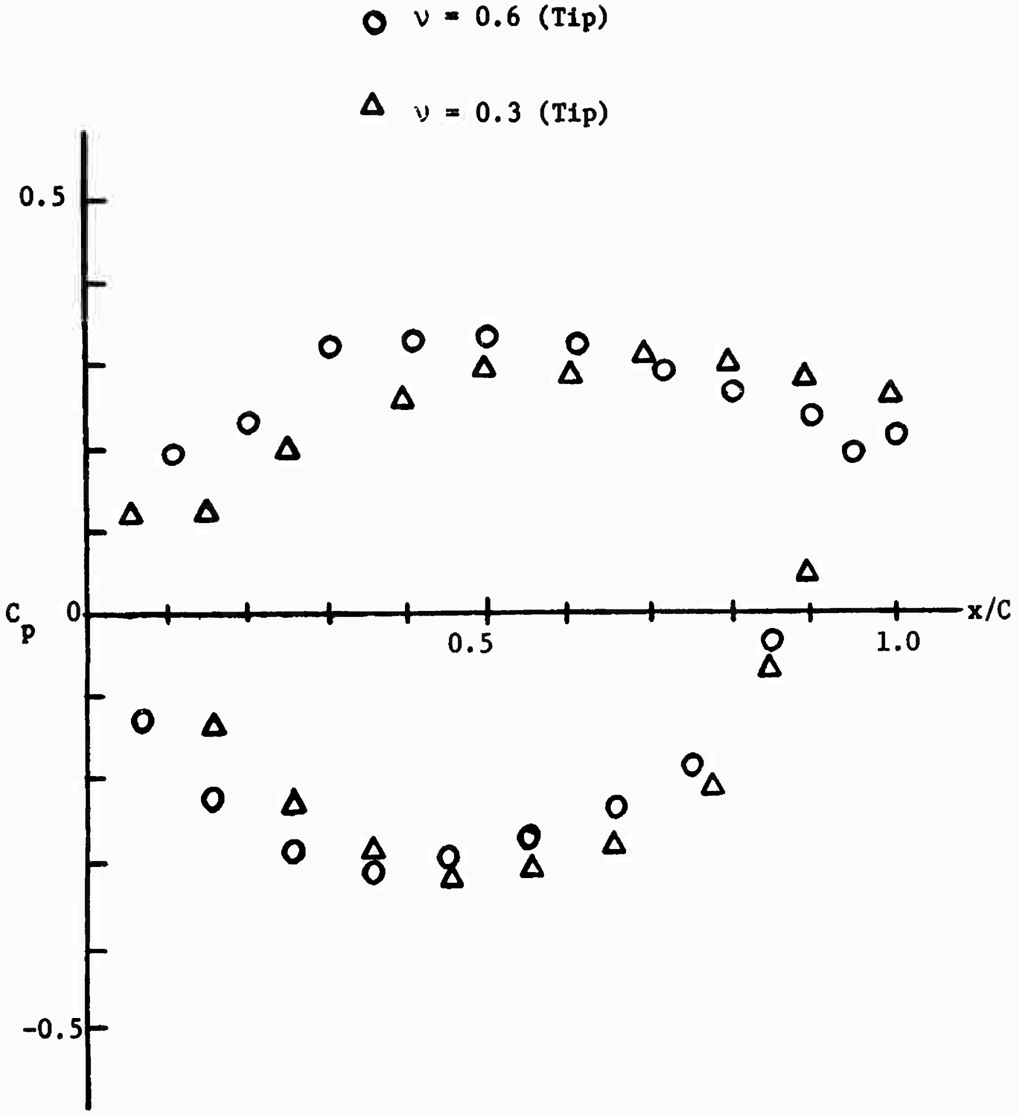

Figure 14c. Effect of Hub/Tip Ratio on Bowerman's Blade as Predicted by Three-Dimensional Singularity Method, $\eta = 0.950, \phi_T = 0.284$.

between the discrete and continuous source is not significant. The vortex, however, needs further consideration.

A continuous distribution of vortices, or a vortex sheet, is characterized by a velocity jump across the sheet at each point which is proportional to the local vortex strength.

Determination of an equivalent discrete vortex distribution is not as simple as it looks. One may, at first glance, conclude that the continuous distribution of vortices can be replaced by discrete vortices such that the total strength is the same and the discrete vortices are located at the centroid of the area under corresponding $\gamma(\xi)$ versus ξ curve where $\gamma(\xi)$ is the local non-dimensional vortex strength. From a simple argument, it can be shown that not only the jump in chordwise velocity is eliminated, at least at some points, but normal velocities may generally occur in the discrete case. Hence the resulting discrete vortex distribution is not identical to the continuous distribution case. Thus, determination of an equivalent discrete representation by matching the conditions near the camber line is not feasible. This led to the technique of adjusting the strengths of the discrete singularities so that they induce at certain points on the profile a velocity perturbation equal to that induced by the continuous vortex sheet.

Since the method of discrete singularities is an approximation to the actual flow, it was desirable to extend the analysis to an exact solution. Thus, the continuous singularity distribution was investigated further.

2.3.3.2 <u>Extension of Three-Dimensional Theory to Include Continuous Singularity Distributions</u>. Tamura's (21) expression for the velocity potential for a discrete vortex distribution is given by Equation

(7). Consider now the case where the discrete non-dimensional vortices Γ_j are replaced by a continuous distribution of non-dimensional vorticity $\gamma(\theta_1^*, \zeta^*)$ and the corresponding discrete non-dimensional position coordinates θ_{1j} and ζ_j have become the continuous non-dimensional coordinates θ_1^* and ζ^*. From the geometry (Figure 1), these position coordinates at the trailing edge, for example, may be expressed as

$$\zeta_t^* = c \cos \lambda \tag{35}$$

and

$$\theta_{1t}^* = \frac{C \sin \lambda}{r} = \frac{c}{\eta} \sin \lambda , \tag{36}$$

where λ = the stagger angle, subscript t refers to the values at the trailing edge, and c is the normalized chord length ($=C/r_t$). Similarly, for any general position ξ, along the chord line, these coordinates are

$$\zeta^* = \zeta^*(\xi, \lambda, f_c) \tag{37}$$

and

$$\theta_1^* = \theta_1^*(\xi, \lambda, f_c, \eta) \tag{38}$$

where $f_c(\xi)$ specifies the camber line distribution along the chord line. Since ζ^* and θ_1^* are not independent functions, then, for a given camber line and stagger angle, the primary variable is (ξ), or the non-dimensional position coordinate along the chord line

$$\zeta^* = \zeta^*(\xi), \ \theta_1^* = \theta_1^*(\xi, \eta) \tag{39}$$

and

$$\gamma = \gamma(\xi),$$

where ξ varies over the range $\xi = 0$ to $\xi = c$.

Consequently, the summation over j in Equation (7) was replaced by an integral over the chord, and the non-dimensional velocity potential for the continuous vortex distribution is

$$\phi_v^* = \mp \frac{NB}{4\pi} \int_0^c d\xi \;\; \gamma(\xi) \; \{\theta + 2 \sum_{\ell=1}^{\infty} \frac{\sin k(\theta - \theta_1^*)}{k}$$

$$\sum_{n=1}^{\infty} \exp\;[\mp K_{kn}(\zeta-\zeta^*)]F_v(K_{kn}\nu)Z_k(K_{kn}\eta)\;\} \qquad (40)$$

where the limits of integration are from the blade leading edge ($\xi = 0$) to the trailing edge ($\xi = c$).

Differentiating the velocity potential, the non-dimensional tangential, radial, and axial velocity components are,

$$u_{v\theta}^* = \mp \frac{NB}{4\pi\eta} \int_0^c d\xi \;\; \gamma(\xi) \; \{1 + 2 \sum_{\ell=1}^{\infty} \cos k\;(\theta - \theta_1^*) \quad . \qquad (41)$$

$$\sum_{n=1}^{\infty} \exp\;[\mp K_{k\eta}(\zeta-\zeta^*)]F_v(K_{\kappa\eta}\nu)Z_k(K_{kn}\eta)\} \;,$$

$$u_{v\eta}^* = \mp \frac{NB}{2\pi} \int_0^c d\xi \;\; \gamma(\xi)\{ \sum_{\ell=1}^{\infty} \frac{\sin k\;(\theta - \theta_1^*)}{k} \quad . \qquad (42)$$

$$\sum_{n=1}^{\infty} \exp\;[\mp K_{k\eta}(\zeta-\zeta^*)]F_v(K_{kn}\nu)\frac{\partial Z_k(K_{kn}\eta)}{\partial\eta}\;\} \quad ,$$

and

$$u_{v\zeta}^* = \frac{NB}{2\pi} \int_0^c d\xi \;\; \gamma(\xi) \; \{ \sum_{\ell=1}^{\infty} \frac{\sin k\;(\theta - \theta_1^*)}{k} \quad . \qquad (43)$$

$$\sum_{n=1}^{\infty} K_{kn} \exp\,[\mp K_{kn}(\zeta-\zeta^*)]\,F_v(K_{kn}\nu)\,Z_k(K_{kn}\eta)\}$$

where ζ, ζ^*, θ_1^*, θ_1 are all functions of ξ. θ^*, ζ^* correspond to the location of the vortices and ζ and θ are points at which the velocities are computed.

Similarly, the equation for the non-dimensional velocity potential for a continuous source distribution is

$$\phi_s^* = \frac{NB}{4\pi} \int_0^c d\xi\,\{\pm \frac{2(\zeta-\zeta^*)}{1-\nu^2} \int_\nu^1 q\,(\eta,\xi)\,d\eta$$

$$-\sum_{n=2}^{\infty} \exp\,[\mp K_{on}(\zeta-\zeta^*)]\,\frac{F_s^*(K_{on},\nu,\xi)}{K_{on}}\,Z_o\,(K_{on},\eta)$$

$$-\,2 \sum_{\ell=1}^{\infty} \cos k\,(\theta-\theta_1^*) \sum_{n=1}^{\infty} \exp\,[\mp K_{kn}(\zeta-\zeta^*)]\;.$$

$$\frac{F_s^*(K_{kn},\nu,\xi)}{K_{kn}}\,Z_k\,(K_{kn},\eta)\}\,, \tag{44}$$

where

$$F_s^*(K_{kn},\nu,\xi) = \frac{\int_\nu^1 q(\xi,\eta)\,Z_m(K_{mn}\eta)\,d\eta}{\int_\nu^1 \eta\,Z_m^2(K_{mn}\eta)\,d\eta}$$

Differentiating Equation (44) the following expressions for the tangential, radial, and axial velocity components can be derived.

$$u^*_{s\theta} = \mp \frac{NB}{2\pi\eta} \int_0^c d\xi \; \{ \sum_{\ell=1}^{\infty} k \sin k\,(\theta-\theta_1^*) \;. \tag{45}$$

$$\sum_{n=1}^{\infty} \exp\,[\mp K_{kn}(\zeta-\zeta^*)] \;\frac{F_s^*(K_{kn},\nu,\xi)}{K_{kn}} - Z_k\,(K_{kn},\eta)\} \;,$$

$$u^*_{s\eta} = -\frac{NB}{4\pi} \int_0^c d\xi \{ \sum_{n=2}^{JVS} \exp\,[\mp K_{on}(\zeta-\zeta^*)]\; \frac{F_s^*(K_{on},\nu,\xi)}{K_{on}} \;\frac{\partial Z_o(K_{on},k)}{\partial\eta}$$

$$+ \, 2 \sum_{\ell=1}^{\infty} \cos k\,(\theta-\theta_1^*) \sum_{n=1}^{\infty} \exp\,[\mp K_{kn}(\zeta-\zeta^*)] \;.$$

$$\frac{F_s^*(K_{kn},\nu,\xi)}{K_{kn}} \;\frac{\partial Z_k(K_{kn},\eta)}{\partial\eta} \} \;, \tag{46}$$

and

$$u^*_{s\zeta} = \frac{NB}{4\pi} \int_0^c d\xi \; \{ \pm \frac{2}{1-\nu^2} \int_\nu^1 q(\eta,\xi)\,d\eta \pm \sum_{n=2}^{\infty} \exp[\mp K_{on}(\zeta-\zeta^*)$$

$$\cdot \; F_s^*(K_{on},\nu,\xi) Z_o(K_{on},\eta) \pm 2 \sum_{\ell=1}^{\infty} \cos k\,(\theta-\theta_1^*) \tag{47}$$

$$\cdot \sum_{n=1}^{\infty} \exp\,[\mp K_{kn}(\zeta-\zeta^*)] F_s^*(K_{kn},\nu,\xi) Z_k(K_{kn},\eta)\} \;.$$

The integrands of these velocity expressions contain kernel functions which are composed of various combinations of K_{kn}, F_v, F_s, Z_k, sin, cos, and exponent terms. Since each of these is a numerical function which is tabulated during the execution of the three-dimensional program, the kernal functions are specified. Further, for any given flow situation, the geometry and calculation points η, ζ and θ are fixed constants. Thus, if the singularity distribution function is known, these equations may be integrated numerically. This extension to a continuous distribution of singularities has been included in the computer program used to model the three-dimensional potential flow about a body spanning an annulus. Thus, a tool is available for more accurately predicting the three-dimensional flow, and for evaluating what errors may be introduced by the simplified discrete singularity model.

A comparison of the three-dimensional pressure coefficients predicted using both a continuous and an equivalent discrete vortex distribution is presented in Figure 15. A continuous distribution was assumed and then the equivalent discrete vortices were calculated using the influence coefficient technique. Although both predictions agree well, a tendency for the discrete case to concentrate vorticity near the mid chord at the expense of the leading and trailing edge regions is apparent. The plot shown is for the mid radius but is typical of other radii.

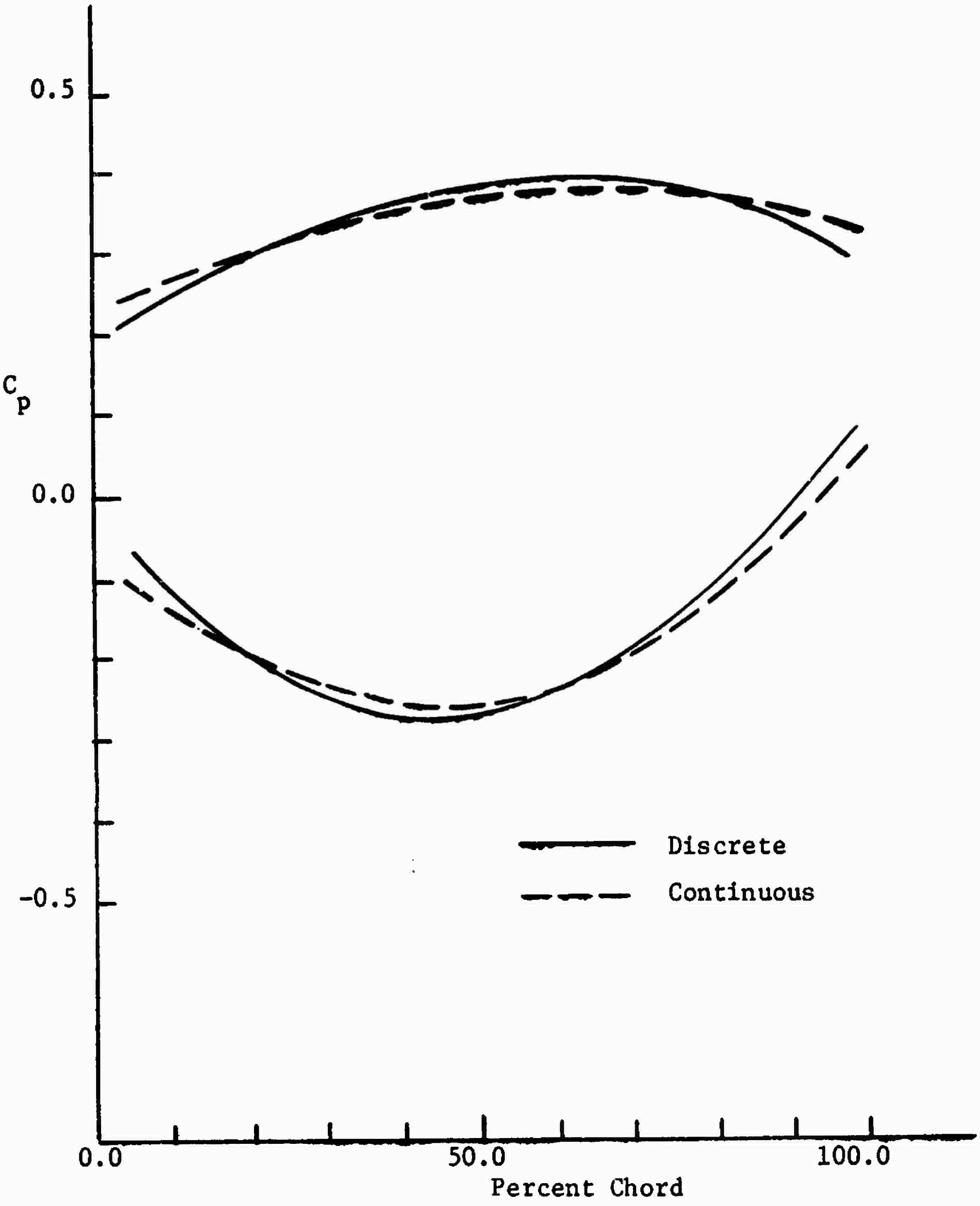

Figure 15. Comparison of Three-Dimensional Static Pressure Coefficients Predicted by Continuous and Equivalent Discrete Vortex Distributions (Mid Radius).

CHAPTER III

EXPERIMENTAL PROGRAM AND RESULTS

In order to verify the theoretical calculations of the flow field, two sets of experimental data were compared with the cascade and three-dimensional theoretical predictions. The pressure distribution over a two-bladed rotor with a hub/tip ratio of 0.6 had been measured by Bowerman (24). Further, a three-bladed rotor with a hub/tip ratio of 0.442, designed to produce large three-dimensional effects, was built at The Pennsylvania State University in order to conduct a more extensive experimental study. The experimental tests with this rotor were accomplished in the Axial Flow Research Fan facility located at the Garfield Thomas Water Tunnel (Figure 16). The rotor and flow parameters were selected to keep viscous effects to a minimum ($Re \approx 5.0 \times 10^5$ at mid radius) since these effects are not included in the current theory.

3.1 Experimental Apparatus

3.1.1 The Axial Flow Research Fan Facility. The Axial Flow Research Fan (AFRF), which is described in detail by Bruce (29), provides an annular flow passage with a bellmouth inlet and is terminated at the aft end by an exhaust throttle (Figure 16). An anti-rotation vane system projecting upstream from the bellmouth inlet was added to remove rotation that could exist in air that is accelerated from rest into the inlet. The flow passage is 19 2/3 feet long, and is bounded in the test section by a cylindrical hub with a diameter of 9.5 inches and a cylindrical outer casing with a diameter of 21.50 inches. A 70 HP

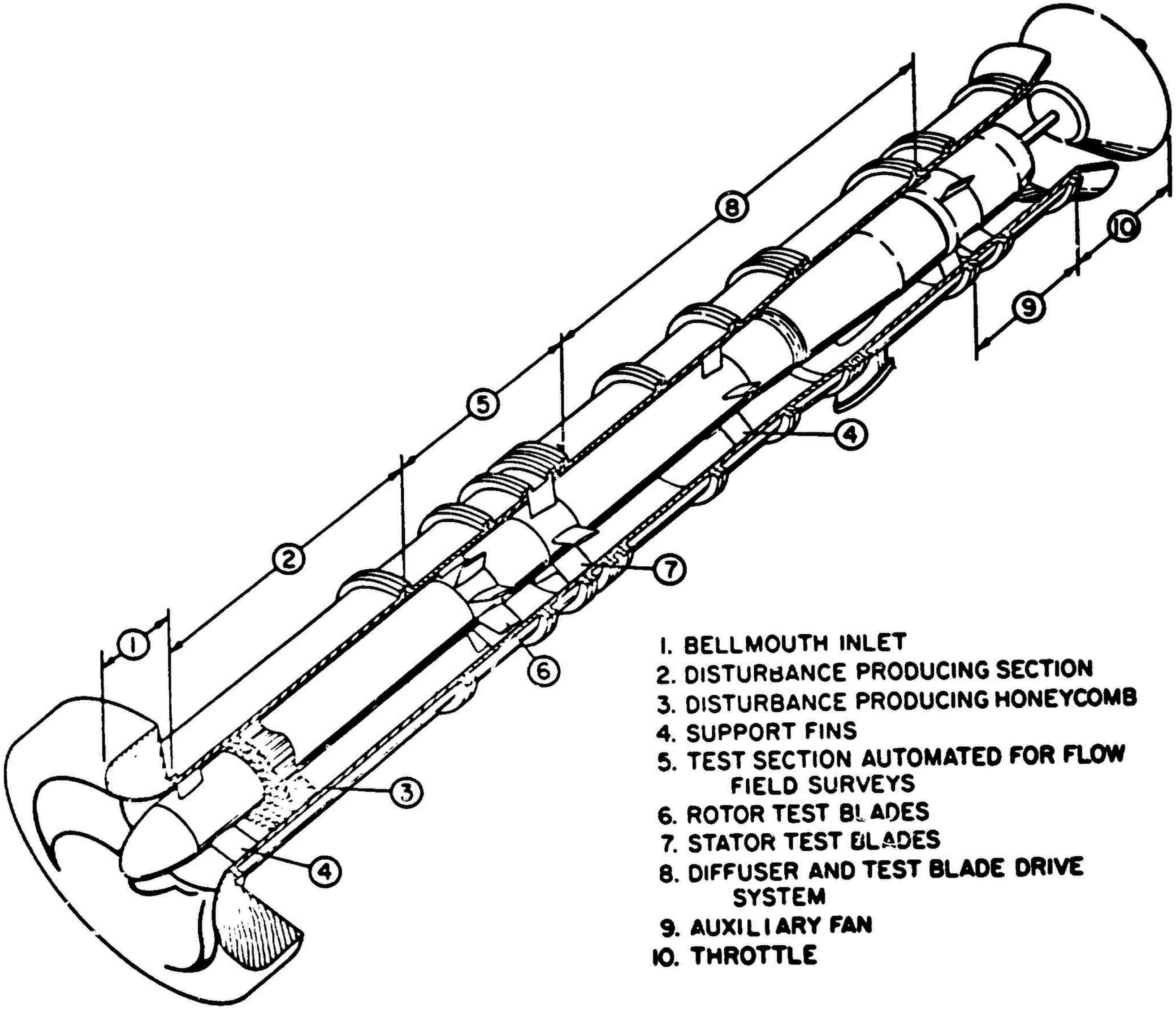

Figure 16. Schematic of Applied Research Laboratory's Axial Flow Research Fan.

motor which drives the test rotor and an auxiliary fan which is used to provide air through flow can be independently controlled by two adjustable frequency inverters. Rotor speeds up to 3600 RPM and axial velocities up to 111 feet/sec are possible. Thus, by fixing the rotor speed and axial through flow velocity, a specified flow coefficient and angle of incidence may be obtained. The adjustable exhaust throttle provides additional control of the through flow, which may become necessary particularly at low axial velocities. A probe may be installed through a section of the outer casing which extends up and downstream of the rotor and may be rotated circumferentially through 360°. The probe may also be traversed radially, and a probe nulling system achieves probe alignment with the flow direction. Using this automated probe positioning and nulling system, large quantities of flow data may be easily and rapidly obtained.

Since, for the present work, a uniform axial velocity was required, the disturbance producing grids and the test stator vanes were not used. Flow measurements were made with only the rotor hub (no blades) installed in order to determine baseline flow characteristics within the AFRF. The data obtained from this calibration procedure will be used subsequently in the evaluation and reduction of test data to correct for flow non-uniformities inherent in the test facility. A plot of the measured local velocity in the flow passage versus radial position is shown in Figure 17a. Total pressure and inlet angle profiles are presented in Figure 17b. These data were measured with the facility operating at a reference velocity (V_{REF}) of 30 fps. The reference

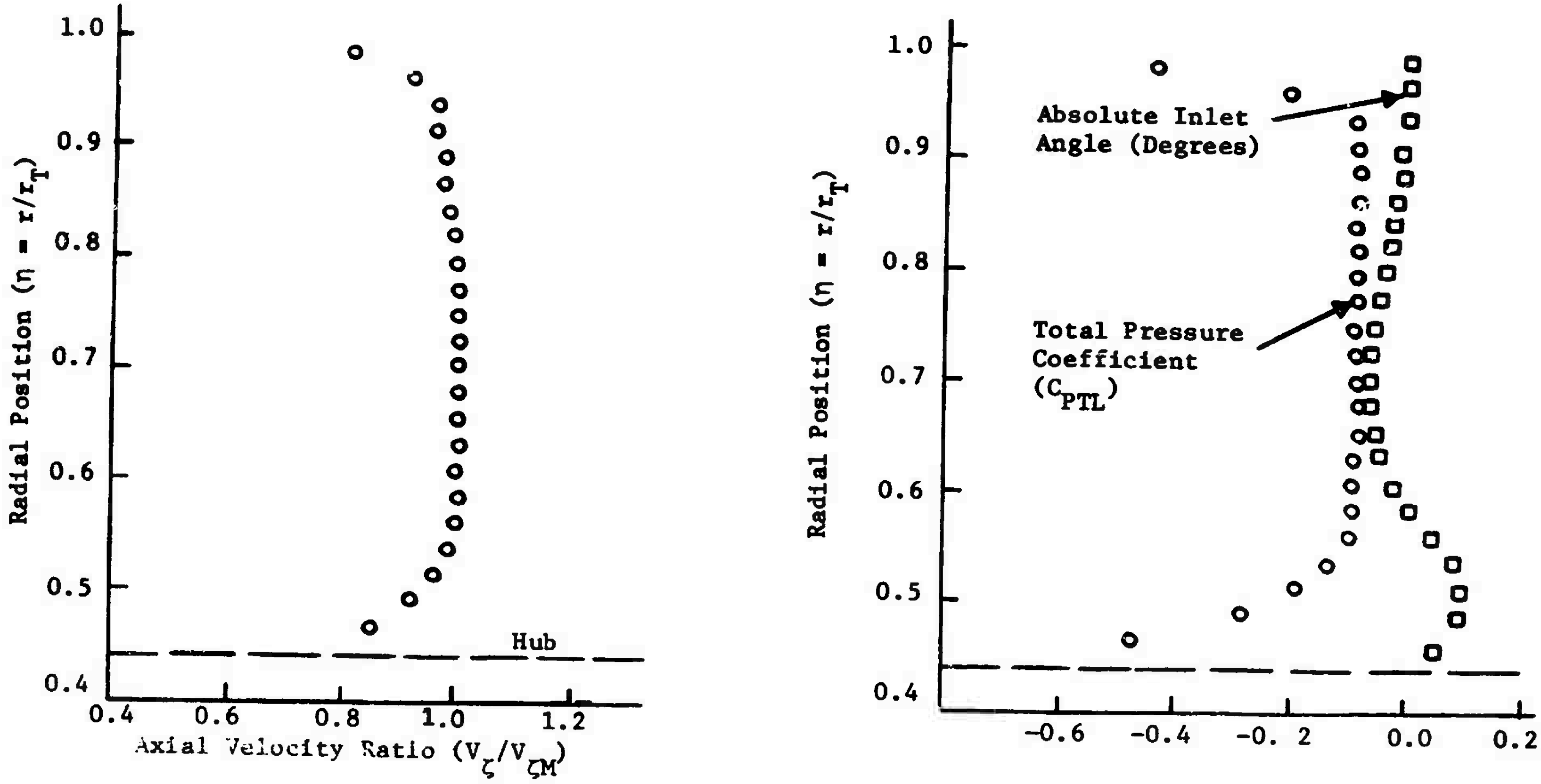

a. Axial Velocity Profile at the Rotor Inlet Plane ($\zeta = 0.0$)

b. Inlet Angle and Pressure Coefficient Profiles.

Figure 17. Axial Flow Research Fan Baseline Characteristics (Experimental).

velocity was measured with a pitot probe located midway between the hub and outer casing ($\eta = 0.701$) in a plane just forward of the rotor inlet plane.

3.1.2 Test Rotor. The constraints applied to the blade design were rather flexible. A high solidity, large stagger, low hub/tip ratio rotor with a few blades was desired since it was felt that these characteristics would induce a flow with significant three-dimensional effects. Further, the blades had to be approximately radial and meet the free vortex conditions due to the limitations of the three-dimensional theory. The implications of the contradictory requirements of the definition of free vortex in two- and three-dimensional theories were not fully understood at the time of design; hence, the blades were designed to the two-dimensional free vortex condition. Other design parameters were chosen either intuitively or for convenience.

The initial design was based on equations given by Morelli and Bowerman (1). This method was chosen because it was relatively simple and permitted rapid parametric studies of various possible configurations. The blade circulation was assumed to grow linearly in the axial direction from zero at the blade inlet to its full value at the blade outlet. As a result of this variation, the relative streamline through the blade passage was curved, and the effect of this curvature upon lift coefficient was considered. A correction to the lift coefficient due to the interference effects of blades in a cascade based on the work of Scholz (3) and Hawthorne (30) was also included. Based on the above consideration, the relative streamline coordinates through the rotor and other blade parameters (e.g., chord, lift coefficient, stagger angles, solidity, etc.) were determined. This preliminary design procedure led to a test rotor with three blades, a mid radius stagger angle of about 70°, an average solidity of 0.8, a hub/tip ratio of 0.442, and a circumferential extent of 90° for each blade. The blades were designed for a tip flow coefficient of 0.220. A NACA mean line 65 camber distribution and NACA 16-006 basic thickness form were used at all radii for the preliminary design. The camber line ordinates were scaled as necessary to produce lift coefficient at each radial location compatible with the free vortex condition. The thickness was scaled linearly from hub to tip. The profiles at five radial locations were designed, and these cylindrical blade profiles were stacked up about a straight radial line passing through the quarter chord point of the camber line of each profile. This is illustrated by the stack up of the hub, mid radius, and tip profiles in Figure 18, which also shows the angle each profile makes with the axis of rotation (ζ) of the rotor.

Figure 19 is a view of a rotor blade as seen looking downstream along the rotor axis. The radial line on which the quarter chord point of each profile has been stacked up and the angular location of the leading edge of the blade from this line at the tip, mid radius, and hub are shown. The blade board sections are shown crosshatched and are useful for checking the blade surface resulting from the proposed stack up for irregularities and for a smooth blade contour from hub to tip. The board sections are cross sections of the blade formed by the intersection of the blade with several radial planes, and are shown rotated into the plane of the rotor blade. These board sections are obtained graphically by a projection of the blade profile stack up as developed by Wislicenus (31). Some deviation from the initially proposed

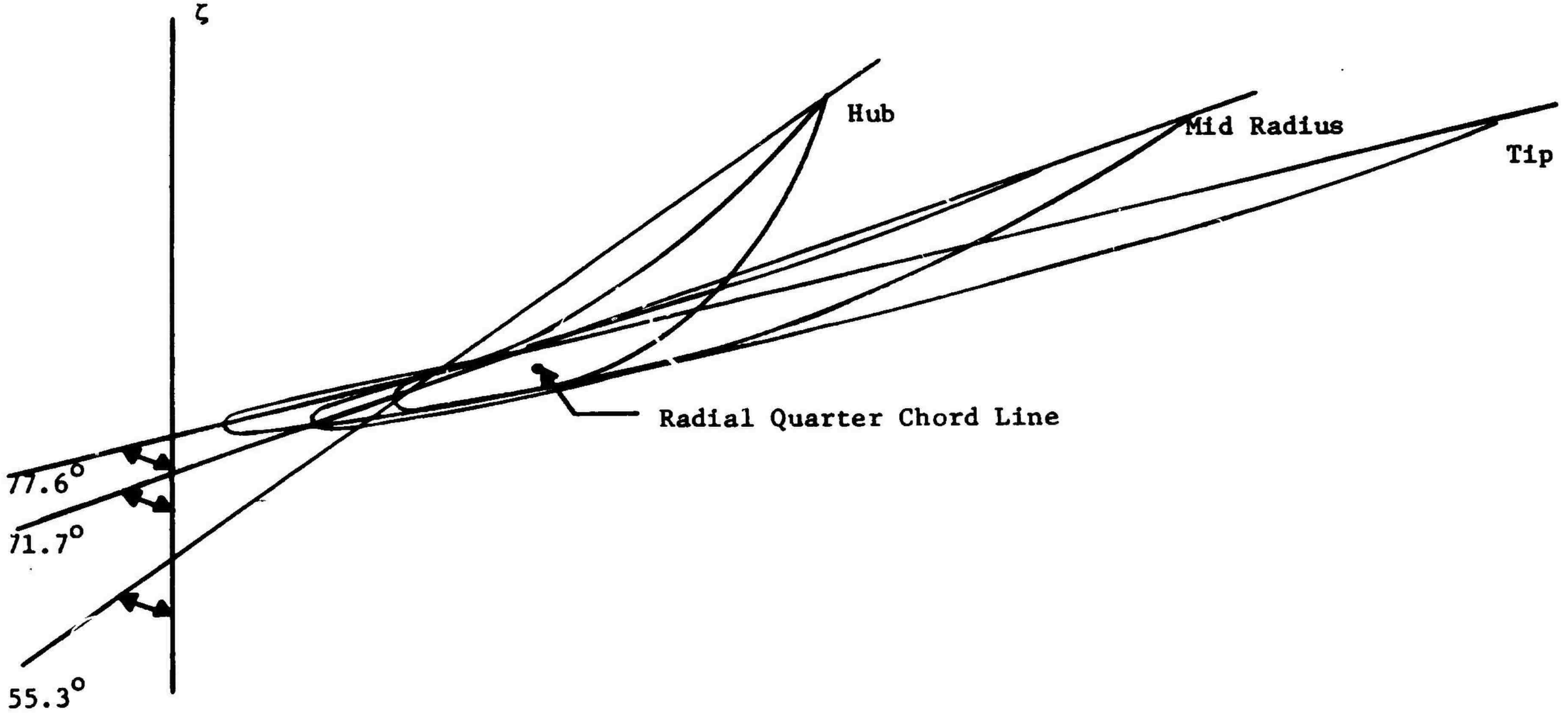

Figure 18. Blade Profile Stack Up.

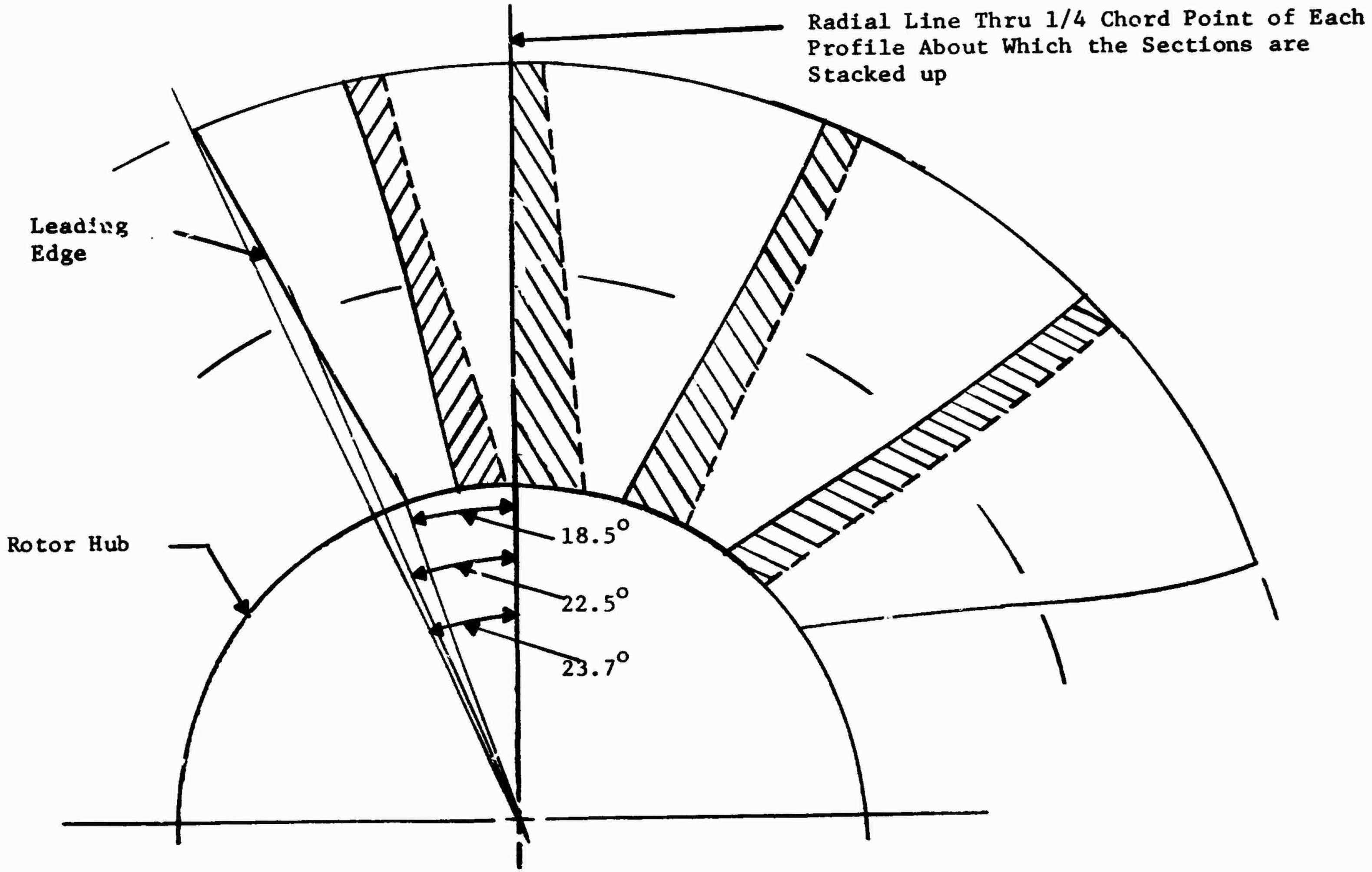

Figure 19. Test Rotor Blade Board Sections.

geometry was made necessary due to fabrication and structural reasons. The large chord, stagger, and twist presented some difficulty. In order to accommodate the travel limitations of the cutting tool on the numerical milling machine, the blades were manufactured in five sections and the final profiles were modified from the standard NACA sections initially chosen. These modified blade profiles were then analyzed using the Douglas Neumann cascade program, and the final blade characteristics are shown in Table 3.

The blades were cut from seasoned mahogany wood. One blade pressure surface and one suction surface were instrumented for measuring the blade surface static pressure distribution. Ten hypodermic tubes of 0.065 in. diameter were imbedded in each surface. A static pressure orifice of 0.040 in. diameter was drilled at five radial locations (η = 0.511, 0.581, 0.721, 0.861, 0.981) in each tube (Figure 20). Each pressure tube was then connected with the instrumentation package. By placing tape over the static pressure orifices at any four of the radial locations, the pressures were measured along the remaining radial position.

Initially, the blades were mounted radially (Figures 21 and 22a). That is, they were mounted on the hub such that the straight quarter chord line was coincident with a radial line extending from the rotor axis through the quarter chord point of the hub profile to outer casing. Subsequently, tests were conducted with the blades mounted such that a reference dihedral angle (μ), measured in a plane perpendicular to the chord line of the hub profile, existed between the quarter chord line and the same radial line defined above for the radial mounting (Figure 22b). The dihedral angle is defined as positive when the blade leans

Table 3

BLADE CHARACTERISTICS FOR THE EXPERIMENTAL ROTOR

Radial Location (η)	Radius (in)	Stagger Angle (deg)	Chord Length (cm)	S/C	Camber (% of Chord)	Max. Thickness (% of Chord)
1.000(tip)	10.75	77.6	41.5	1.38	1.2	2.3
0.861	9.25	75.3	35.6	1.38	1.8	3.35
0.721	7.25	71.7	30.5	1.34	2.7	4.7
0.581	6.25	65.8	25.3	1.31	4.4	6.6
0.442(hub)	4.75	55.3	19.8	1.31	8.4	9.62

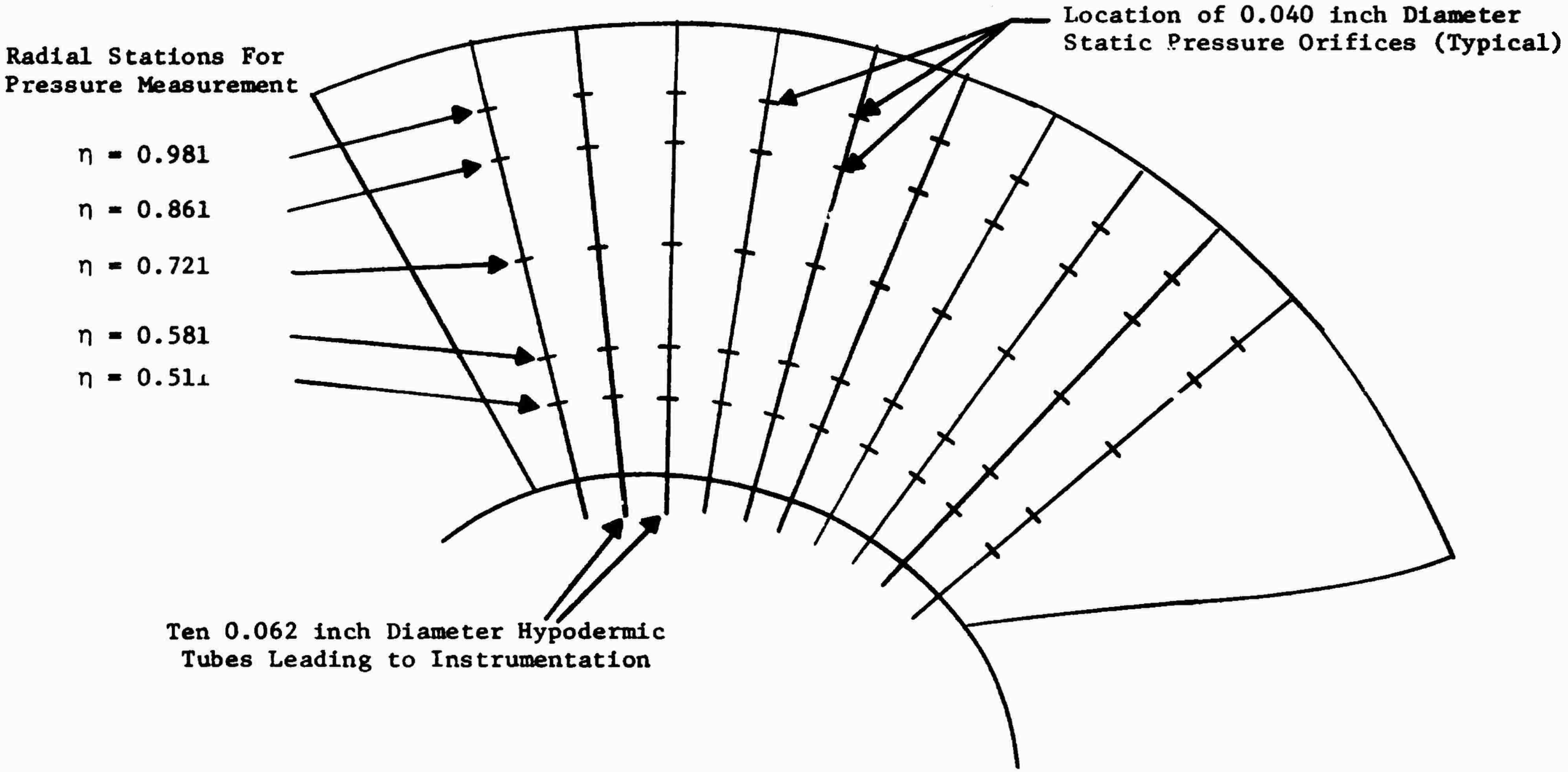

Figure 20. Schematic of Blade Static Pressure Orifice Locations.

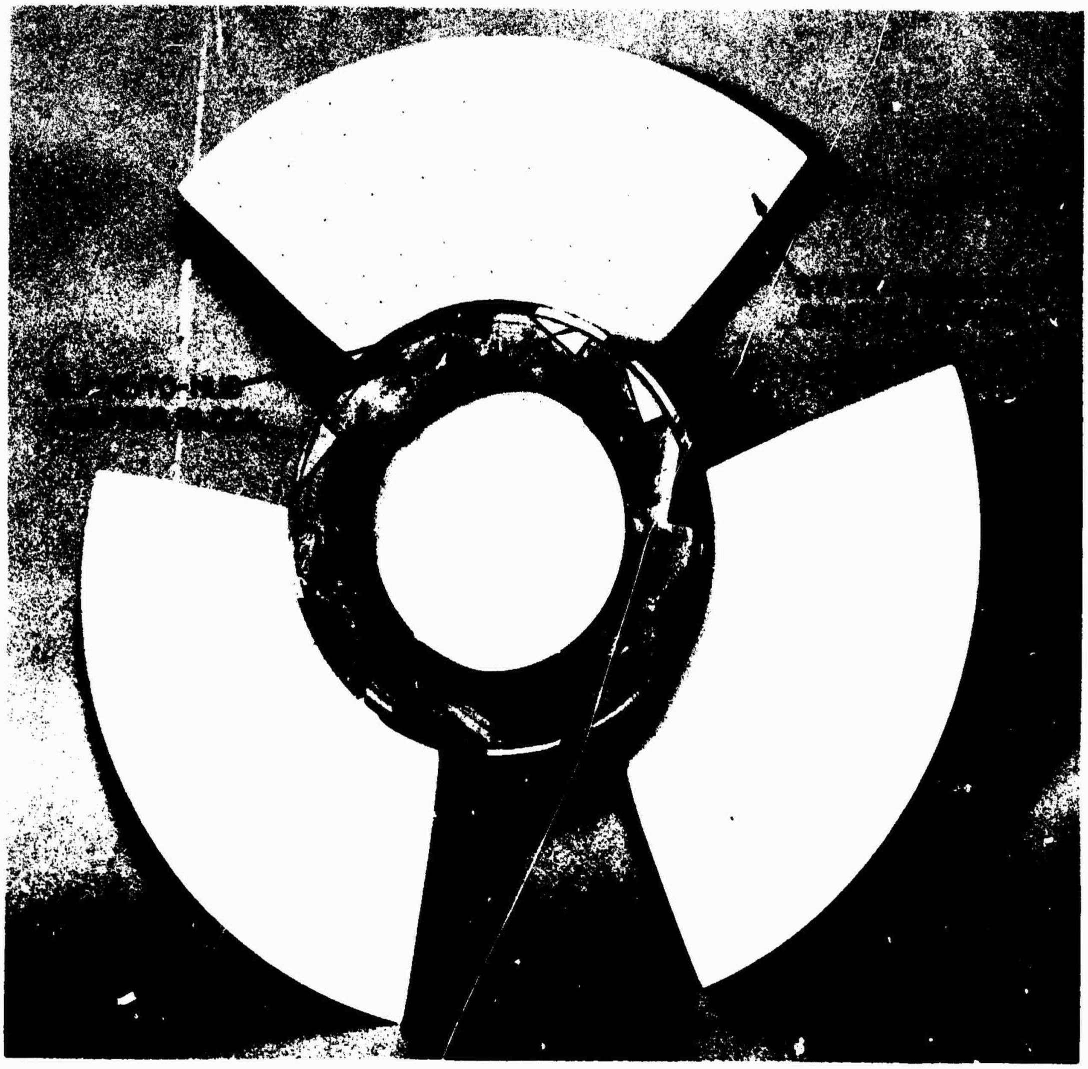

Figure 21a. Test Rotor with Blades Mounted Radially - Front View Showing Static Pressure Orifices on Suction Surface.

Figure 21b. Test Rotor with Blades Mounted Radially - Side View.

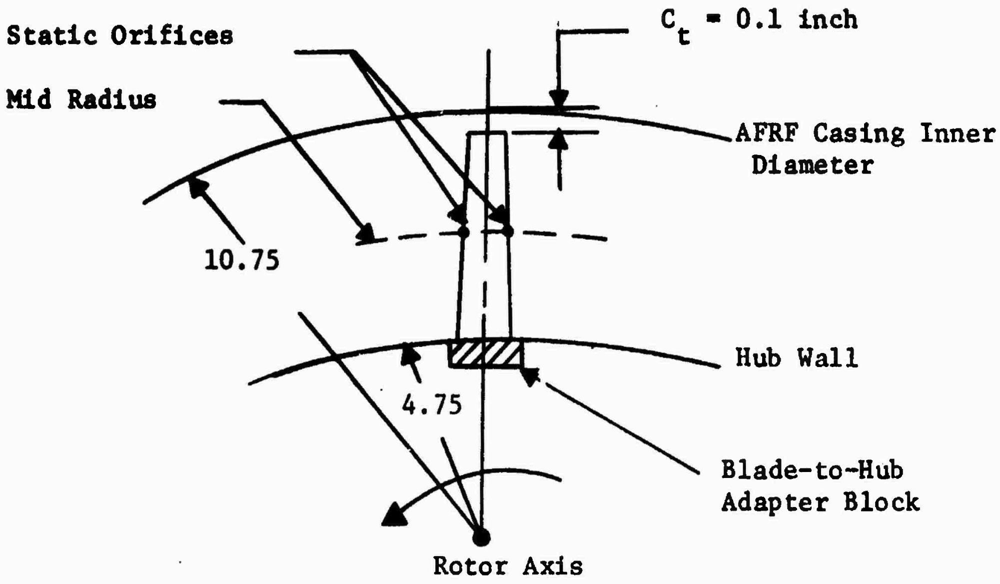

a. Radial Blade Mounting

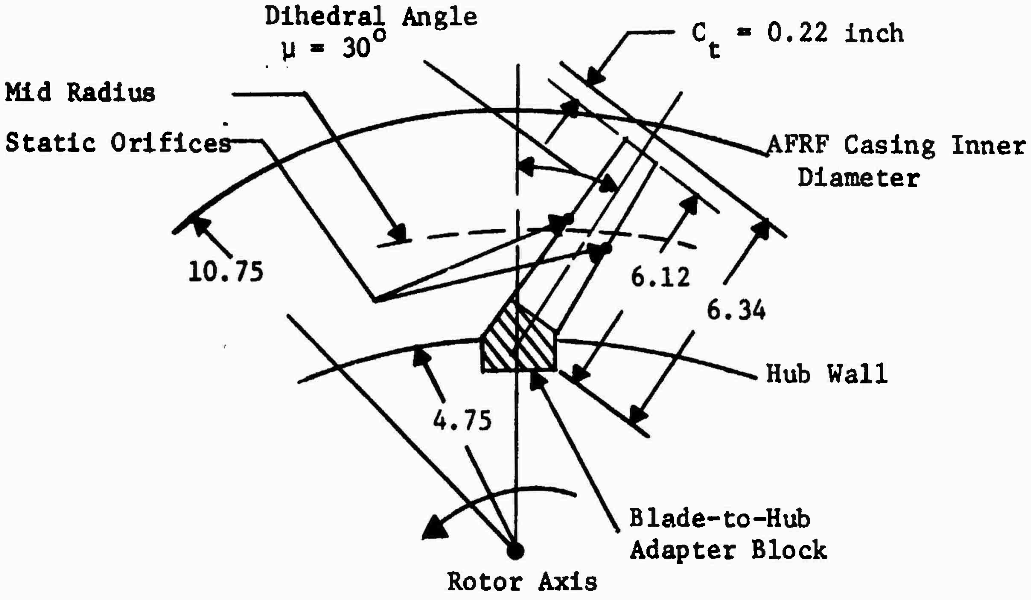

b. Dihedral Blade Mounting

Figure 22. Effect of Dihedral Mounting on Test Rotor Blade Tip Clearance and Relative Static Pressure Orifice Location.

toward its suction surface and negative when it leans toward its pressure surface. This convention was adopted to be consistent with the definition of dihedral used in aircraft wing theory. Three sets of blade-to-hub adapter blocks which fit into slots in the hub and fasten to the blade root provided reference dihedral angles of 0°, -15°, and -30°.

The rotor was operated in a uniform axial absolute inlet flow, and the configurations tested are summarized in Table 4. The velocity profiles and the flow angles at rotor inlet and exit, and the steady-state blade static pressures were measured for each of these tests. The experimentally measured blade static pressures were compared with pressure distributions predicted by both two- and three-dimensional theories.

3.1.3 Instrumentation for Measuring the Steady-State Static Pressures on a Rotating Blade. An instrumentation package for measuring the steady-state static pressures on a rotating blade and transmitting the output signal to the stationary laboratory frame was designed and built. The primary elements of this package, which attaches to the rotor and rotates with the blade system, are a pressure transducer and a switching unit (i.e., scanivalve). A potentiometer is also used to monitor the position of the switching unit. The output signal is passed through the rotor hub and shafting to a slip ring unit. The instrumentation package is shown in Figure 23.

Utilizing a pressure transducer mounted in the rotating rotor-fixed frame of reference simplifies the measurement of the static pressures on the surface of a rotating blade. Since the transducer converts the mechanical pressure signal into an electrical signal within the rotating

Table 4

ROTOR CONFIGURATIONS TESTED IN THE EXPERIMENTAL PROGRAM

Axial Velocity (ft/sec)	Rotor RPM	Flow Coefficient ($V_x/\omega r_T$)	Skew Angle (degrees)	Quantities Measured (Blade C_p)	(Flow Angles)
12.2	1000	0.130	0 radial	x	x
20.8	1000	0.220	0	x	x
32.0	1000	0.340	0		x
12.2	1000	0.130	-15	x	x
20.8	1000	0.220	-15	x	x
6.6	1000	0.071	-30		x
12.2	1000	0.130	-30	x	x
20.8	1000	0.220	-30	x	x

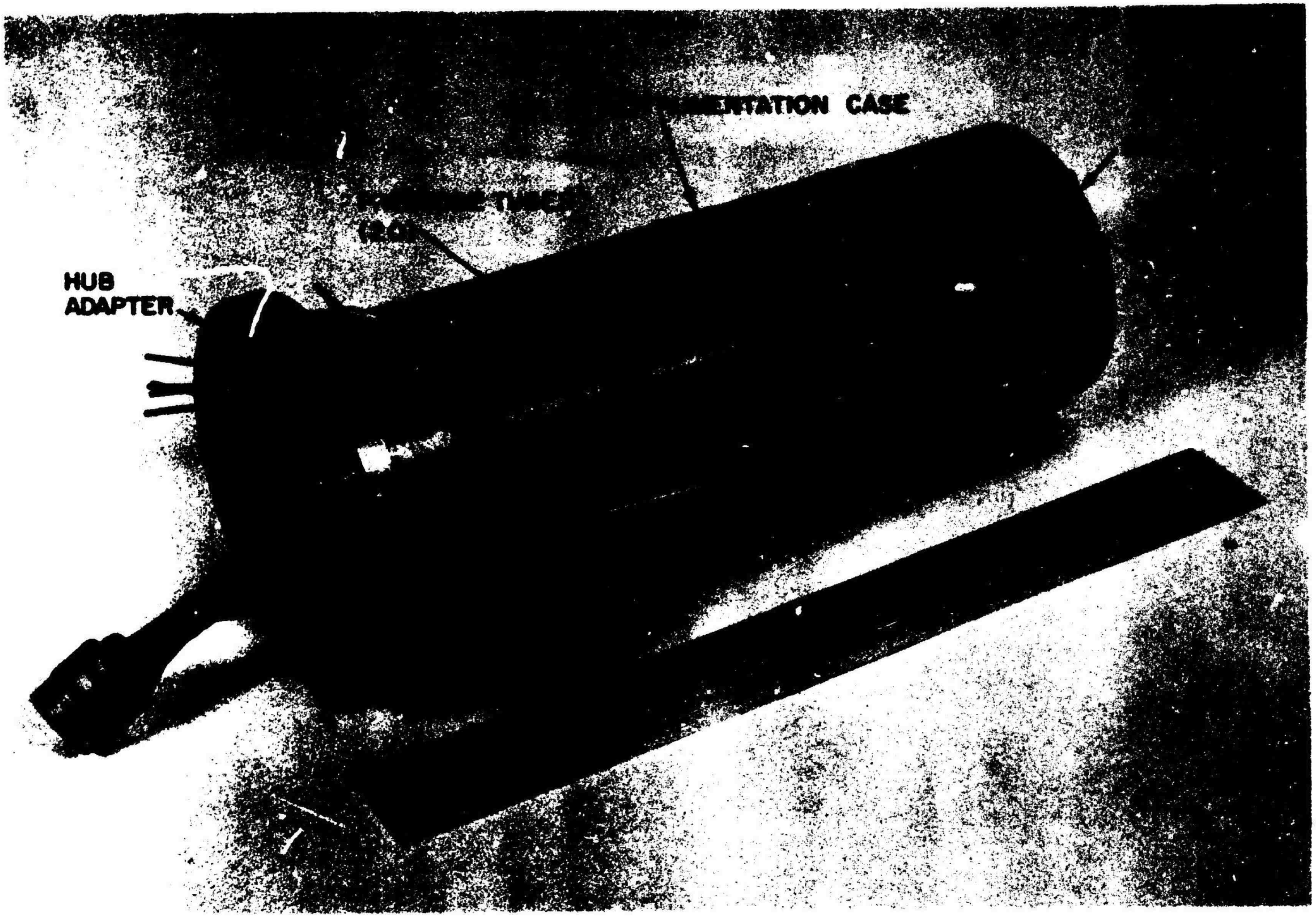

Figure 23a. Instrumentation Package - Assembled.

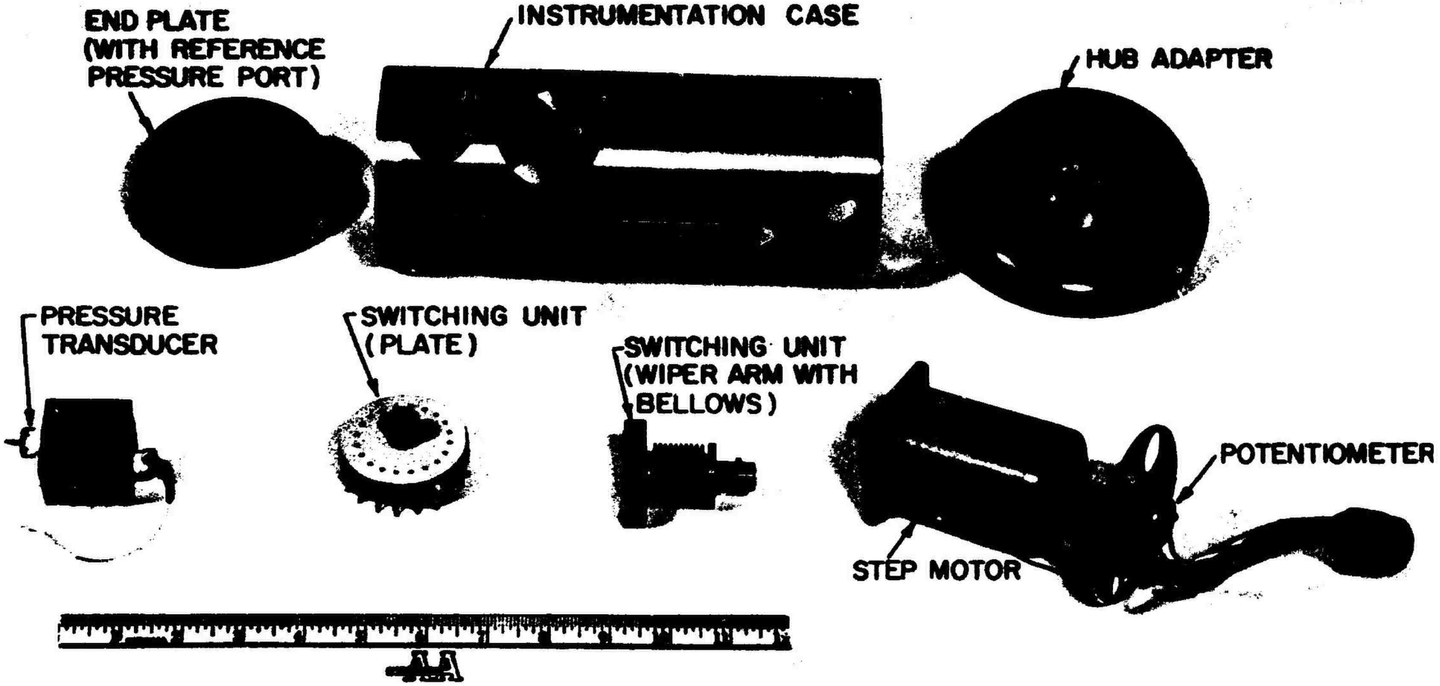

Figure 23b. Instrumentation Package - Components.

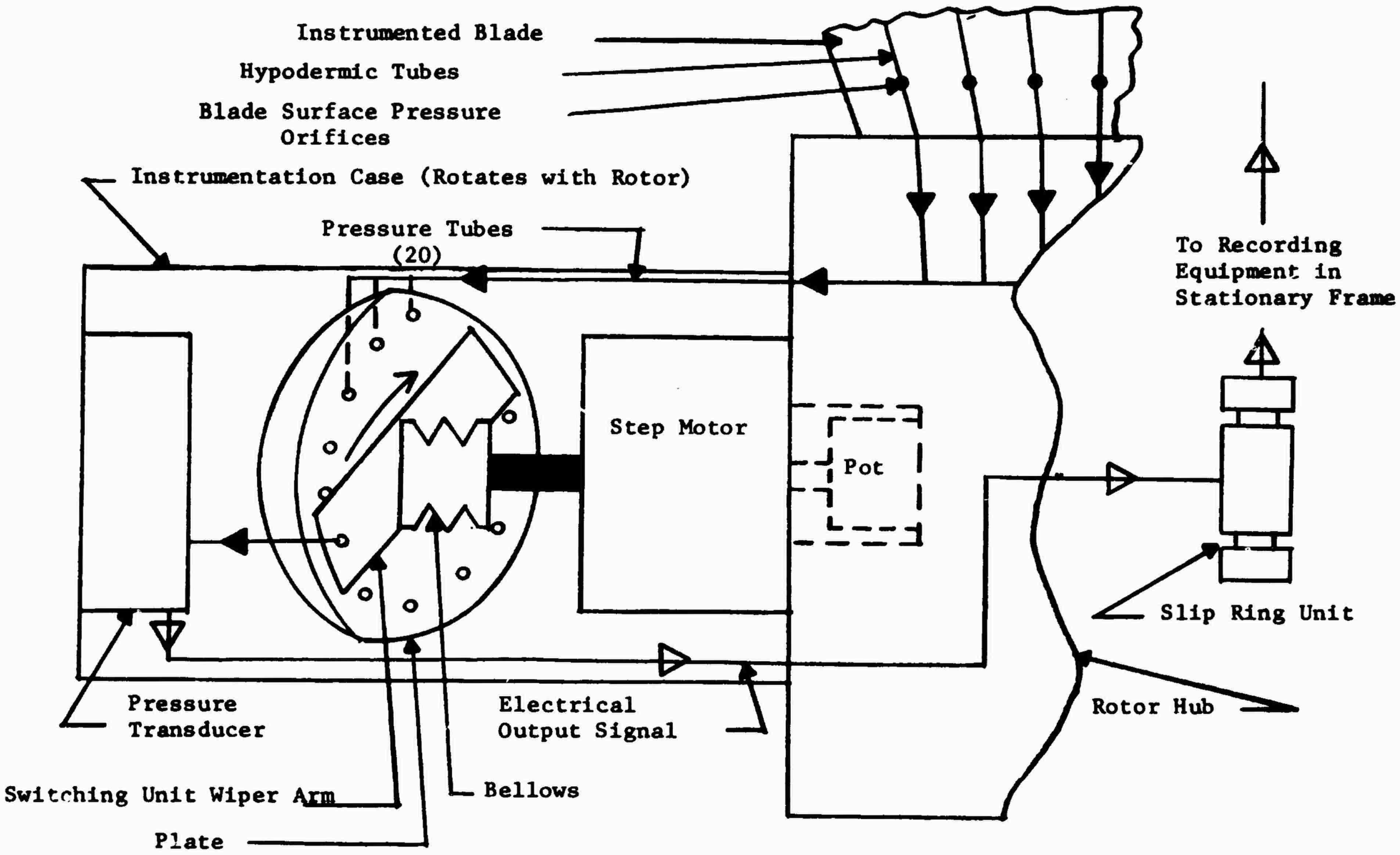

Figure 23c. Instrumentation Package-Schematic.

frame, the passage of this output signal to the stationary laboratory-fixed frame requires only a slip ring unit. Furthermore, the switching unit in the rotating system allows the use of the same output channel for the measurement of the blade pressures at several stations. A multi-channel, sealed-bearing, pressure transfer device would otherwise be required to extract the mechanical pressure signals from the rotating frame.

The instrumentation package attaches to the face of the rotor hub (No. 6 in Figure 16) and operates inside the cylindrical hub of the disturbance producing section (No. 2 in Figure 16). Thus, the entire package rotates with the blade system. Hypodermic tubes which lead from the static pressure orifices on the blade surface connect to the stationary part, or the plate, of the 20 channel switching unit. The spacing between channels is 18 degrees. The movable part of the switching unit, or the wiper arm, is controlled by a SLO-SYN HS-25E precision stepping motor. A copper bellows with adjustable compression is located between the motor shaft and wiper arm, and holds the arm firmly against the plate. Rubber O-rings in the wiper arm and the teflon-coated face of the plate form a pressure seal. The wiper arm may be positioned over any hole in the plate by stepping the motor, and then the pressure of the corresponding static orifice may be read. The pressure signal is passed to the pressure transducer. A Validyne model DP 15 differential transducer, range ± 0.5 PSID, was used. The inlet for the reference port of the transducer is located inside the hub along the axis of rotation. This eliminates the dynamic interference which would occur if the port was exposed to the relative velocity due to the rotation.

A slip ring unit, which is not an integral part of the instrumentation package, allows passage of the electrical signal to the recording equipment located in the stationary laboratory-fixed frame.

The other shaft of the double shafted HS-25E motor is connected to a Helipot model MN54 potentiometer. The potentiometer is used to check for accurate stepping of the motor and to indicate the channel on which the wiper arm is positioned.

Since the use of a pressure transducer mounted in the rotating system was a new technique, some questions about the effect of centrifugal force on the transducer existed. Although rotation about an axis perpendicular to the plane of the transducer diaphragm theoretically would eliminate any centrifugal effects, it was not clear initially that the effects of rotation on the transducer output could actually be neglected. There could have been, for example, a pressure difference erroneously indicated due to deflection of the diaphragm by centrifugal forces. Thus, it was necessary to investigate the output of a rotating transducer and to develop calibration curves, if required. A test jig was built to spin the transducer over a range of speeds (0 to 3750 RPM) and eccentricities (0 to 0.5 in.). Eccentricity is the distance between the axis of rotation and the center of the transducer diaphragm. The results of this test indicated that if the transducer is located on the axis of rotation and perpendicular to it and if the static port is properly shielded, the rotation has no significant effect on the output signal. For all speeds and eccentricities tested, the deviation between the stationary and rotating output signal from the transducer was less than 7.11×10^{-3} in. of H_2O (2.56×10^{-4} psi). Hence, the effect of rotation on the transducer, as used with this instrumentation, is negligible and no calibration was required.

Check-out of the system indicated that experimentally measured pressure coefficient data agreed with cascade predictions within 5% at the mid radius of a radially mounted blade. Further discussion of the instrumentation is presented by Howells and Lakshminarayana (32).

3.2 Results of Flow Measurements on Rotating Blades

The rotor was operated at 1000 rpm with air as the test medium and with inlet velocities of 3.7, 6.34 and 9.75 m/sec (corresponding to values of $\phi = 0.13$, 0.22 and 0.34 respectively). The radial bladed rotor was tested at all these flow coefficients, and the dihedral bladed ($\mu = -15^\circ$ and -30°) rotor was tested at $\phi = 0.13$ and 0.22. The axial velocity profile and the incidences were kept identical for the rotors with $\mu = 0$, -15°, and -30°. The exit flow measurements were made at a distance of one axial extent of the rotor (about 12 cm) downstream. A commercially available YC type probe was installed through the outer casing of the fan facility such that it could be rotated circumferentially and traversed radially. Also, an automatic probe nulling system was used to achieve probe alignment with the flow direction. Exit flow velocities and absolute exit flow angles were measured at about 23 radial positions.

3.2.1 Radial Blade Configuration . The measured and predicted values of flow angles and blade static pressure distributions at various radii for the design flow coefficient ($\phi = 0.22$) and one off-design condition ($\phi = 0.13$) for the radial blade configuration ($\mu = 0^\circ$) are shown in Figures 24 through 34. The blade outlet angles have been

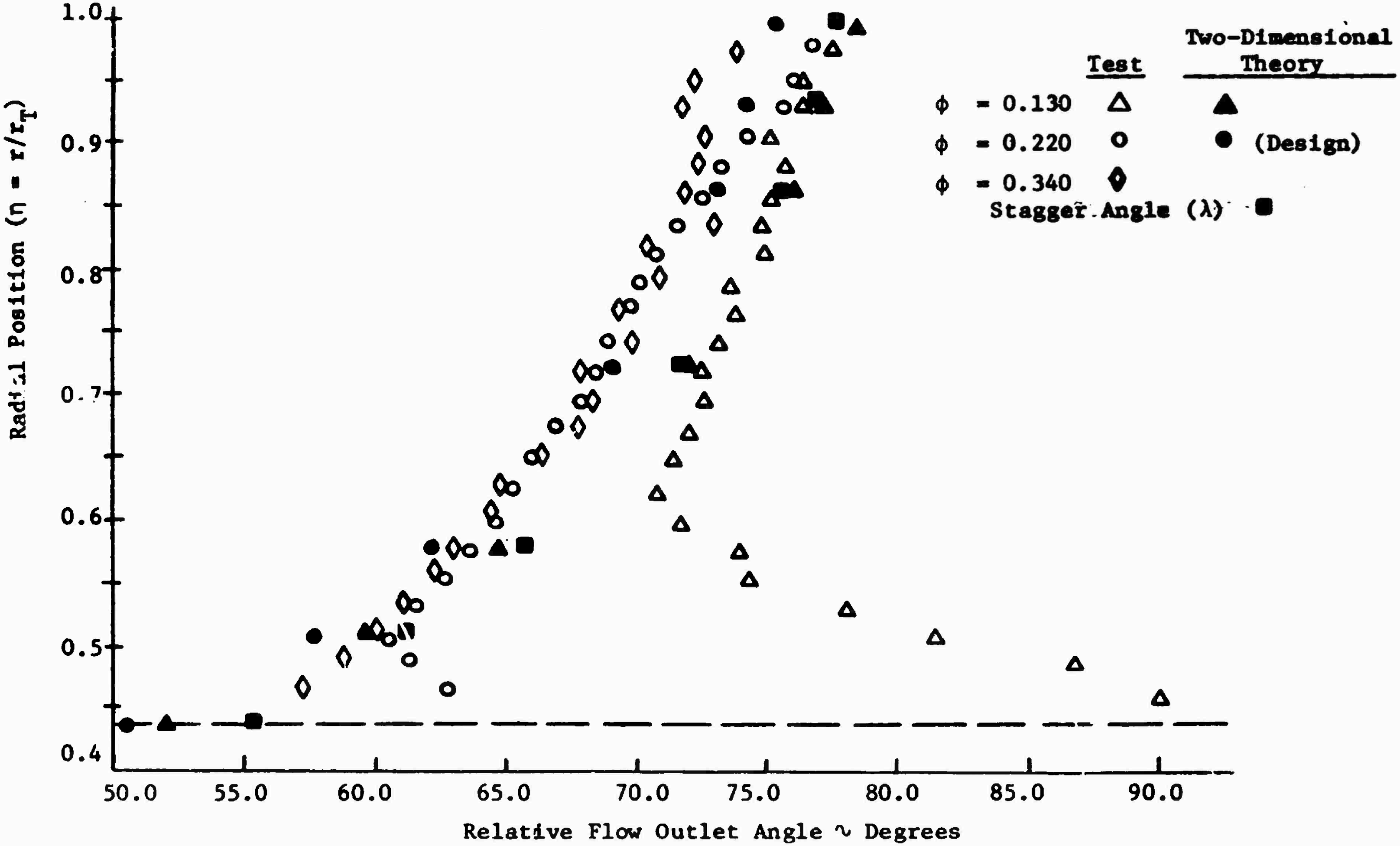

Figure 24. Flow Outlet Angle Summary for Radial Blades ($\mu = 0^o$).

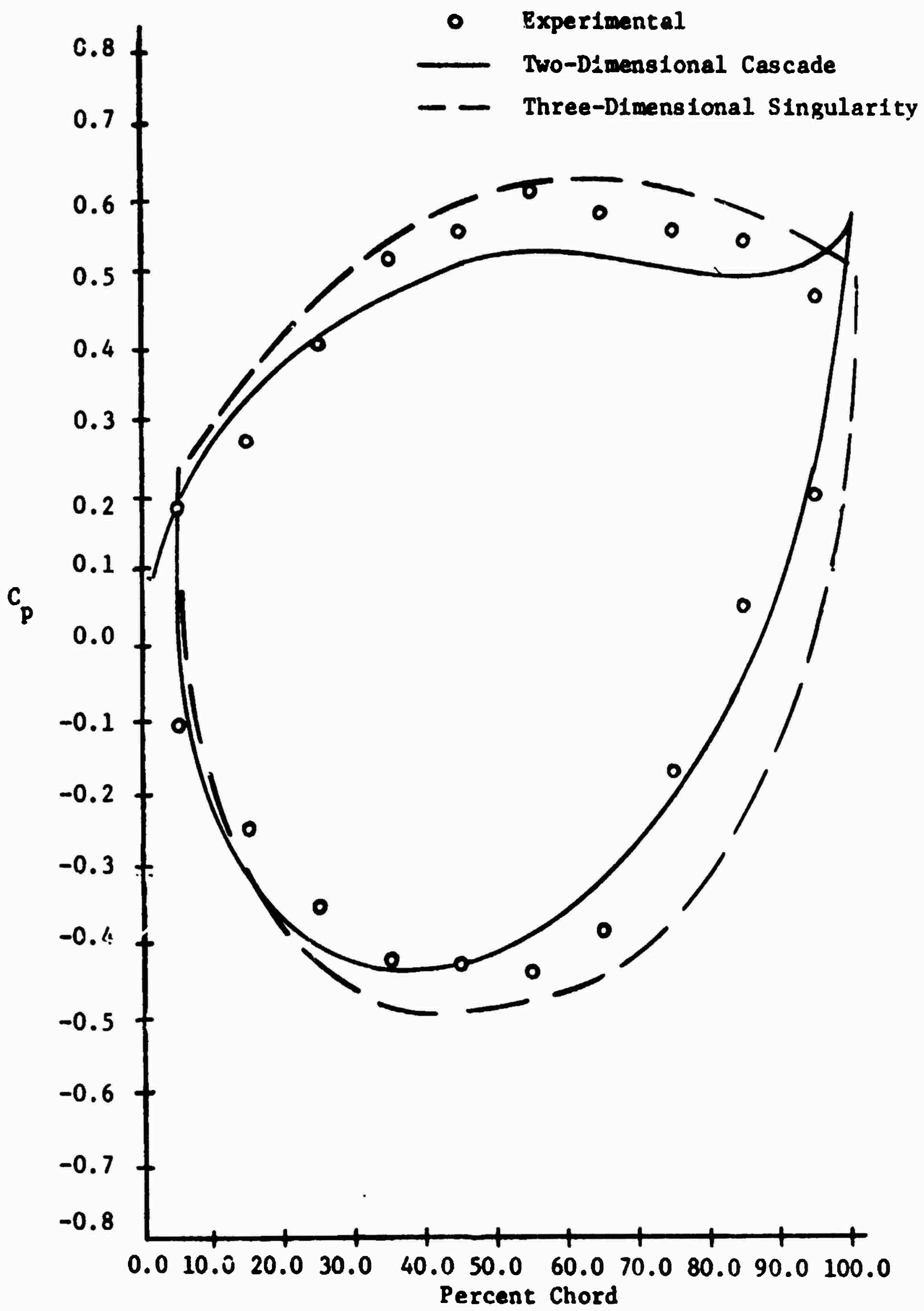

Figure 25. Experimental and Theoretical Static Pressure Coefficient Distributions for Test Rotor; Radial Blades ($\mu = 0^{o}$), $\eta = 0.511$ (Hub), $\phi = 0.220$.

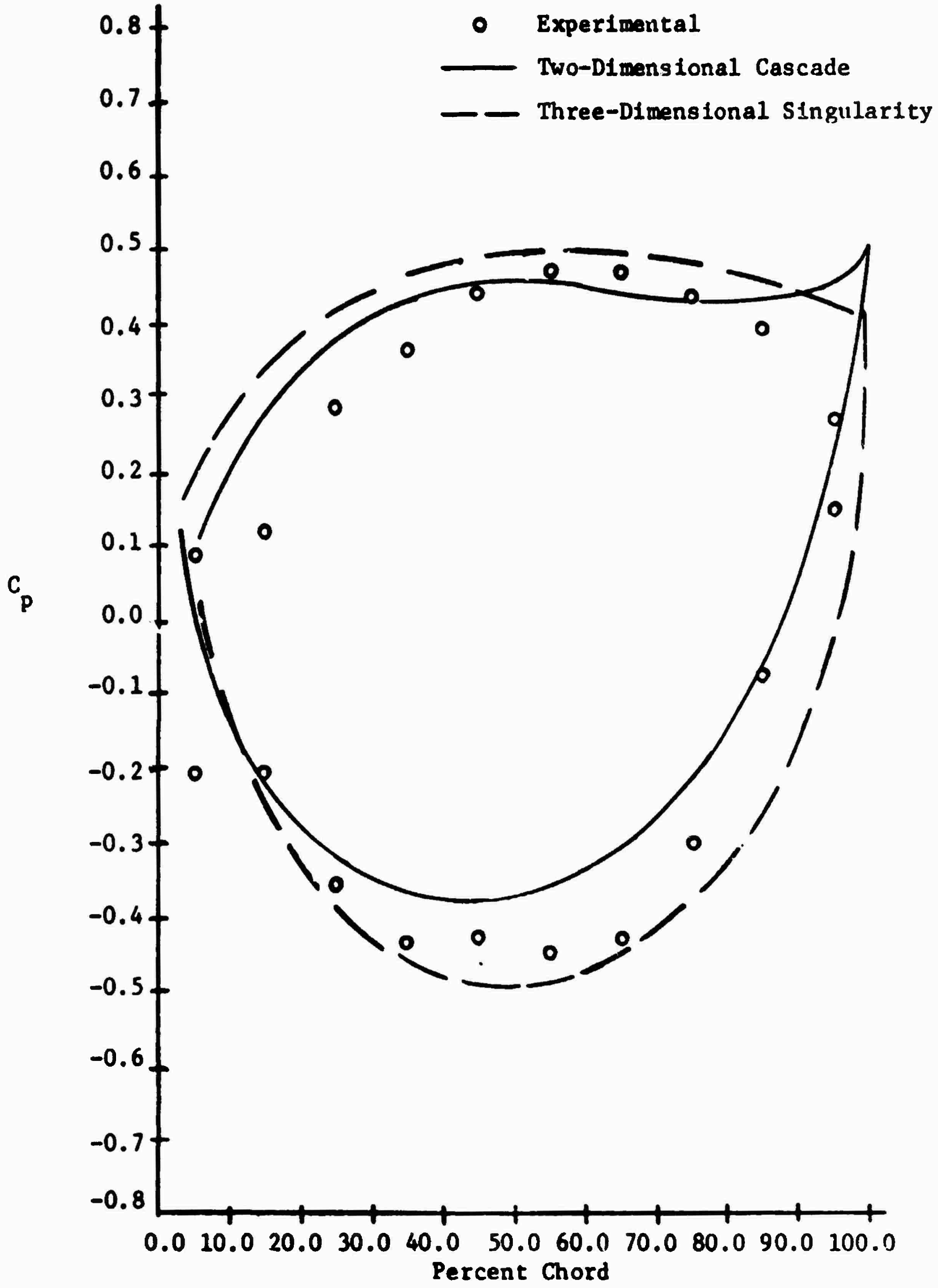

Figure 26. Experimental and Theoretical Static Pressure Coefficient Distributions for Test Rotor; Radial Blades ($\mu = 0^o$), $\eta = 0.581$ (1/4 Radius), $\phi = 0.220$.

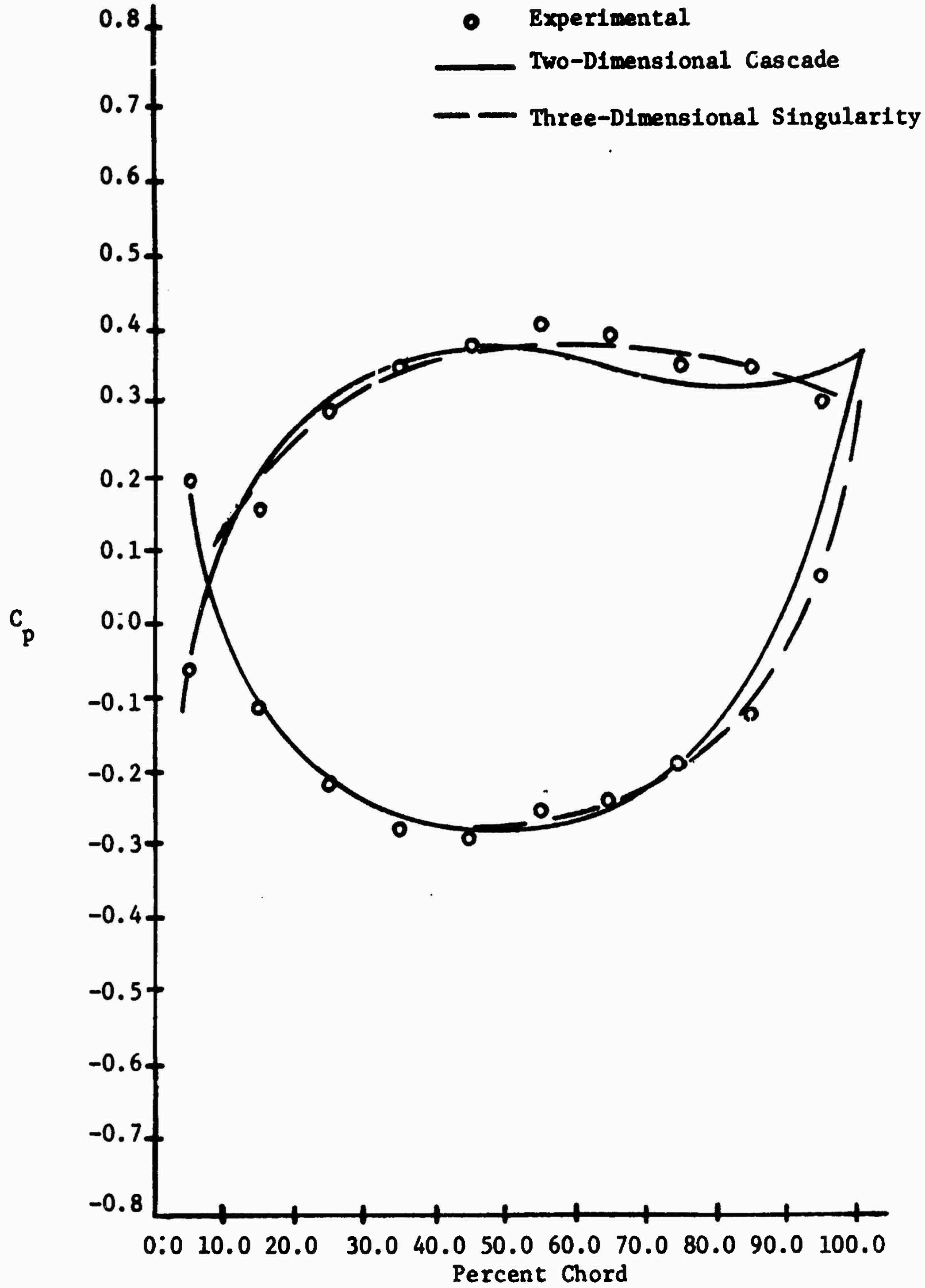

Figure 27. Experimental and Theoretical Static Pressure Coefficient Distributions for Test Rotor; Radial Blades ($\mu = 0^{\circ}$), $\eta = 0.721$ (Mid), $\phi = 0.220$.

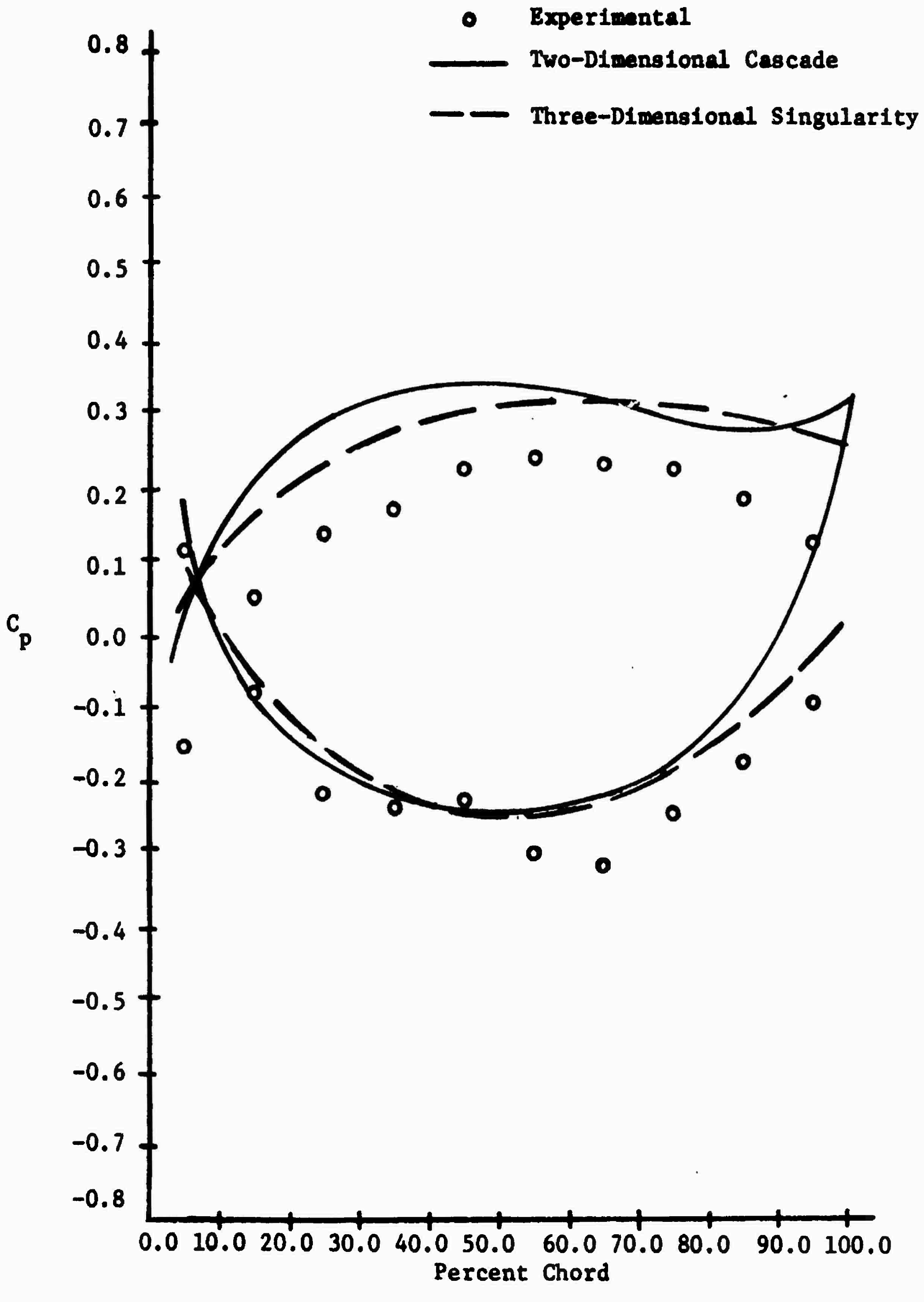

Figure 28. Experimental and Theoretical Static Pressure Coefficient Distributions for Test Rotor; Radial Blades ($\mu = 0^{\circ}$), $\eta = 0.861$ (3/4 Radius) $\phi = 0.220$.

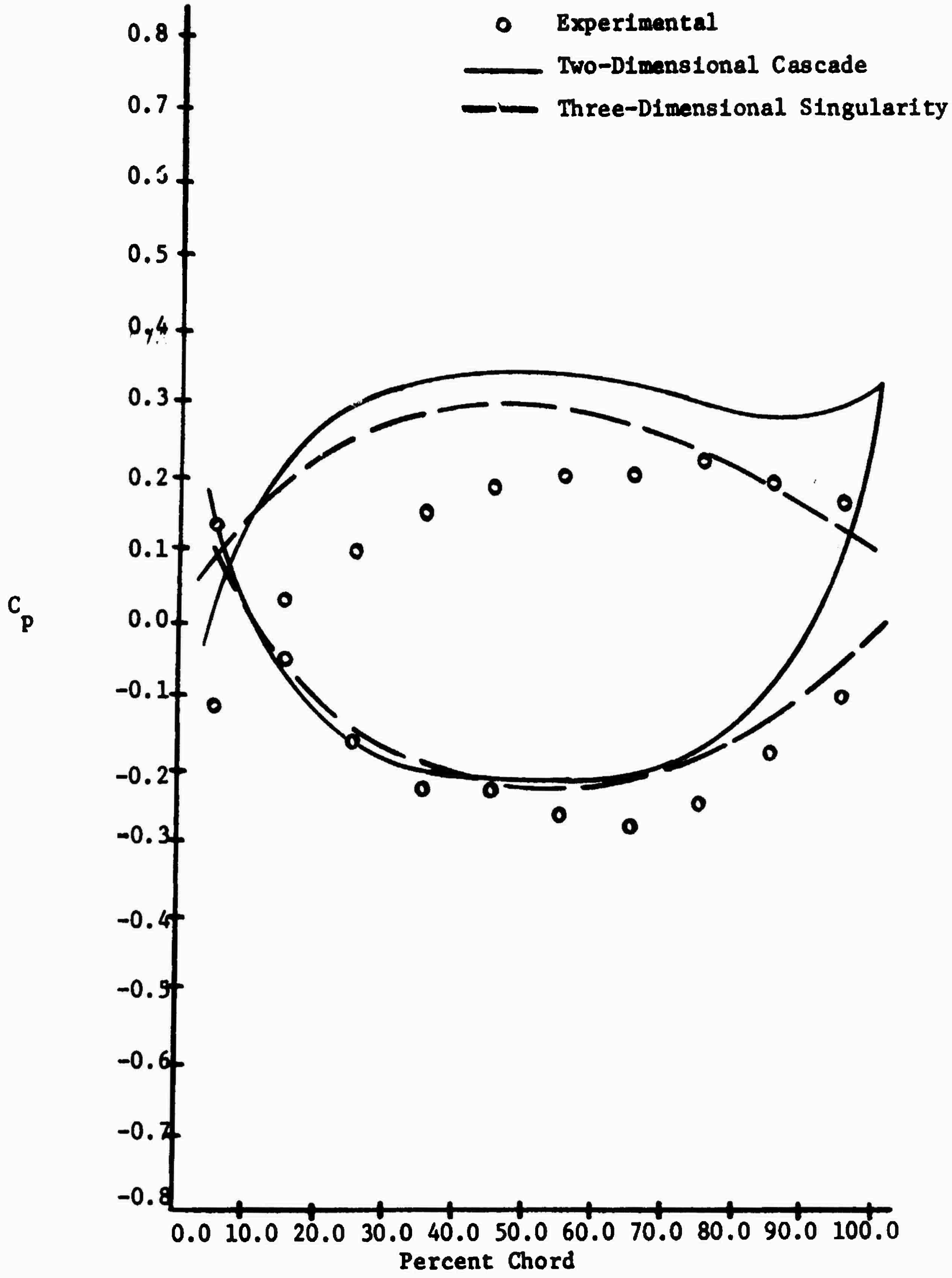

Figure 29. Experimental and Theoretical Static Pressure Coefficient Distributions for Test Rotor; Radial Blades $(\mu = 0^{\circ})$, $\eta = 0.981$ (Tip), $\phi = 0.220$.

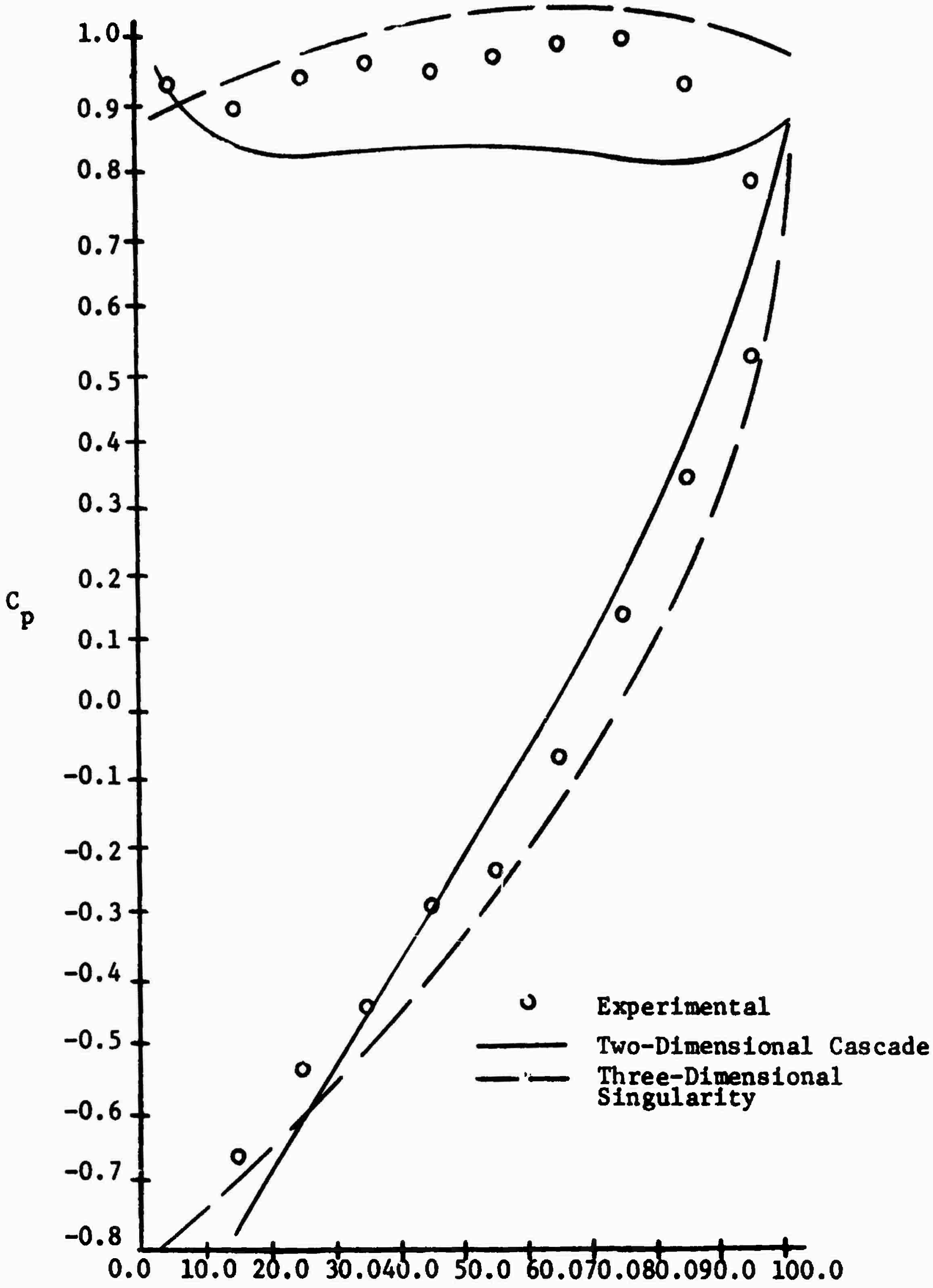

Figure 30. Experimental and Theoretical Static Pressure Coefficient Distributions for Test Rotor; Radial Blades ($\mu = 0^{\circ}$), $\eta = 0.511$ (Hub), $\phi_T = 0.130$.

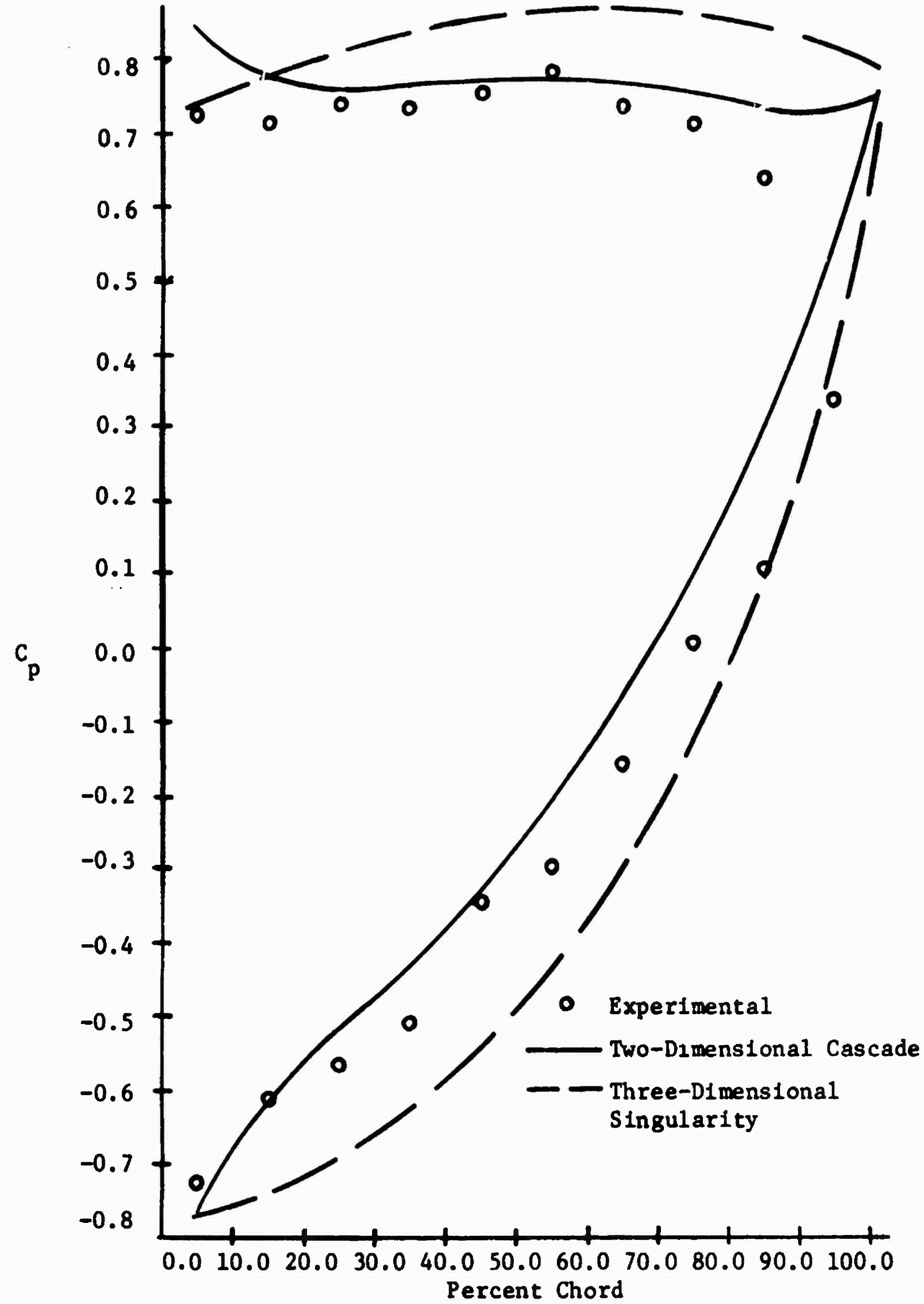

Figure 31. Experimental and Theoretical Static Pressure Coefficient Distributions for Test Rotor; Radial Blades ($\mu = 0^{o}$), $\eta = 0.581$ (1/4 Radius), $\phi = 0.130$.

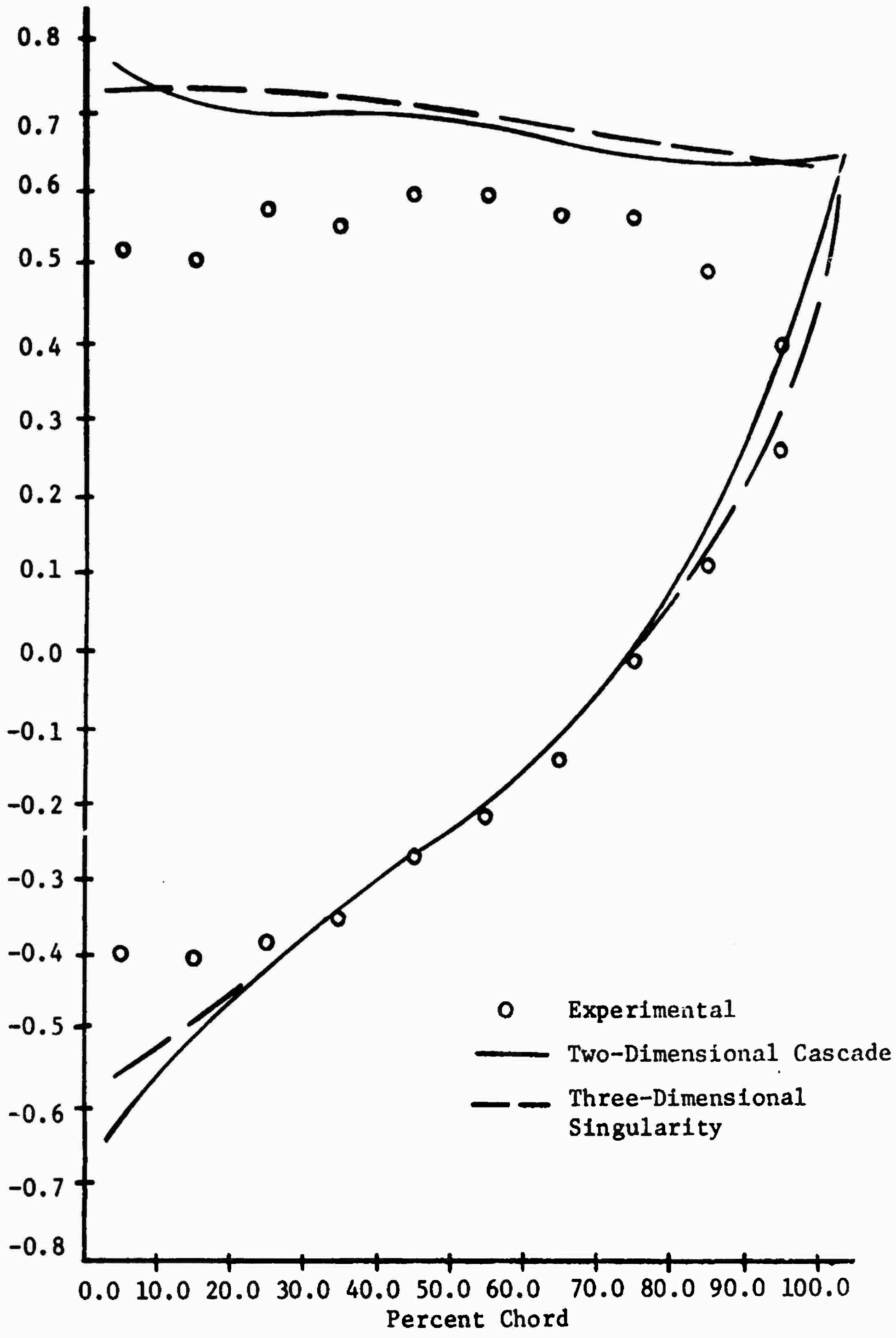

Figure 32. Experimental and Theoretical Static Pressure Coefficient Distributions for Test Rotor; Radial Blades ($\mu = 0^\circ$), $\eta = 0.721$ (Mid), $\phi = 0.130$.

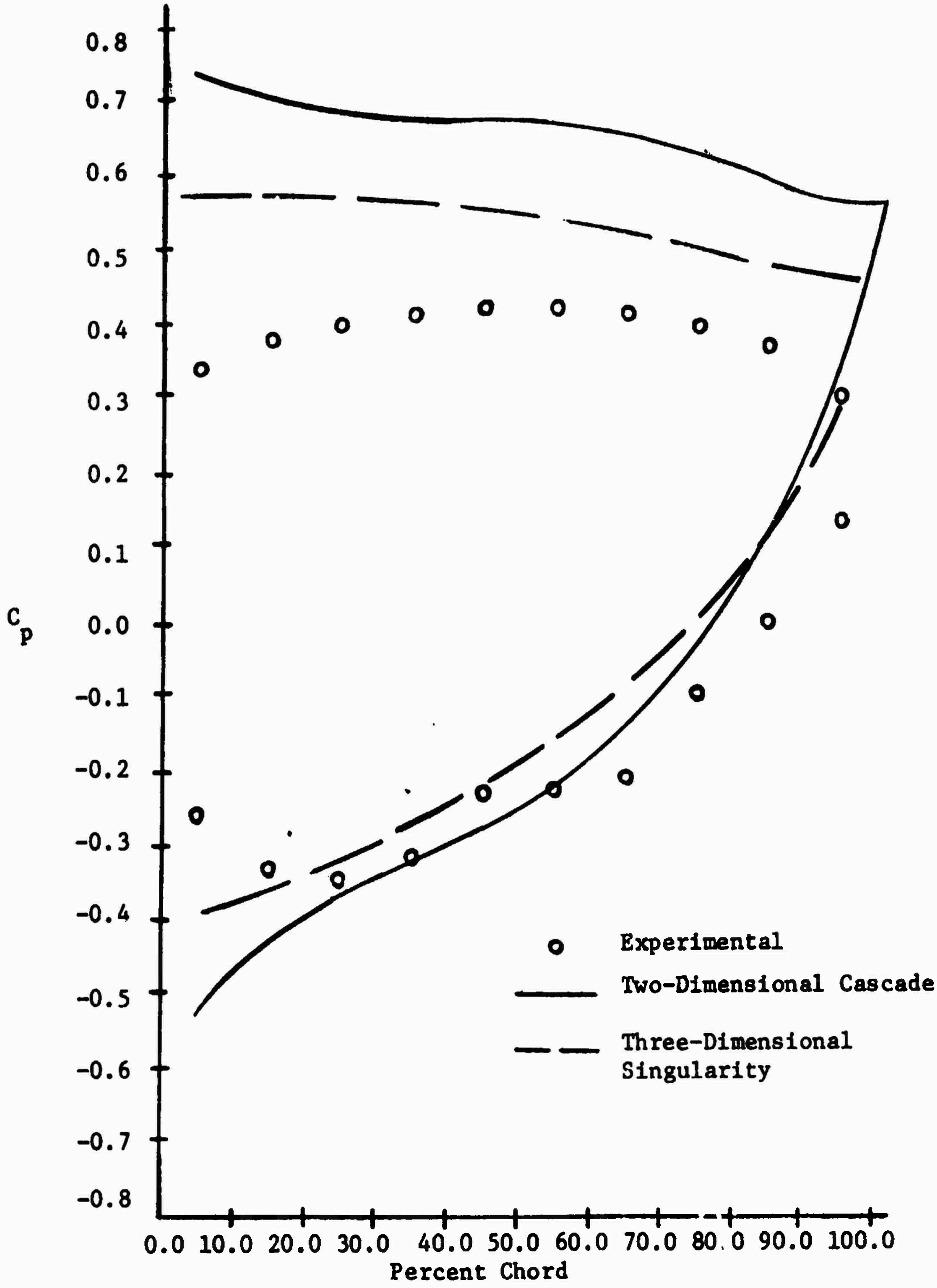

Figure 33. Experimental and Theoretical Static Pressure Coefficient Distributions for Test Rotor; Radial Blades ($\mu = 0^{\circ}$), $\eta = 0.861$ (3/4 Radius), $\phi = 0.130$.

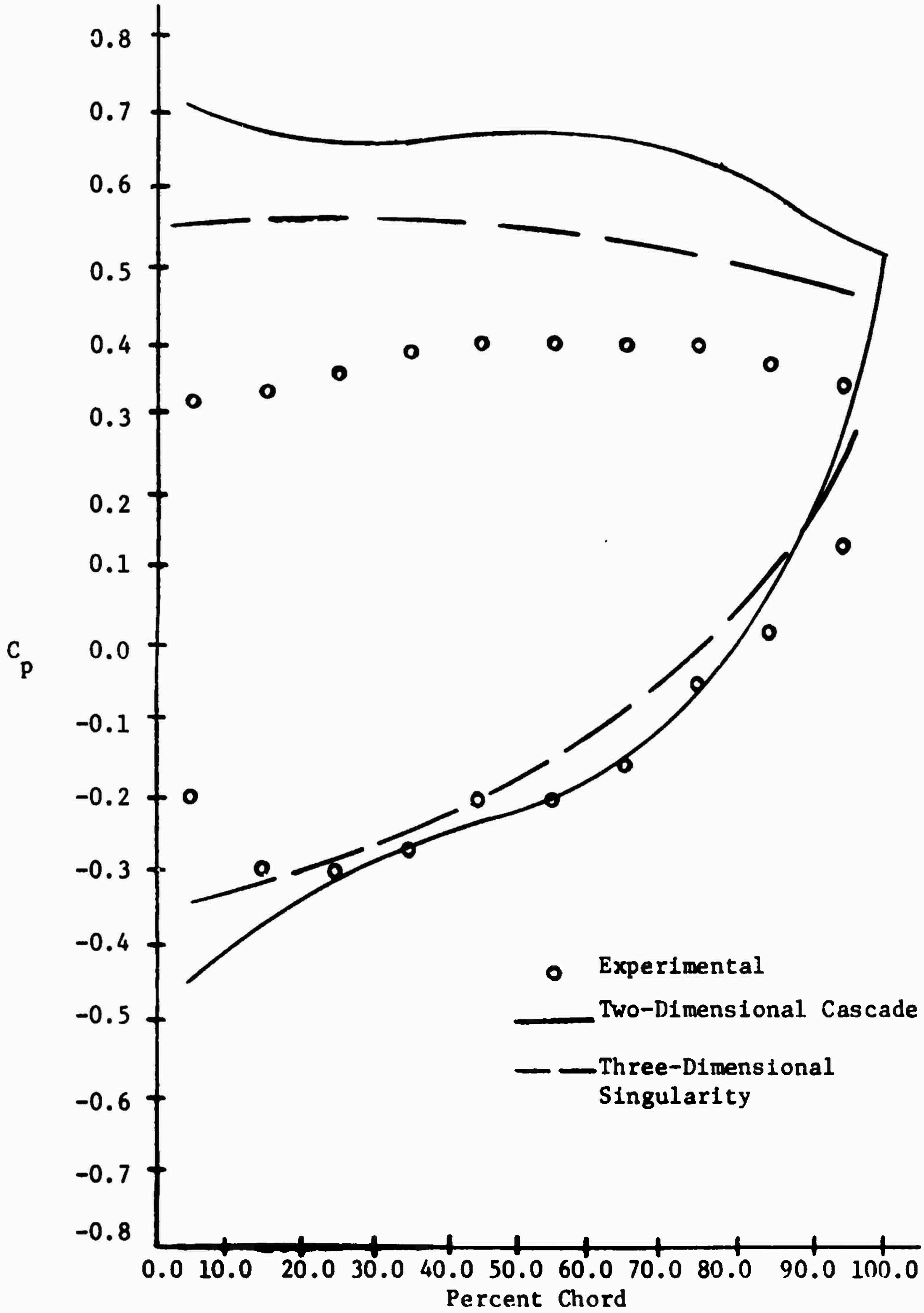

Figure 34. Experimental and Theoretical Static Pressure Coefficient Distributions for Test Rotor; Radial Blades ($\mu = 0°$), $\eta = 0.981$ (Tip), $\phi = 0.130$.

presented as angles relative to the rotating blade for convenience of comparison with theoretical predictions and interpretation. The static pressures are presented in coefficient form where C_p is based on the local relative inlet velocity at each radial position considered.

In addition to the measured flow outlet angles for three flow coefficients (Figure 24), the blade outlet angles predicted by two-dimensional cascade theory as well as the geometric stagger angles are presented for comparison.

The actual relative blade inlet angles at each radius were calculated from knowledge of the tangential velocity and axial velocity profile due to boundary layer growth. The inlet tangential velocity at each radius is known from local blade speed. In order to account for the inlet axial velocity profile induced by boundary layer growth on the walls of the AFRF, the absolute inlet axial velocity component at each radius was scaled in accordance with the velocity profile presented in Figure 17a. The relative blade inlet angles used for the theoretical predictions were thus calculated to correspond to the actual experimental conditions.

Although the outlet angles are of interest, the sensitivity of these measurements to even small regions of flow separation at the trailing edge causes their accuracy to be less reliable than the pressure distribution measurements, which have consequently been used in the reduction and interpretation of the data. Nevertheless, the flow angles do tend to provide validation of the other measurements. The measured angles agree reasonably well with the cascade predictions except near the hub and tip in those cases where separation is evident. The limited range of efficient operation of these blades is evidenced by the hub separation at $\phi = 0.22$ and $= 0.13$; further increase of ϕ to alleviate the hub separation causes tip separation at $\phi = 0.34$ due to negative incidence limitations.

The static pressure distributions measured along five radial positions on the surface of the rotating blades in the radial configuration are presented in Figures 25 through 34. Theoretical pressure distributions predicted by both two-dimensional cascade and three-dimensional singularity methods are also plotted for comparison. This data was obtained for two flow coefficients: $\phi = 0.22$ (Figures 25 through 29) and $\phi = 0.13$ (Figures 30 through 34).

The difference between the two-dimensional predictions and the measured values tends to confirm the anticipated three-dimensional flow effects. The three-dimensional theory, while generally showing good agreement, does not consistently verify the experimental data. Some of this erratic behavior is felt to be due to problems with the convergence of the numerical solution, and is discussed further in the subsequent section.

3.2.2 Dihedral Blade Configuration. The measurements described above for the radial blades were repeated for two blade configurations with dihedral. The measured values of flow angles and blade static pressure distributions at various radii for the design flow coefficient ($\phi = 0.22$) and one off-design condition ($\phi = 0.13$) for blades with dihedral ($\mu = -15^{\circ}$, -30°) are superimposed upon the radial blade data in Figures 35 through 46 for comparison. Only experimental pressure distributions are shown for the dihedral configurations since neither the two-dimensional cascade nor three-dimensional singularity theory is capable of an analysis of a blade with dihedral.

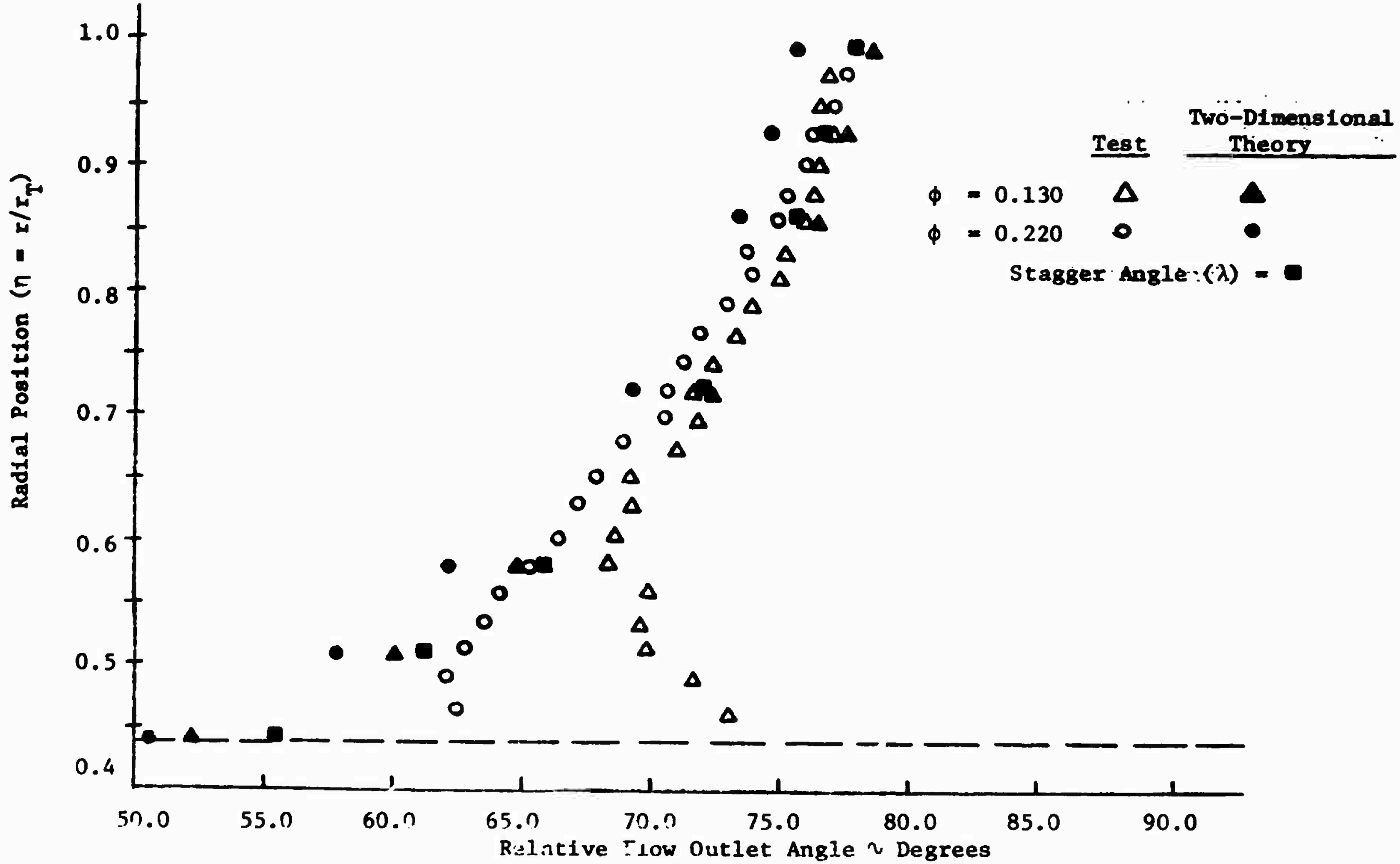

Figure 35. Flow Outlet Angle Summary for Blades with Dihedral ($\mu = -15^{\circ}$).

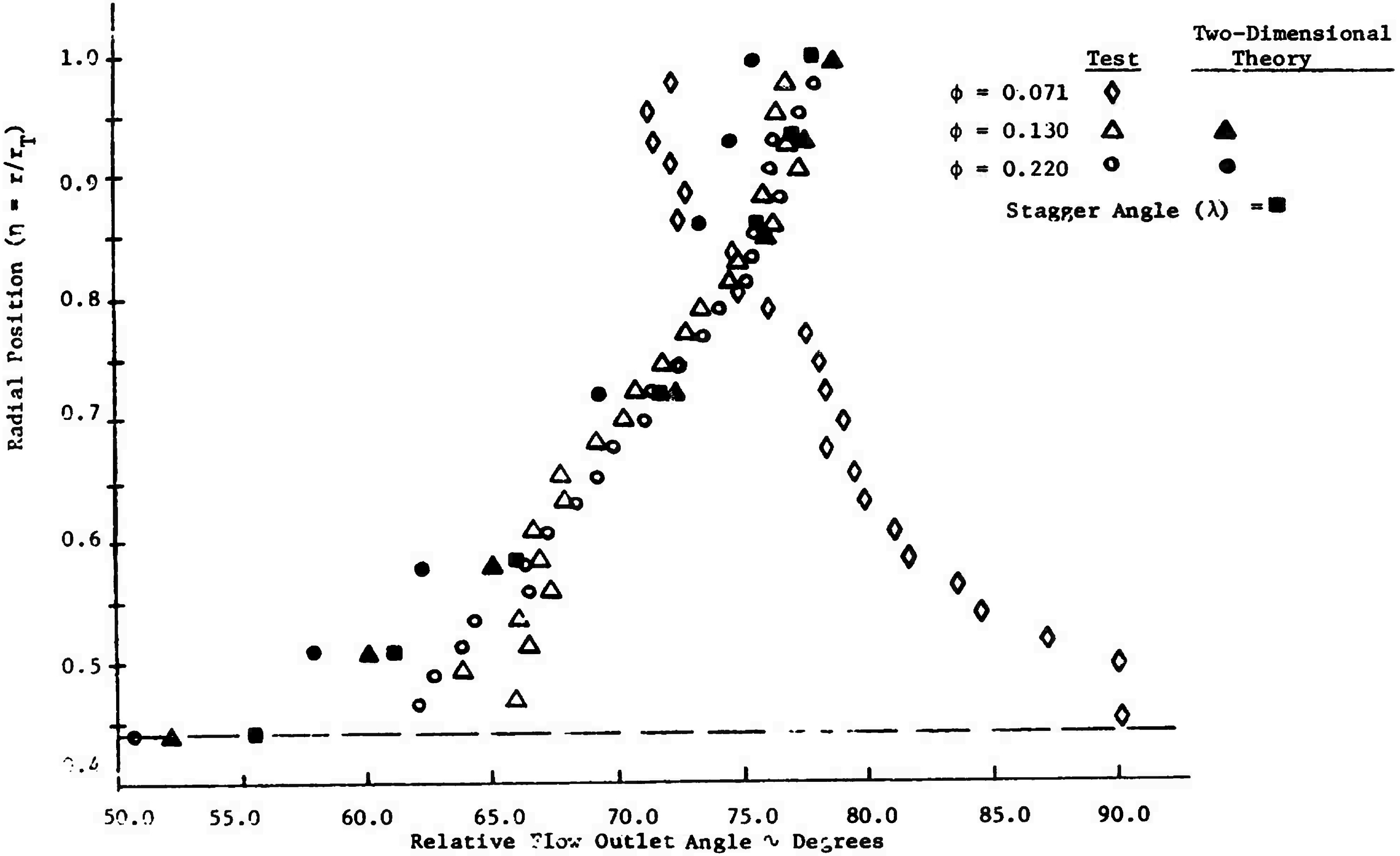

Figure 36. Flow Outlet Angle Summary for Blades with Dihedral ($\mu = -30^{\circ}$).

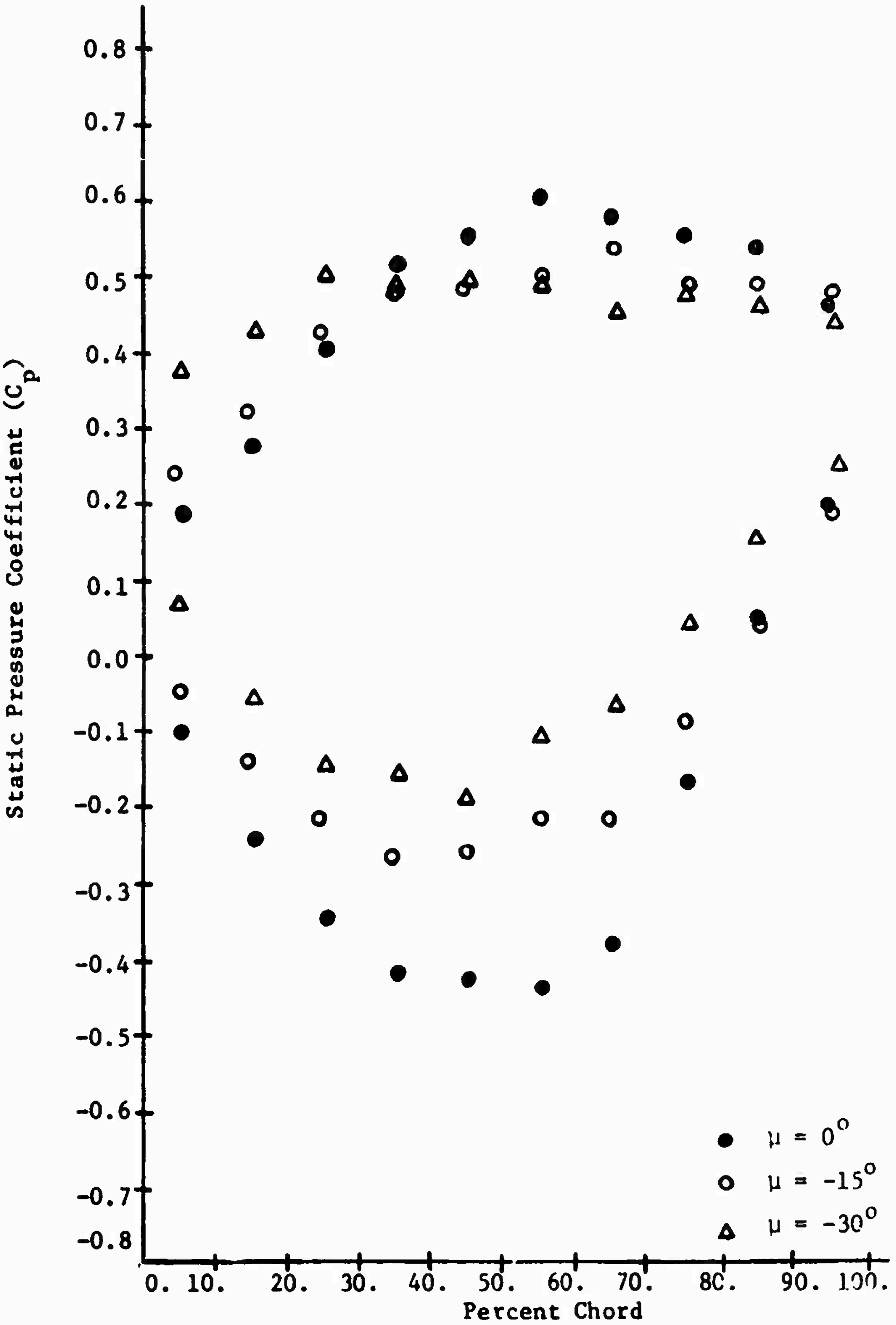

Figure 37. Experimental Static Pressure Coefficient Distributions for Test Rotor at Three Dihedral Angles (μ); Radial Position $\eta = 0.511$, Flow Coefficient $\phi = 0.220$.

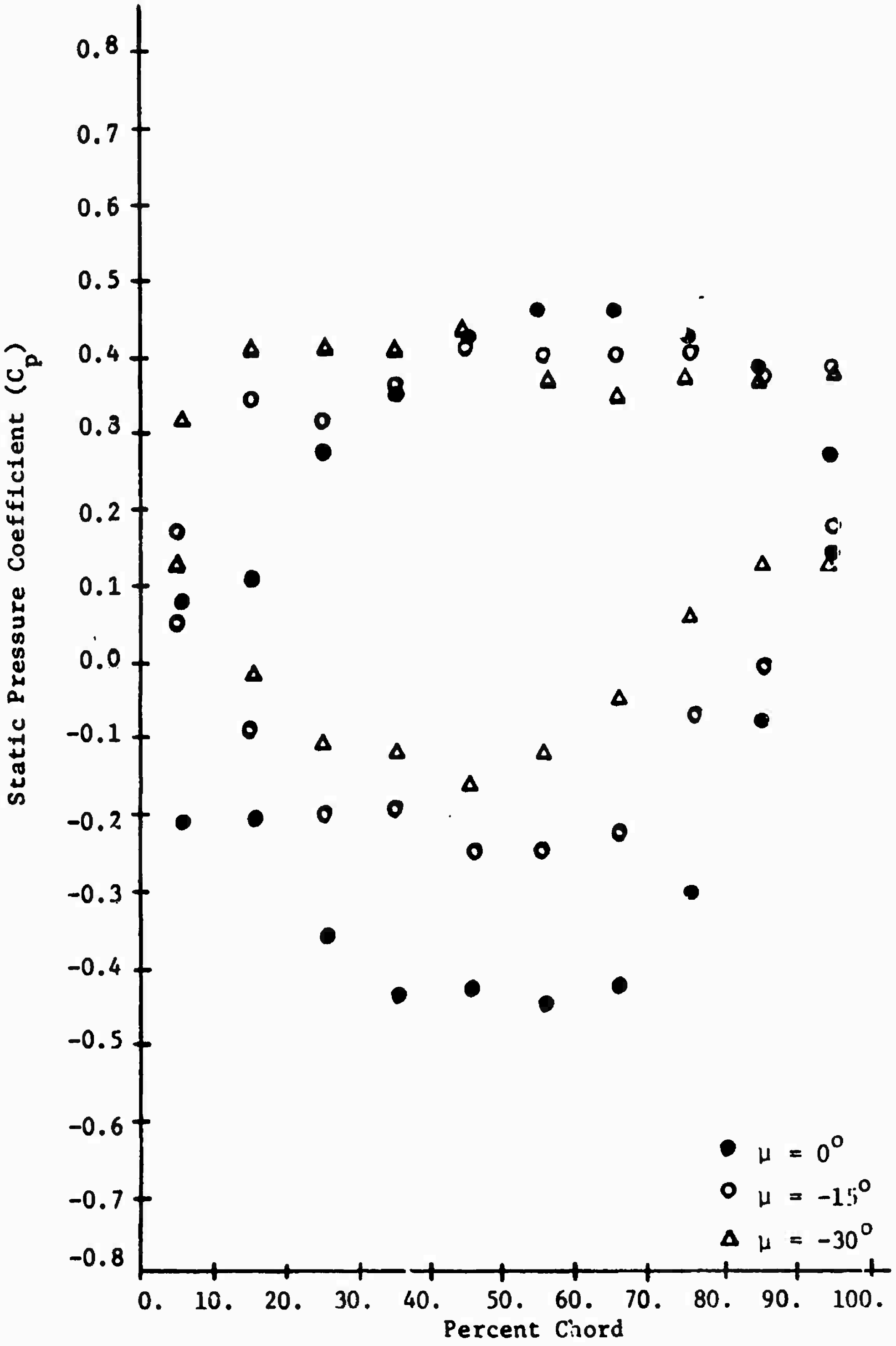

Figure 38. Experimental Static Pressure Coefficient Distributions for Test Rotor at Three Dihedral Angles (μ); Radial Position $\eta = 0.581$, Flow Coefficient $\phi = 0.220$.

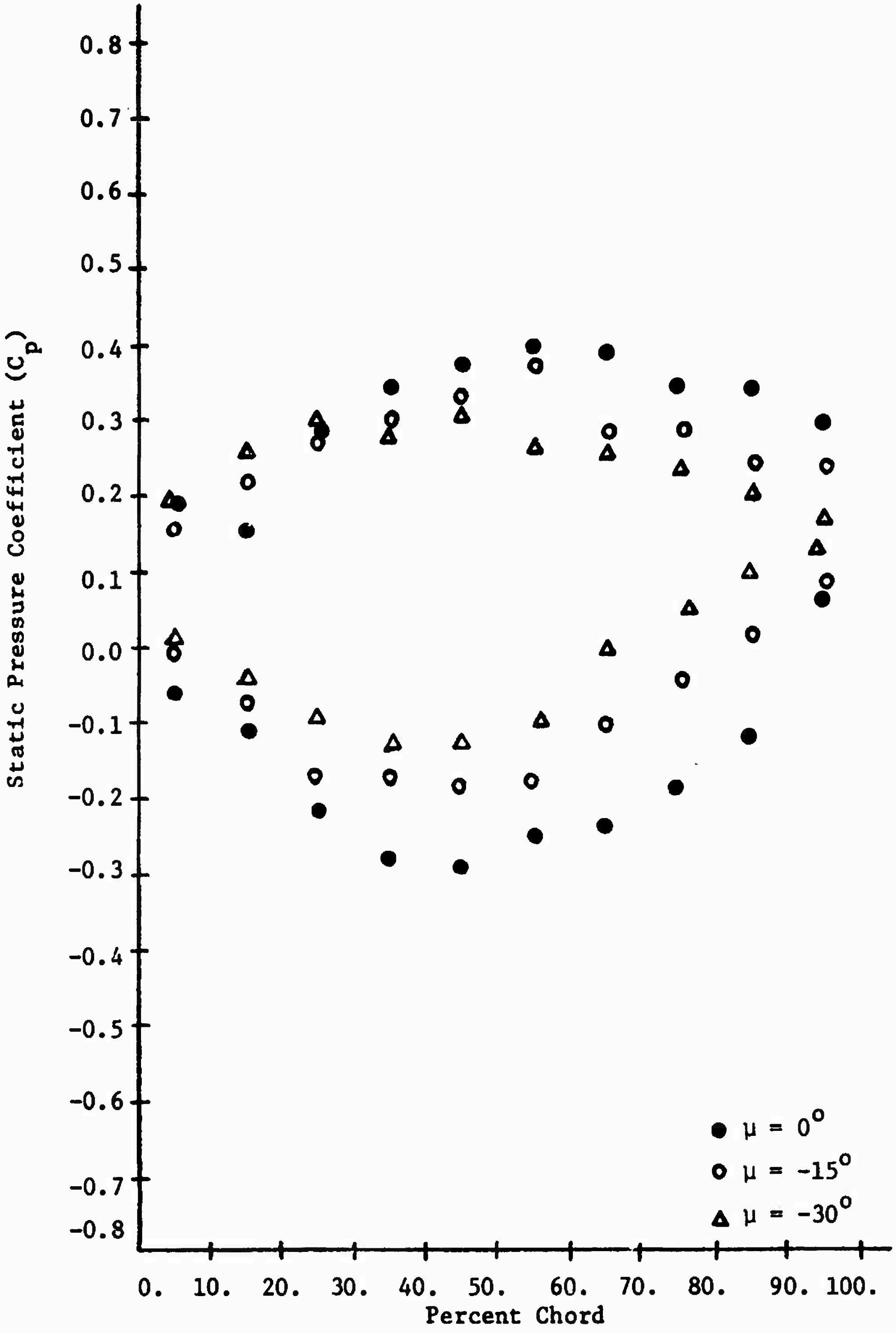

Figure 39. Experimental Static Pressure Coefficient Distributions for Test Rotor at Three Dihedral Angles (μ); Radial Position $\eta = 0.721$, Flow Coefficient $\phi = 0.220$.

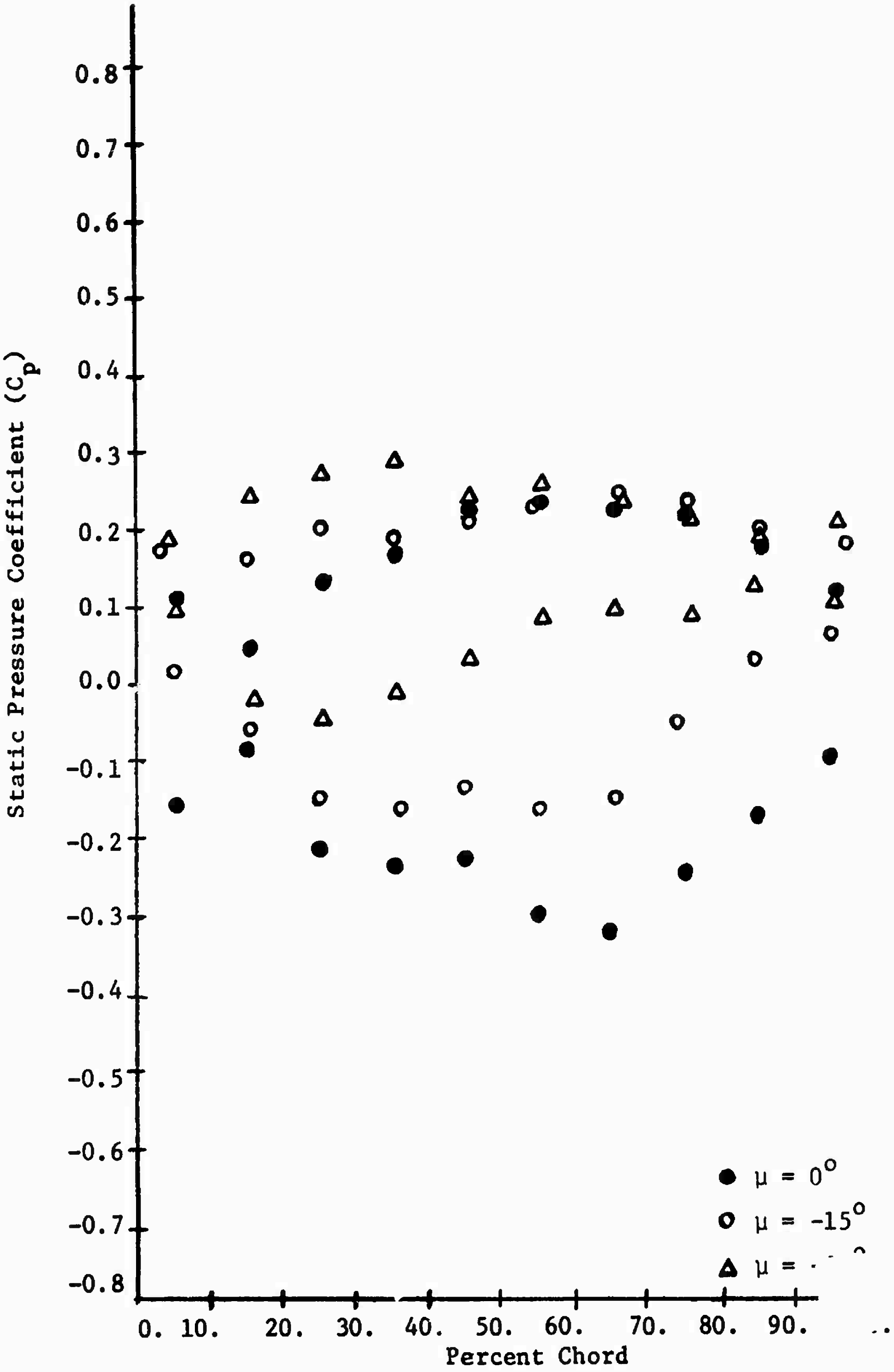

Figure 40. Experimental Static Pressure Coefficient Distribution for Test Rotor at Three Dihedral Angles (μ); Radial Position η = 0.861, Flow Coefficient ϕ = 0.220.

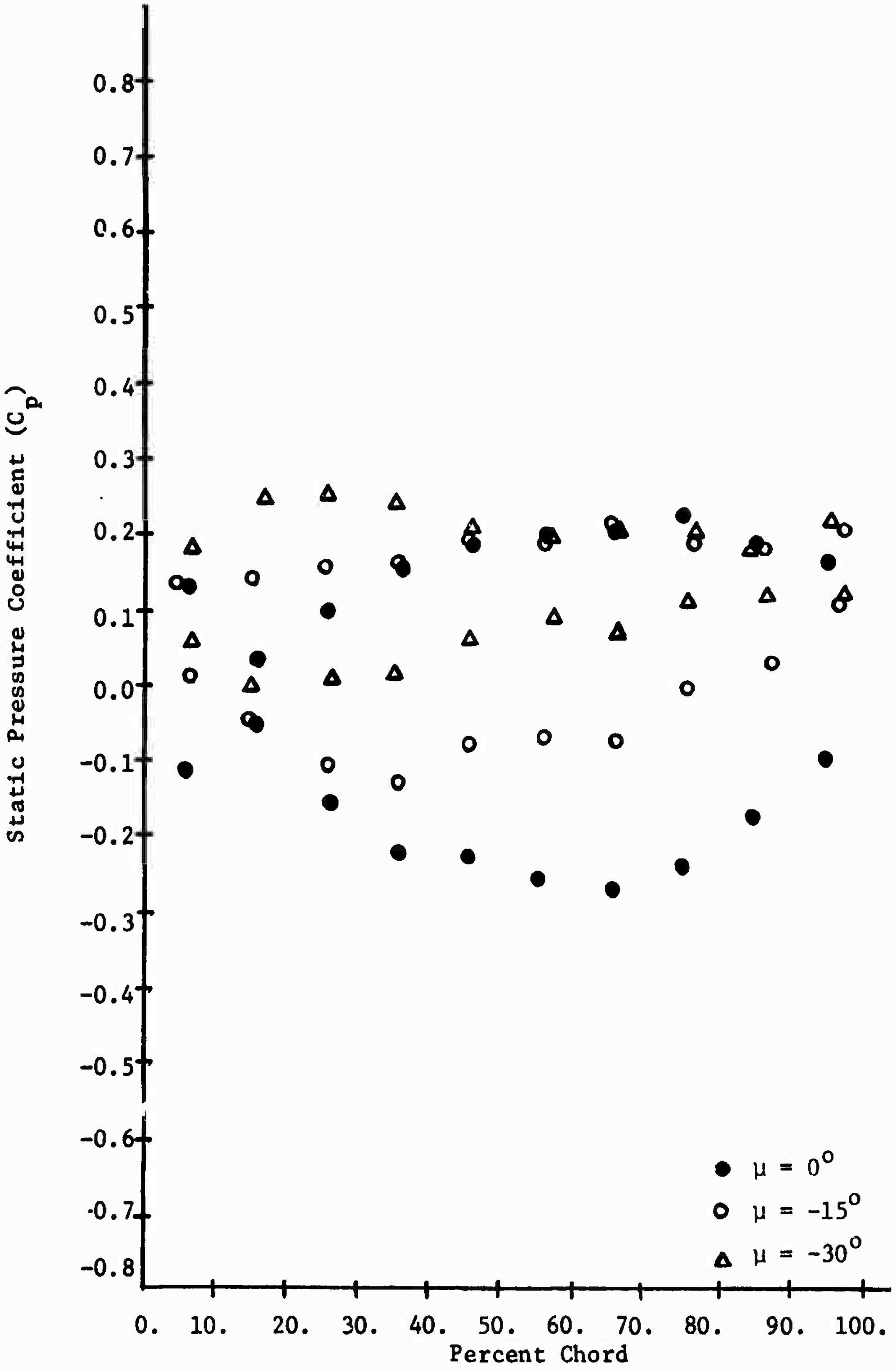

Figure 41. Experimental Static Pressure Coefficient Distributions for Test Rotor at Three Dihedral Angles (μ); Radial Position η = 0.981, Flow Coefficient ϕ = 0.220.

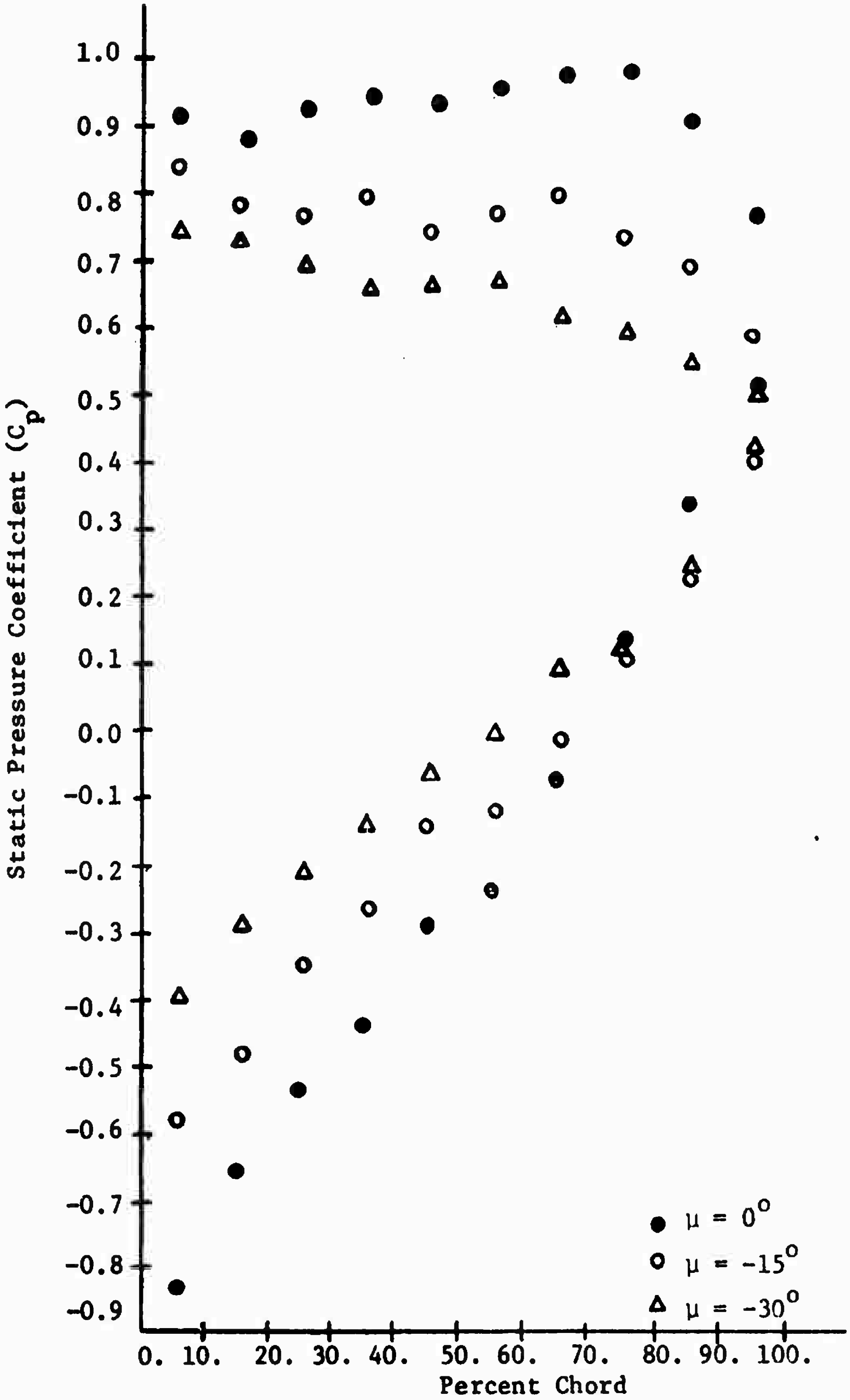

Figure 42. Experimental Static Pressure Coefficient Distributions for Test Rotor at Three Dihedral Angles (μ); Radial Position $\eta = 0.511$, Flow Coefficient $\phi = 0.130$.

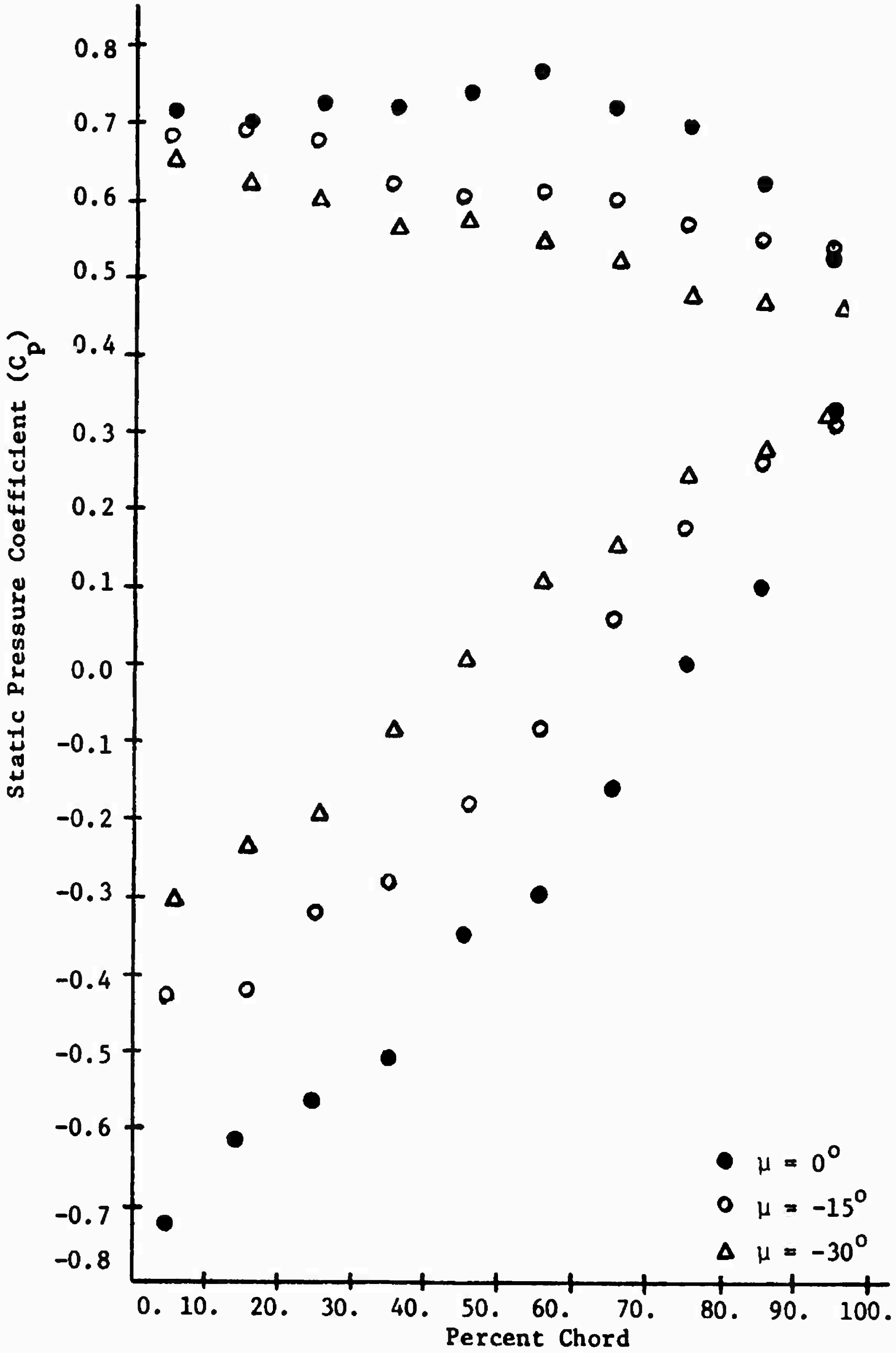

Figure 43. Experimental Static Pressure Coefficient Distributions for Test Rotor at Three Dihedral Angles (μ); Radial Position η = 0.581, Flow Coefficient ϕ = 0.130.

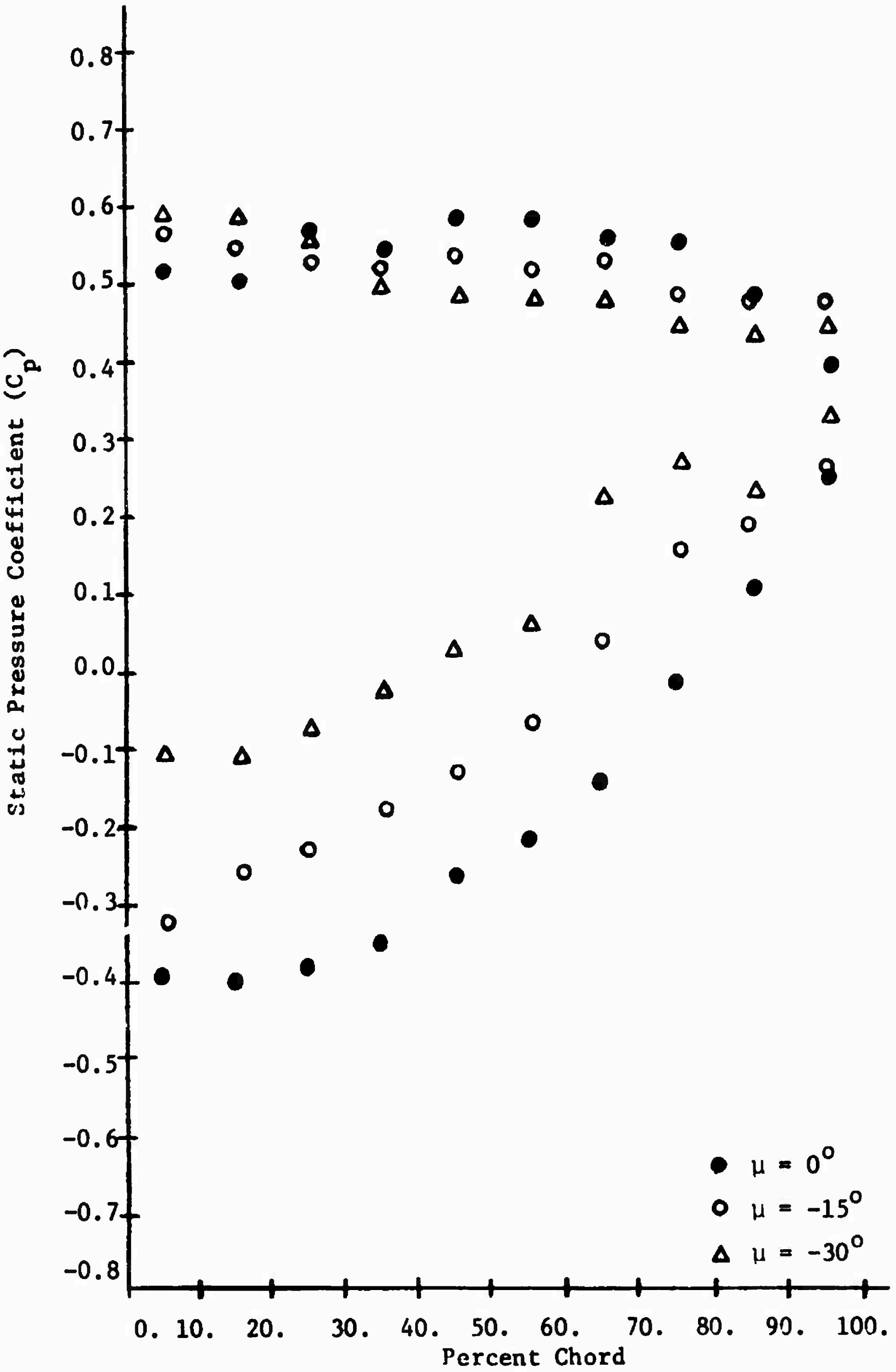

Figure 44. Experimental Static Pressure Coefficient Distributions for Test Rotor at Three Dihedral Angles (μ); Radial Position $\eta = 0.721$, Flow Coefficient $\phi = 0.130$.

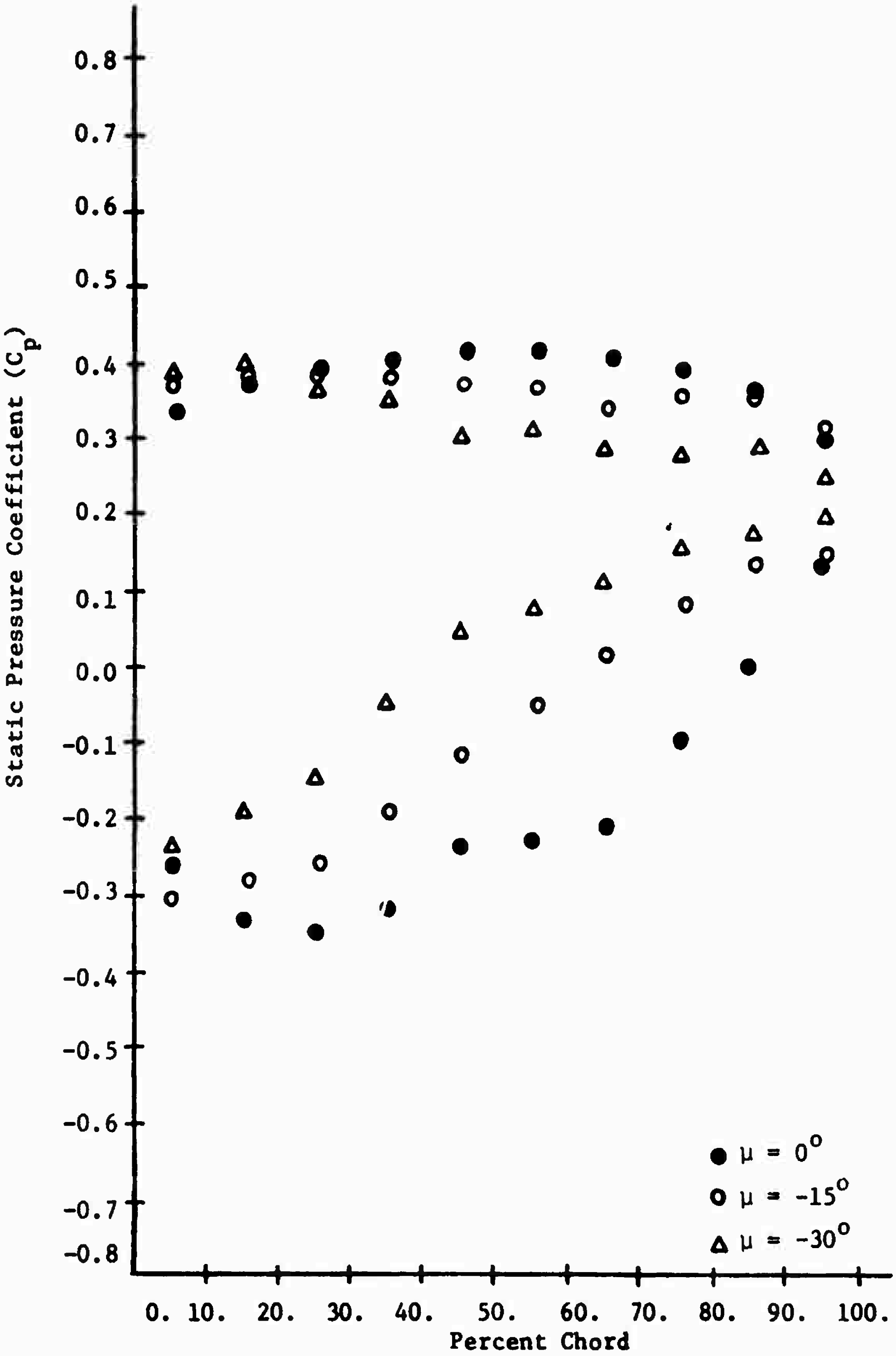

Figure 45. Experimental Static Pressure Coefficient Distributions for Test Rotor at Three Dihedral Angles (μ); Radial Position $\eta = 0.861$, Flow Coefficient $\phi = 0.130$.

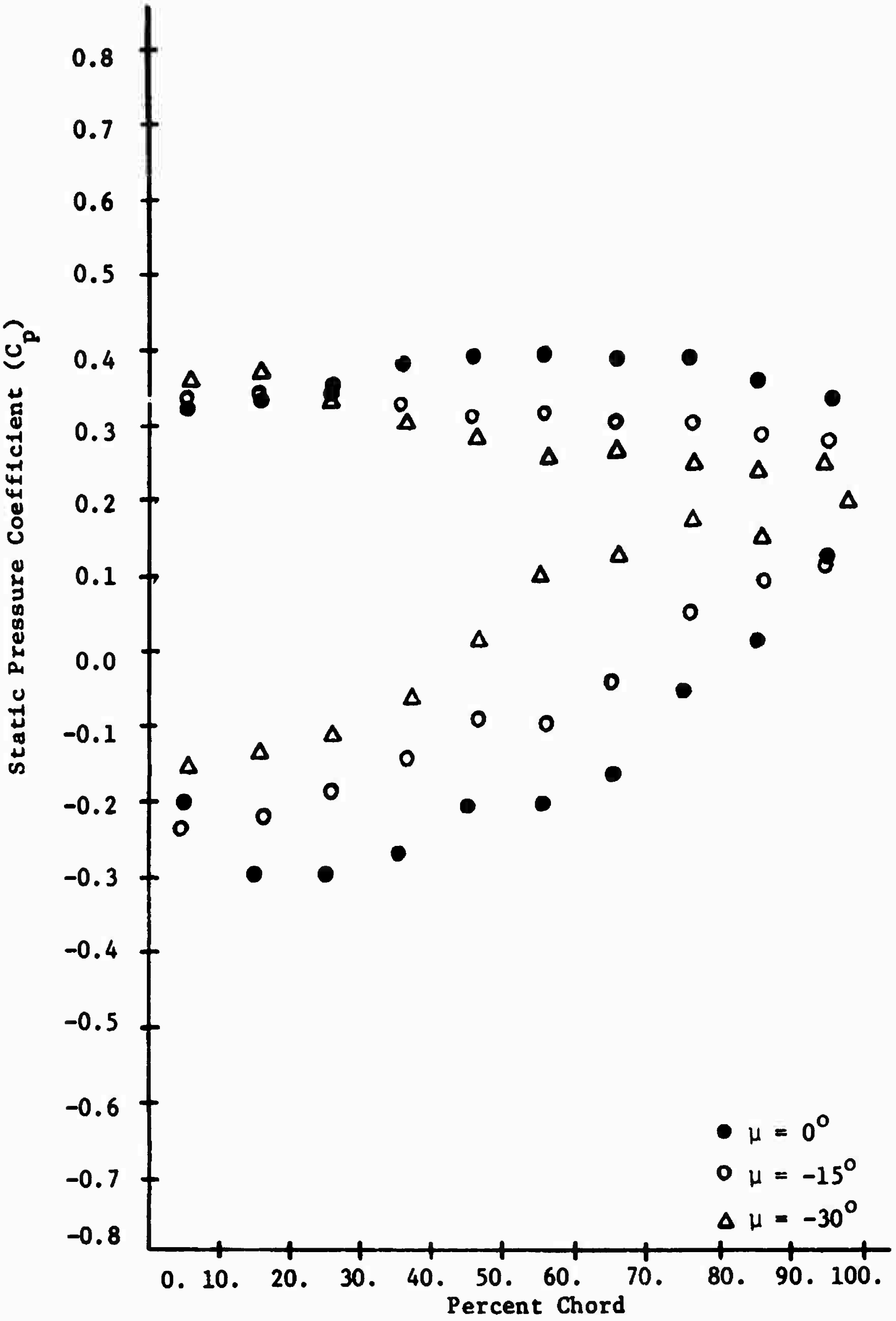

Figure 46. Experimental Static Pressure Coefficient Distributions for Test Rotor at Three Dihedral Angles (μ); Radial Position $\eta = 0.981$, Flow Coefficient $\phi = 0.130$.

The flow outlet angle measurements for both dihedral angles again indicate separation and a narrow range for efficient operation (Figures 35 and 36). The outlet angles for the $\phi = 0.220$ case increase with increasing dihedral angle and are generally greater than in the radial case indicating less flow turning, which is consistent with the decreasing trend exhibited by the pressure distribution data presented below. Conversely, the more highly loaded $\phi = 0.130$ case exhibits a general decrease of outlet angle with increasing dihedral angle. This seemingly paradoxical trend is probably due to the blade boundary layer separation becoming less severe as a consequence of the unloading effect of increasing dihedral angle.

Since the same blades were used for both the radial and dihedral experiments, interpretation of the data must consider the variation of the geometry and possible error in the data induced by it. The blades were designed to span the 6-inch annular flow region of the AFRF when mounted radially, and the blade edges at the tips were cut square with a 0.1 inch tip clearance (Figure 22a). When these same blades are mounted at a dihedral angle, three effects which must be evaluated are the variation of the radial location of the static pressure orifices, the change in tip clearance, and the different geometric relationship between annulus wall and blade tip. These conditions are depicted in Figure 22b and discussed below.

When the blade is mounted radially, the static orifices on the suction and pressure sides both lie on the same cylindrical surface. When the blades are mounted at a dihedral angle, however, the tipping over effect causes the orifices on the side of the blade toward the direction of dihedral to move toward the hub while the orifices on the opposite side move toward the tip, relative to their positions for the radial case. Nevertheless, this condition has been neglected since the maximum deviation ($\Delta\eta$) of the static orifice location from the corresponding radial case was calculated as about $\Delta\eta = \pm.02$. This maximum $\Delta\eta$ occurs near the hub due to the greater blade thickness, and is even smaller at all other radii.

When tilted and mounted at a dihedral angle, the blade span necessary to extend from hub to annulus wall is increased over the radial value. For $\mu = 30^\circ$, the effective span across the annular flow region of the AFRF becomes 6.34 inches. Part of this effective span increase is compensated by the increase in actual mean blade span to 6.12 inches achieved by the blade-to-hub adapter block. Therefore, the resulting tip clearance (C_t) increases from the 0.1 inch value in the radial case to 0.22 inch for the maximum dihedral case when $\mu = -30^\circ$. Presenting the tip clearance as non-dimensional values normalized by the blade span, (C_t'), the tip clearance for the radial and maximum dihedral cases are 0.017 and 0.036, respectively. As a result, the decrease of blade performance near the tip region due to tip clearance should be more severe for the blade with dihedral.

Again referring to Figure 22, in the radial case, the blade tip is parallel to the annulus wall and the resulting tip clearance region is channel-shaped. In contrast, the dihedral mounting results in a wedge-shaped tip clearance gap. The effect of this tip clearance region shape variation on the test data is uncertain.

Although the method used to achieve blade dihedral involves some inaccuracy, especially at the tip, it is insufficient to account for the large loss of lift observed near the blade tip and root section.

According to Smith and Yeh (33), the blade sections should be viewed along the blade stack up axis. This results in very little change in the blade camber or profile for this particular case.

3.2.3 Summary of Rotor Performance. In order to evaluate the effect of dihedral at each radial position, the variation of section lift coefficient with dihedral angle was examined. The ratio of section C_L, which was derived from the blade pressure distribution and normalized by the value of section C_L at $\mu = 0^o$, is plotted in Figure 47. The degradation of blade performance with increasing dihedral angle is evident at each radial section. However, the relative magnitude of this variation implies that a rather complex interaction of factors is in play, and this will be further considered in Chapter IV.

The overall performance of the test rotor over the ranges of flow coefficient and dihedral angle considered is depicted in Figure 48. The blade loading coefficients (ψ_1) for each of five radial sections were calculated from measurements of the areas under the experimental blade static pressure coefficient plots, and subsequently, these curves were obtained by mass averaging the performance at these sections along the blade span. Decrease in blade loading with increase in dihedral angle is evident from Figure 48. Values of $\bar{\psi}$ derived from stagnation pressure measurements, plotted in Figure 48, show good agreement with the values derived from the blade pressure distribution. This provides a good check on both the measurements.

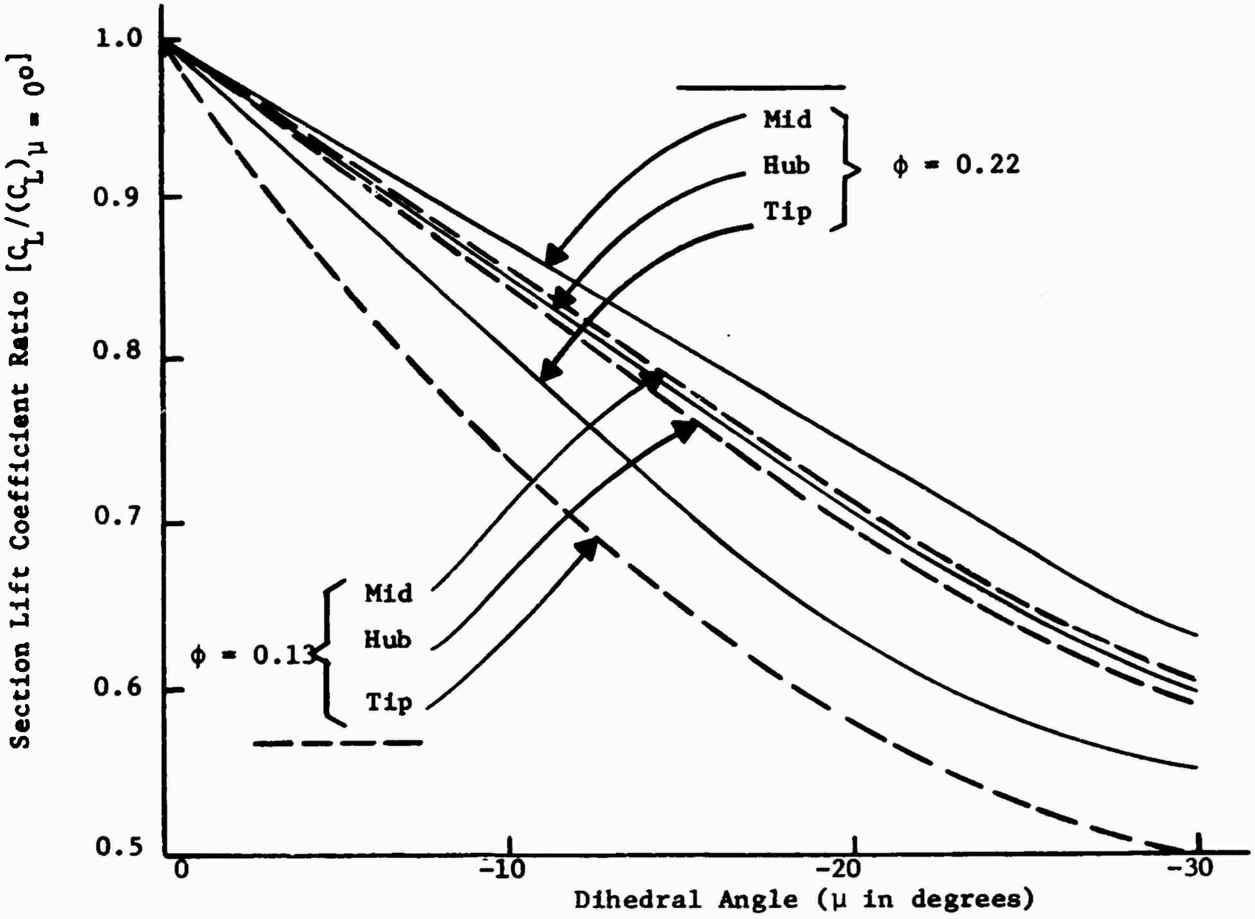

Figure 47. Effect of Dihedral Angle on the Section Lift Coefficient.

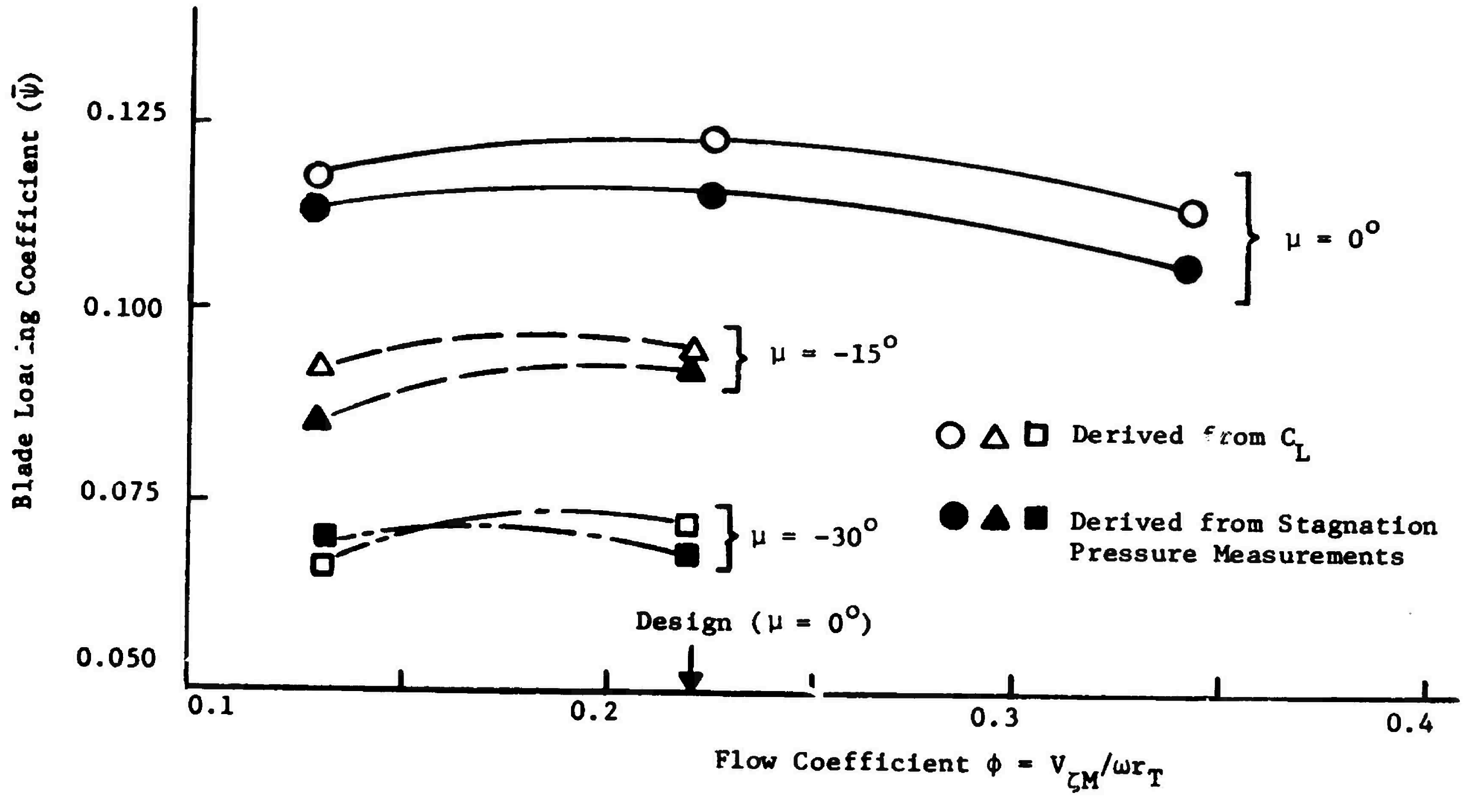

Figure 48. Effect of Dihedral on the Overall Performance of Test Rotor.

CHAPTER IV

DISCUSSION AND INTERPRETATION

4.1 Radial Configuration: Interpretation of the Data and Comparison with the Theory

The procedure applied to calculate the theoretical values was discussed in section 2.3.2. Comparison of the two- and three-dimensional theoretical predictions and the experimental data for the radial blade configuration tends, in general, to confirm the three-dimensional flow effects hypothesized based on the analytical work. The three-dimensional data and predictions generally exhibit a greater area (than two-dimensional predictions) under their pressure coefficient plots near the hub region (Figures 25, 26, 30 and 31) and smaller areas near the tip region (Figures 28, 29, 33 and 34). This is consistent with the higher hub and lower tip circulation in the three-dimensional case found previously.

Near the hub, away from the walls (Figure 26, $\eta = 0.581$), the suction pressures are predicted more accurately by the three-dimensional theory. Accurate prediction of minimum suction pressures is important from the point of view of estimating the cavitation effects in liquid handling machinery. It must be noted that the agreement between two- and three-dimensional theory at mid radius ($\eta = 0.72$) is not the result of analysis, but rather due to the imposed condition of equality at several points on the blade surface. The agreement between theory and experiment is good at this location. Near the tip, the suction surface pressures are predicted more accurately by the three-dimensional theory, but the agreement on the pressure surface is poor with both theories.

The influence of tip clearance may account for the discrepancy between theory and experiment observed at these tip locations (34).

Near the hub sections (Figure 25) the significant difference between two- and three-dimensional theory occurs from about mid chord to the trailing edge on both suction and pressure surfaces. Near the tip (Figures 29, 34), however, the discrepancy is greatest on the pressure surface, while the suction surface agrees reasonably well except very near the trailing edge. The considerably lower pressure surface pressure coefficients at the tip for the data as compared to three-dimensional predictions indicate significantly less circulation and the probable occurance of tip clearance losses (34).

The lift coefficient derived from the blade pressure distributions for $\phi = 0.13$ is plotted and compared with two-dimensional and three-dimensional theories in Figure 49. Near the hub, the two-dimensional theory under predicts and the three-dimensional theory over predicts the lift coefficient. The discrepancy between the three-dimensional theory and the experiment at this location may be due to real fluid effects (e.g. wall stall). Near the tip, the trend is reversed and the discrepancy between the two-dimensional theory and the experiment is as much as 60% while that between the three-dimensional theory and the experiment is 20%. The predictions from the three-dimensional theory show better agreement with the experiment throughout and the trend (i.e. higher lift at the hub and lower lift at the tip than two-dimensional values) is correctly predicted.

Oshima et al. (35) investigated the difference in blade performance of a pump rotor and the corresponding cascade. Comparing three-dimensional data obtained from tests on various rotating impellers with

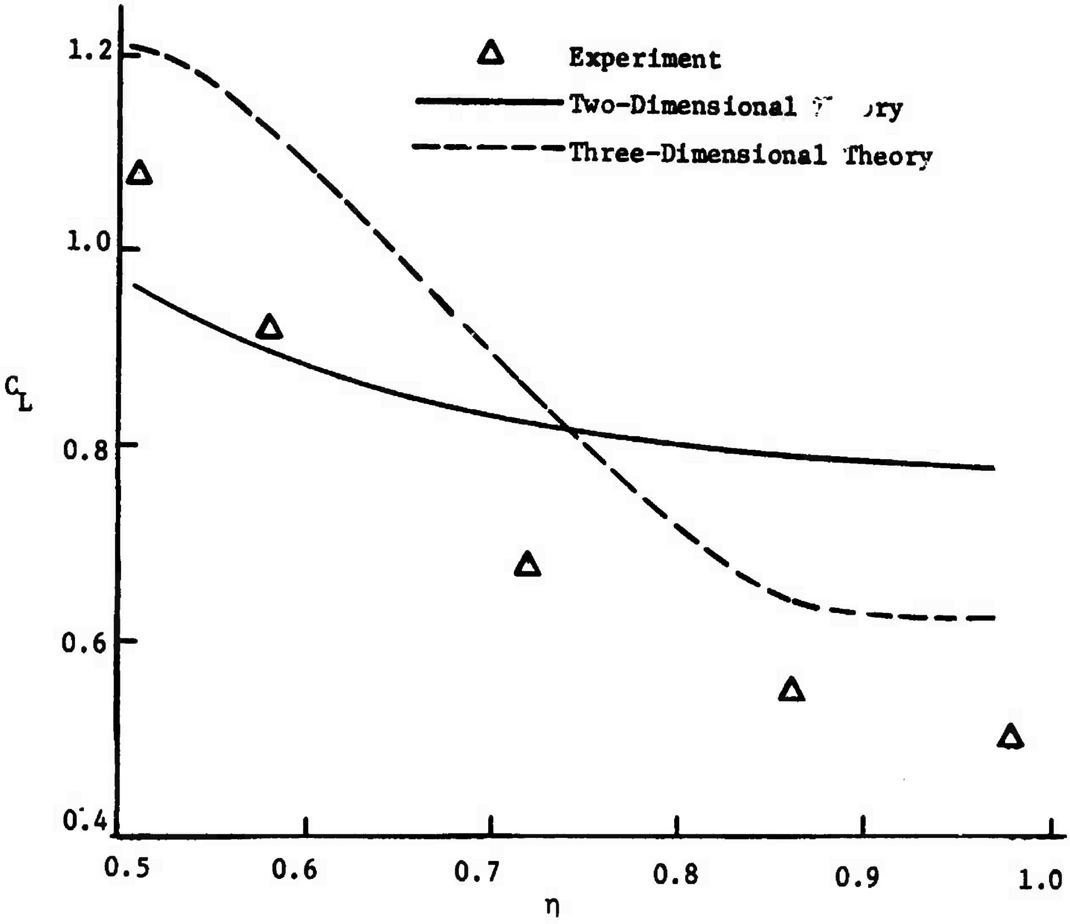

Figure 49. Experimental and Theoretical Distributions of Lift Coefficient for the Test Rotor, $\mu = 0^{\circ}$ and $\phi = 0.13$.

experimental two-dimensional cascade data for the individual profiles used to design the impellers, significant discrepancies between the rotating and stationary data were evident. The experimental lift coefficients measured at the hub were greater and those measured at the tip were less than the two-dimensional predictions. Oshima attributed this to centrifugal and Coriolis forces acting on the three-dimensional boundary layer, tip clearance effects, and the annulus wall boundary layer. These effects of rotation are undoubtedly important, but the three-dimensional inviscid effect must also be considered. Although this effect is not related to the rotation, it is certainly responsible for a significant part of the discrepancy between the rotating three-dimensional (rotor) and stationary two-dimensional (cascade) data, as shown in Figure 49. The discrepancies observed by Oshima et al. follow the trends predicted herein by the three-dimensional potential flow analysis.

It was discussed previously that the two- and three-dimensional solutions at the mid radius are only approximately the same. This is further evidenced by the experimental blade pressure distributions. Although the data and both theories agree well for $\phi = 0.220$ (Figure 27), the pressure coefficient plot shapes for the more highly loaded $\phi = 0.130$ case emphasize the actual difference between the solutions. The two- and three-dimensional theories at the mid radius are not equal but rather behave similarly to the tip section, but to a much smaller extent, consistent with Figure 11. Thus, a source of inaccuracy in the analytical technique used is the mid radius condition whereby the two- and three-dimensional solutions are set equal at the mid radius. This is only approximately true for low hub/tip ratios and higher blade loadings as evidenced by the theoretical analysis and experimental data.

Since the singularities used to represent the test rotor in the three-dimensional model were located at 5, 15, 25, etc. percent chord, the points at which the blade pressure coefficients were calculated were selected midway between these, or at 10, 20, 30, etc. percent chord. This was done to minimize convergence problems which become more severe closer to the singularities. Nevertheless, some waviness of the three-dimensional predictions was experienced and the dotted lines shown in Figures 25 through 34 represent an average curve through the theoretical points. Utilization of a greater number of weaker singularities and calculation of more eigen values is necessary to smooth the theoretical three-dimensional curve.

The real fluid effects due to hub and annulus wall boundary layer growth within the AFRF were considerable as exhibited by the measured inlet velocity profiles. Although these effects were compensated for, they could not be eliminated entirely. Also, boundary layer growth in the blade, especially at the tip where the chord is very large, had some influence. The influence of a finite tip clearance is not considered by either two- or three-dimensional theories utilized. A semi-empirical relation presented by Lakshminarayana (34) indicates a loss of stage efficiency for the radial blade configuration of about 1.4% due to tip clearance. For the increased clearance of the dihedral blades, their loss of efficiency increases to about 2.9%. Thus, for all cases, the theoretical pressure distributions were expected to predict better performance near the blade tip regions than observed experimentally.

4.2 Dihedral Configuration: Interpretation of Data for Blade with Dihedral and Comparison with the Radial Configuration

The blade configuration with dihedral has been treated only experimentally, since the present three-dimensional theory cannot handle a singularity line that does not lie along a radial line from the hub to annulus walls. The difficulty lies with the boundary condition requiring no radial flow, or no flow normal to the wall, at the point of intersection of the singularity line and the end wall. For a radial blade, the singularity line intersects the end wall perpendicularly and the boundary condition is easily satisfied. For a blade with dihedral, the singularity lines intersect the walls at an angle, and the elemental strength of the singularity induces velocity perturbations normal to the wall (Figure 50). The present theory must be modified or an entirely new approach must be developed to predict such flows. The mathematical representation should involve a zero circulation at the tip (unlikely from physical considerations) or a trailing vortex system which in combination with the blade vortex system will provide a zero radial flow velocity at the wall.

Since some of the terms applied to describe blade configuration vary somewhat depending on the specific engineering discipline (e.g. marine, aerospace, etc.), a brief discussion of a few relevant terms is included here to aid the reader. Some modern compressors and pumps are designed to have "sweep" as well as "dihedral". This terminology is similar to that used for aircraft wings. Turbomachinery is said to have "sweep" when the flow direction is not perpendicular to the spanwise direction (33). A rotor has "dihedral" when the blade surface is not normal to the surfaces of an endwall (casing or hub) as shown in Figure 51.

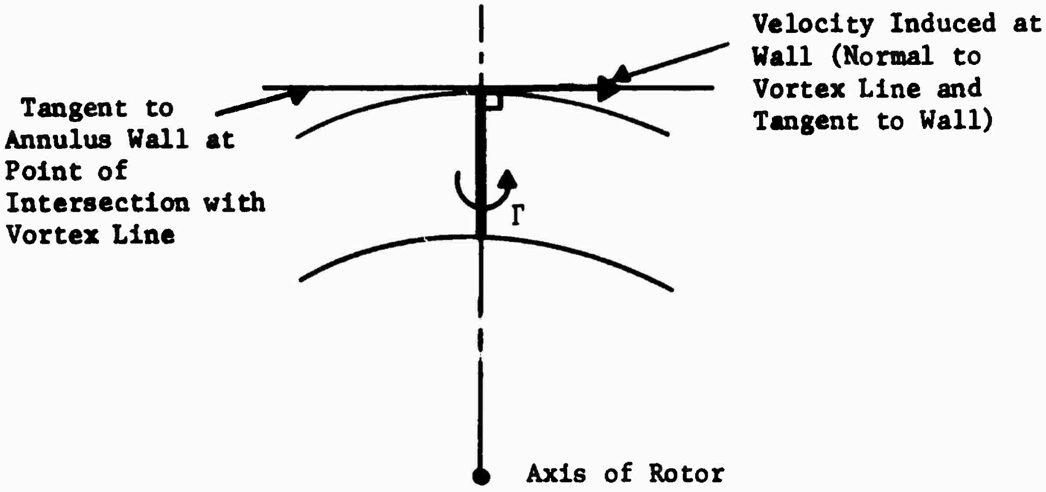

a. Radial Vortex Line

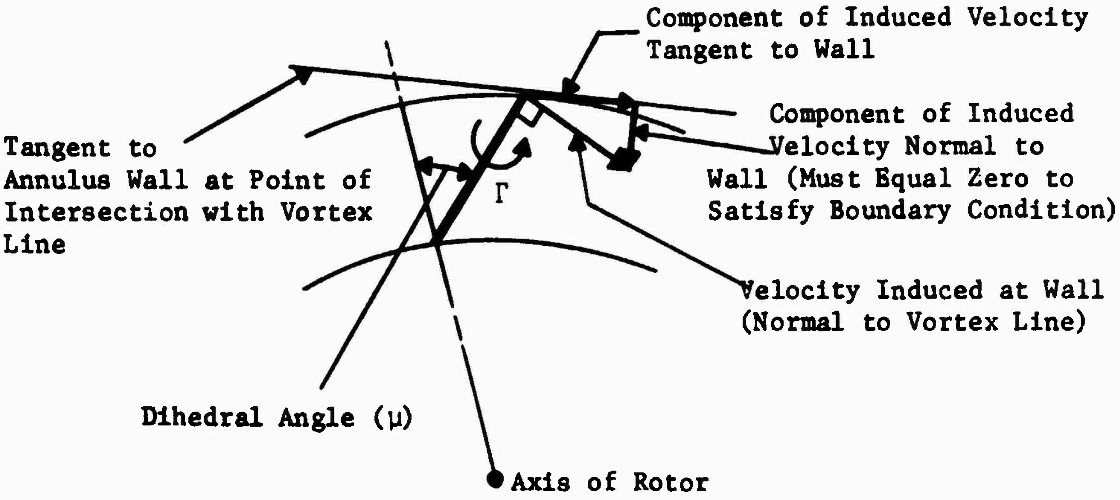

b. Non-Radial Vortex Line

Figure 50. Potential Flow Theory Boundary Condition at Hub and Annulus Wall for Vortex Line Spanning an Annulus.

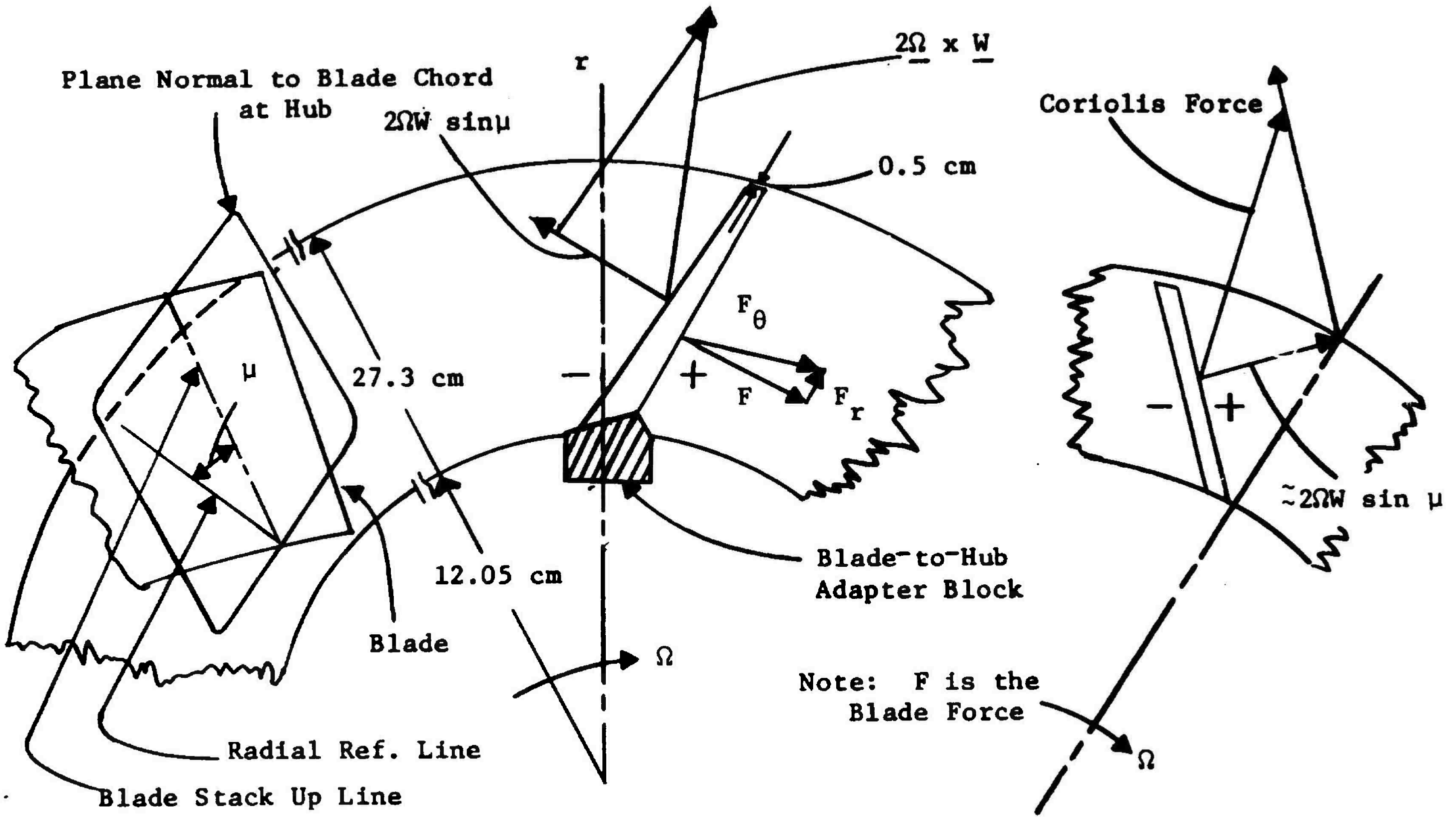

a. Experimental Configuration with Negative Dihedral

b. Positive Dihedral

Figure 51. Dihedral Blade Mounting.

Dihedral will result from blade stack up and twist. Similar terminology used by propeller hydrodynamicists are "skew" and "rake". "Skew" is defined as the displacement of propeller blade sections successively along their relative pitch helices (36). This term is analagous to the sweep used in aircraft wings. The increased resistance to the cavitation of a propeller due to "skew" is analagous to increase in the critical Mach number achieved by a swept aircraft wing or a compressor blade. "Rake" in the propeller field is defined as the longitudinal displacement forward or aft of the blade sections successively from the radial direction (36). The "rake" prevents overhang of the skewed blade from the propeller hub.

Most turbomachinery will have some amount of dihedral. But for aircraft compressors with swept blades, flared annuli and staggered blades, there will always be some amount of sweep and dihedral. Combination of "skew" and "rake" will also give rise to dihedral. The major effects of dihedral are to produce a radial blade force (Figure 51) which serves to disturb the meriodional flow; produce a Coriolis force in the direction normal to the blade which alters the stability and other characteristics of the blade boundary layer; and alter the wall stall characteristics near the blade ends. These effects will result in appreciable change in the performance of the blade row as compared to one without dihedral.

Considering the wall boundary condition discussed previously for a blade with dihedral, certain qualitative trends in the blade performance can be identified. Although a complete dimunition of the circulation at the hub and tip to zero is not a physical condition likely of realization, certainly a reduction of circulation in these regions can be anticipated. This implies that the hub and tip of a blade with dihedral should not perform as well as an identical blade mounted radially. Furthermore, since a greater dihedral angle corresponds to a greater normal component of velocity at the wall, the circulation in such a case would have to decrease more rapidly near the tip and/or start to decrease closer to the mid radius. Hence, the performance degradation may be expected to become more severe with increasing dihedral angle. This qualitative effect of dihedral angle corresponds to the experimentally observed behavior.

Comparing the data for the dihedral blade configurations with the radial blades, the blade outlet angles (Figures 35 and 36) show less flow turning and the pressure coefficient plots (Figures 37 through 46) indicate lower lift coefficients with dihedral. Both of these trends are proportional to increasing dihedral angle, and indicate a reduction of blade performance with increasing dihedral angle. The large flow turning observed for the radial blade near the root, particularly for the $\phi = 0.130$ case, diminished significantly for $\mu = -15^{\circ}$ and nearly disappeared for $\mu = -30^{\circ}$, which is consistent with the blade unloading phenomenon. As with the radial blade data, the outlet angle measurements are somewhat unreliable and hence the pressure coefficient data has been primarily relied upon for the purpose of interpretation of the data.

Although the pressure coefficient data for both dihedral angles measured consistently indicates a reduction of blade performance at each radial position, the data for the tip regions is suspect. The two tip sections at which measurements were made ($\eta = 0.861$ and 0.981) exhibit rather unusually shaped pressure distributions. This is particularly evident aft of the mid chord point for $\mu = -30^{\circ}$, where the distribution becomes flat and the circulation goes almost to zero. This is probably due to the tip clearance losses caused by the test hardware which were discussed in section 3.2.2, and therefore data near the tip for the dihedral configurations should be viewed with great caution. The dihedral effect for the tip data presented is probably obscured by tip losses and indicates greater loss of performance than would actually occur in a turbomachine due to the dihedral effects.

The effect of dihedral angle on the section lift coefficient is summarized in Figure 47 which is derived from measurements of the areas under the experimental pressure coefficient plots. The mid radius is least influenced by the increase of dihedral angle. The hub and tip, as would be required to satisfy the potential flow wall boundary condition, show greater lift reductions. The actual magnitude of the tip lift reduction, however, is questionable due to tip losses.

The only previous work done on the effect of dihedral in turbomachinery was a theoretical investigation by Smith and Yeh (33) which developed an approximate method for including the effects of sweep and dihedral in axial flow turbomachinery, although the work concentrated primarily on the effect of sweep. The method is basically a quasi-three-dimensional technique where a two-dimensional blade-to-blade solution is superposed on an axisymmetric solution. Further, the numerical calculations presented are based on a rectilinear cascade of quite a different configuration than that considered here. In view of these differences, no meaningful quantitative comparison may be made. Nevertheless, a general conclusion made by Smith and Yeh regarding the effect of dihedral may be applied here. Due to an increase in the downwash near the leading edge and a decrease near the trailing edge, the effect of dihedral was found to be to reduce the effective camber line of the blade. Hence, a blade with dihedral will perform as if it has less camber than an identical blade installed radially, or with no dihedral. This result agrees with and provides further verification of the qualitative analysis and experimental data put forth above.

So far, all analytical consideration of dihedral effects has been limited to potential flow theory; but real fluid phenomena also enter into the observed behavior of the dihedral blade. Although the topic of this work is potential flow, it is essential to include some consideration of real fluid phenomena in order to isolate the potential flow effects and present a meaningful interpretation of the experimental data. It is known that the boundary layer fluid on a turbomachine blade experiences outward migration due to the centrifugal and Coriolis forces in the radial direction and approximately parallel to the blade surface. When the blade has dihedral, however, the centrifugal and Coriolis forces are still directed radially but they are no longer parallel to the blade surface. Resolving the force vectors into components parallel and normal to the surface of the blade with dihedral, it is evident that the parallel component, although not as great as in the radial case, will again cause migration of the boundary layer from hub to tip (Figure 51). The most significant difference here is the normal components which for a blade with dihedral toward the pressure surface now tend to destabilize the boundary layer on the blade suction surface and aggravate flow separation. The normal component of the Coriolis force tends to stabilize the flow on the pressure side. For dihedral toward the suction surface, the normal component tends to stabilize the boundary layer on the suction surface, but destabilize the pressure surface boundary layer. Thus, since the tendencies of the centrifugal and Coriolis forces and conventional boundary layer growth to cause flow separation are additive on the suction surface for dihedral toward the pressure surface, this case may result in flow separation at any given radial position. Thus the combined viscous and inviscid effects due to dihedral are more detrimental to blade performance. While reducing somewhat the outward migration of boundary layer fluid and the secondary consequence of induced flow separation, the dihedral blade introduces the more unfavorable effect of the direct action of the normal component on the boundary layer separation.

CHAPTER V

CONCLUSIONS

A two-dimensional cascade solution may be a satisfactory approximation of the three-dimensional flow through a turbomachine for some rotor configurations. Typically, such rotors are characterized by a low solidity, large number of blades, high hub/tip radius ratio, low stagger angle, and low blade loading. For rotor configurations not falling within these conditions, a three-dimensional analysis is required.

This work has been an attempt to introduce three-dimensional correction into turbomachinery design and analysis procedure. Although the restriction of constant circulation radially and radial blade mounting are significant practical limitations, the theory has proven useful in defining the general three-dimensional trends and will serve as a basis for further development. For a given blade geometry for which the singularity representation has been determined, the three-dimensional computer program is fast and inexpensive with computer execution time on the order of a few minutes on an IBM 360 computer.

The feasibility of applying the three-dimensional singularity theory to the analysis of the potential flow through a turbomachine has been demonstrated, although further refinement of the technique and more extensive application to other design configurations is necessary before it may be considered to be a practical design tool. A useful extension of this theory would be to allow radially variable vortex strengths. Not only would this enable treatment of much more general radial blade configurations, but it should make possible a further extension of the theory to include non-radial singularity lines. With this added capability, the three-dimensional theory could be used to model straight blades with dihedral as well as sweep. A further useful extension which would include curvilinear singularity lines could allow analysis of curved turbomachinery blading.

Although the basic three-dimensional theory is sound, improved convergence of the numerical solution is a prerequisite to applying the analysis to an actual design process.

A turbomachine blade operating in an actual three-dimensional annular flow field performs differently than predicted by the widely used two-dimensional cascade, or strip theory. The hub regions develop more circulation while the tip regions develop less circulation in the three-dimensional flow than predicted two-dimensionally. Although real fluid effects may contribute to this trend, the three-dimensional potential flow effects are also a significant factor for many rotor configurations. The three dimensional effects are inversely proportional to the hub/tip ratio. Furthermore, the three-dimensional effects are larger near the hub than at the tip. For example, for $\nu = 0.4$, $\eta = 0.4$, $\lambda = 80^\circ$, the ratio $(\Gamma_2 - \Gamma_3)/\Gamma_3$ is 18.75 percent, which is appreciable. From a practical viewpoint, this means that designers, who typically use two-dimensional strip theory for blade layout, must take into account these three-dimensional effects in their designs. In order to achieve the desired circulation at each radial blade section under actual operating conditions, the hub profiles must be designed with less camber and the tip profiles with more camber than predicted using cascade theory.

Near the hub, the two-dimensional theory under predicts and the three-dimensional theory over predicts the lift coefficient as derived from the experimentally measured blade pressure distributions. Near the tip, this trend is reversed and the discrepancy between the two-dimensional theory and the experiment is as much as 60% while that between the three-dimensional theory and the experiment is 20%. The predictions from the three-dimensional theory show better agreement with the experiment throughout and the trend (i.e. higher lift at the hub and lower lift at the tip than two-dimensional values) is correctly predicted.

Check-out of the instrumentation system indicated that the experimentally measured pressure coefficient data agreed with cascade predictions within 5 percent at the mid radius of a radially mounted blade. This good agreement at the mid radius locations between the experimental data and the values predicted by cascade theory, the reliability of which has been well established, provides confidence in the instrumentation. The unique rotating instrumentation system developed for this program is a feasible approach to the measurement of static pressures on a rotating blade.

A blade which is mounted with dihedral toward its pressure surface, which is defined as negative dihedral, produces less lift at each spanwise location than does the identical blade when mounted radially, and this degradation of blade performance is proportional to increasing dihedral angle. Although not investigated experimentally, qualitative analytical study indicates that a similar trend in the variation of lift should exist for positive dihedral toward the suction surface. The effects of dihedral were found to be appreciable.

It is recognized that the experimental method used to achieve blade dihedral may involve some inaccuracy, especially at the tip, but these inaccuracies are not significant enough to account for the large loss in lift observed near the blade tip and root sections. Since there is no previous data available on the effects of dihedral, this approach was pursued to obtain some data using the existing hardware.

The effect of dihedral on blade performance derives from two basic but distinct types of flow phenomena. The boundary conditions imposed on the potential flow solution require a diminishing circulation at the hub and tip to satisfy the wall condition of no normal flow. The real fluid phenomena associated with separation of the boundary layer coupled with components of centrifugal and Coriolis forces normal to the blade surface lead to further deterioration of the blade performance. This condition exists in varying degrees at all radial locations, and is more severe for a negative dihedral angle.

Any future analysis to deal with the effect of blade dihedral on rotor performance should include the following:

1) The constraint and the change in boundary conditions near the hub and tip walls caused by non-radial blades.
2) The effect of radial blade force which serves to disturb the meridional flow and radial equilibrium.
3) The effect of transverse components of centrifugal and Coriolis forces on the blade boundary layer.
4) The effect on wall stall near the hub surface and the accumulation of blade boundary layer near the tip.

REFERENCES

1. D. A. Morelli and R. D. Bowerman, "Pressure Distribution on the Blade of an Axial Flow Propeller Pump," Trans. ASME, Vol. 75, August, 1953, p. 1007-1013.

2. H. Schlichting, Incompressible Flow Through Cascades V. D. I. Forsch. Heft. 447 (1955).

3. N. Scholz, *Aerodynamik der Schaufelgitter* (Verlag G. Braun Karlsruhe, 1965), Vol. I.

4. H. Schlichting, "Application of Boundary Layer Theory in Turbomachinery," Journal of Basic Engineering, Vol. 81D, Nov. 1959, p. 543-551.

5. B. Lakshminarayana and J. H. Horlock, "Review: Secondary Flows and Losses in Cascades and Axial-Flow Turbomachines," Int. J. Mech. Sci., Vol. 5, pp. 287-307, 1963.

6. G. Mellor, "A Combined Theoretical and Empirical Method of Axial Compressor Cascade Prediction," ASME Paper No. 72-WA/GT-5, November, 1972.

7. J. H. Horlock, *Axial Flow Turbines*, Butterworths, London, 1966.

8. J. H. Horlock, *Axial Flow Compressors*, Butterworths, London, 1958.

9. T. Katsanis, "Quasi-Three-Dimensional Calculation of Velocities in Turbomachine Blade Rows," ASME Paper No. 72-WA/GT-7, November, 1972.

10. C. H. Wu, "A General Theory of Three-Dimensional Flow in Subsonic and Supersonic Turbomachines of Axial, Radial, and Mixed Flow Types," NACA TN 2604, 1952.

11. D. J. L. Smith and D. H. Frost, "Calculation of the Flow Past Turbomachine Blades," Paper 27, Axial and Radial Flow Turbomachinery, Institute of Mechanical Engineers (London), 1970, p. 219-231.

12. H. Marsh, "A Digital Computer Program for the Through Flow Fluid Mechanics in an Arbitrary Turbomachine Using a Matrix Method," ARC R&M 3509, 1968.

13. L. H. Smith, Jr., "The Radial Equilibrium Equation of Turbomachinery," Journal of Engineering for Power, Trans. ASME, Series A, Vol. 88, January 1966, p. 1-12.

14. R. A. Novak, "Streamline Curvature Computing Procedures for Fluid-Flow Problems," Journal of Engineering for Power, Trans. ASME, Series A, Vol. 89, October 1967, p. 478-490.

15. J. E. McCune and O. Okurounmu, "Three-Dimensional Vortex Theory of Axial Compressor Blade Rows at Subsonic and Transonic Speeds," AIAA Journal, Vol. 8, No. 7, July, 1970.

16. J. E. McCune, "A Three-Dimensional Theory of Axial Compressor Blade Rows - Applications in Subsonic and Supersonic Flows," Journal of Aerospace Sciences, September 1958.

17. J. E. McCune and J. P. Dharwadkar, "Lifting-Line Theory for Subsonic Axial Compressor Rotors," MIT GTL Report No. 110, July, 1972.

18. H. N. Tyson, Jr., "Three-Dimensional Interference Effect of a Finite Number of Blades in an Axial Flow Turbomachine," Cal Tech Hydrodynamics Lab. Report No. E 19.1, November, 1952.

19. Vernon J. Rossow, "An Analysis of the Error Involved in Unrolling the Flow Field in Turbine Problem," Mitt. Aus. Dem. Inst. Aerodynamik (E. T. H., Zurich) Report 23, 1957 (publisher, Verlag Leeman, Zurich).

20. A. Tamura and B. Lakshminarayana, "Three-Dimensional Flow Field Due to a Vortex and Source Spanning an Annulus," Int. J. Engr. Sci., Vol. 13, 1975, p. 549-561.

21. A. Tamura and B. Lakshminarayana, "Assessment of Three-Dimensional Inviscid Effects in Turbomachinery Using Simple Models," ASME Paper 75 WA/FE8 (To be published in J. Fluids Engineering).

22. P. C. Pien, "The Calculation of Marine Propellers Based on Lifting-Surface Theory," J. Ship Research, Vol. 5, No. 2, 1961, p. 1-14.

23. J. P. Geising, "Extension of Douglas Neumann Problems of Lifting, Infinite Cascade," Douglas Aircraft Co. Report LB31653, July 2, 1964.

24. R. D. Bowerman, "The Design of Axial Flow Pumps," Trans. ASME, Vol. 78, November, 1956, p. 1723-1734.

25. J. McMahon, "On the Roots of Bessel and Certain Related Functions," Annals of Math, Vol. 9, 1894, p. 23.

26. A. Tamura, R. Howells and B. Lakshminarayana, "Three-Dimensional Potential Flow Around a Body Spanning an Annulus: Computer Program and Solution," Applied Research Laboratory, The Pennsylvania State University, Technical Memo 73-173, 1973.

27. R. J. Etter and P. VanDyke, "Three-Dimensional Flow Field from a Radial Vortex Filament in a Cylindrical Annulus," Hydronautics Technical Report 703-7, December 1969.

28. V. M. Falkner, "The Calculation of Aerodynamic Loading on Surfaces of Any Shape," ARC Reports and Memoranda No. 1910, August 26, 1943.

29. E. P. Bruce, "The ARL Axial Flow Research Fan - A New Facility For Investigation of Time Dependent Flows," ASME Paper 74-FE-27, 1974.

30. W. R. Hawthorne (editor), Aerodynamics of Turbines and Compressors, Princeton University Press, Vol. 10, 1964.

31. G. Wislicenus, The Fluid Mechanics of Turbomachinery, Dover, New York, 1965, p. 567-578.

32. R. Howells and B. Lakshminarayana, "Instrumentation for Measuring Steady-State Static Pressure on a Rotating Blade in the Axial Flow Research Fan," The Pennsylvania State University, Applied Research Laboratory, TM 74-201, June 25, 1974.

33. L. H. Smith, Jr. and H. Yeh, "Sweep and Dihedral Effects in Axial Flow Turbomachinery," Journal of Basic Engineering, Transactions of ASME, Series D, Vol. 75, 1963, p. 401-416.

34. B. Lakshminarayana, "Methods of Predicting the Tip Clearance Effects in Axial Flow Turbomachinery," Journal of Basic Engineering, Transactions of ASME, September 1970, p. 467-482.

35. M. Oshima, H. Endoh, T. Gotoh, N. Koyama, and Y. Tamura, "Blade Characteristics of Axial-Flow Propellers", Second International JSME Symposium on Fluid Machinery and Fluidics, Tokyo, Vol. I, September 1972.

36. R. A. Cumming, W. B. Morgan, and R. J. Boswell, "Highly Skewed Propellers", Trans. Soc. Naval Architects and Marine Engineers, Vol. 80, 1972.

APPENDIX

Variation of Singularity Position Between Two- and Three-Dimensional Discrete Representation

To calculate the relationship of the strength of the two- and three-dimensional discrete singularity representations in Paragraph 2.3.1, the assumption was made that, in both cases, the singularities were located along the same camber line. Only the strength of the discrete singularities was allowed to vary between the two- and three-dimensional cases. However, from previous work, it was shown that in actuality not only the strengths but also the camber line shape were different. Hence, the error introduced by the above assumption must be investigated.

The geometric relationship of a typical two and three-dimensional camber line at zero stagger is depicted in Figure 52a. The velocity perturbation induced at a point $x = \ell$ on the camber line by a discrete vortex at a point $x = j$, for example, may be expressed as

$$\left|\underline{U}_v\right|_2 = \frac{\Gamma_j}{2\pi r} \tag{A1}$$

and

$$\left|\underline{U}_v\right|_3 = \frac{\Gamma_j}{2\pi(r+dr)} \tag{A2a}$$

for the two- and three-dimensional cases, respectively. Also, it has been assumed for simplicity that $\Gamma_j = (\Gamma_j)_2 = (\Gamma_j)_3$. Rearranging, Equation A2a becomes,

$$\left|\underline{U}_v\right|_3 = \frac{\Gamma_j}{2\pi r\,(1 + \frac{dr}{r})}$$

$$= \frac{\Gamma_j}{2\pi r}\,(1 - \frac{dr}{r}) \quad . \tag{A2b}$$

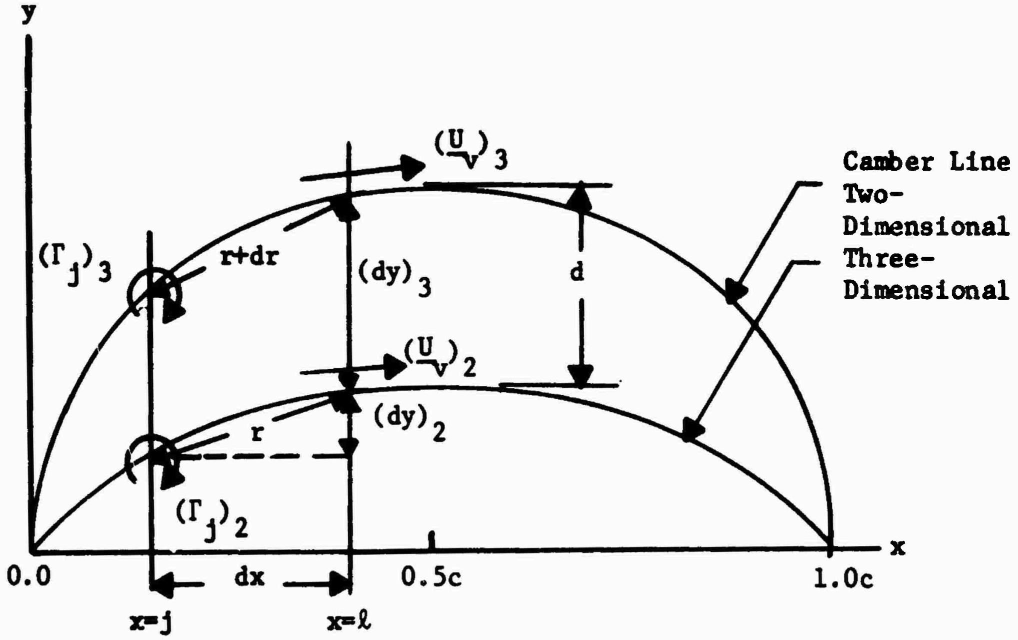

a. Geometrical Relationship of Typical Two- and Three-Dimensional Camber Lines at Zero Stagger (Descrepancy Exaggerated for Clarity)

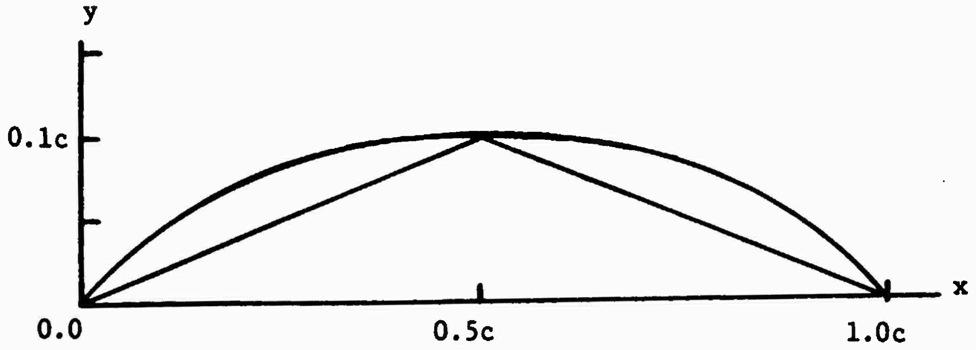

b. Camber Line Slope Estimation for 10% Camber.

Figure 52. Estimation of the Error Introduced by Assuming the Discrete Vortices to be Co-Located in the Two- and Three-Dimensional Flow Fields.

Comparing Equations A1 and A2b, the actual difference between the two- and three-dimensional induced velocity perturbations is (dr/r). Consequently, the error in the induced velocity introduced by assuming the two- and three-dimensional camber lines to the same is O(dr/r).

To investigate the order of magnitude of dr/r, it follows that,

$$r = [dx^2 + (dy)^2_2]^{1/2} = dx\,[1 + (\frac{dy}{dx})^2_2]^{1/2}$$

and

$$r + dr = [dx^2 + (dy)^2_3]^{1/2} = dx\,[1 + (\frac{dy}{dx})^2_3]^{1/2} .$$

Substituting

$$\frac{dr}{r} = \frac{(r+dr) - r}{r}$$

$$= \frac{dx\{[1 + (\frac{dy}{dx})^2_3]^{1/2} - [1 + (\frac{dy}{dx})^2_2]^{1/2}\}}{dx[1 + (\frac{dy}{dx})^2_2]^{1/2}}$$

$$= \frac{[1 + (\frac{dy}{dx})^2_3]^{1/2}}{[1 + (\frac{dy}{dx})^2_2]^{1/2}} - 1$$

$$= [1 + \frac{1}{2}(\frac{dy}{dx})^2_3][1 - \frac{1}{2}(\frac{dy}{dx})^2_2] - 1$$

$$= [1 - \frac{1}{2}(\frac{dy}{dx})^2_2 + \frac{1}{2}(\frac{dy}{dx})^2_3 - \frac{1}{4}(\frac{dy}{dx})^2_3(\frac{dy}{dx})^2_2 - 1]$$

$$\simeq \frac{1}{2}[(\frac{dy}{dx})^2_3 - (\frac{dy}{dx})^2_2] ,$$

where second order terms have been neglected. Then rearranging,

$$\frac{dr}{r} \simeq \frac{1}{2} \left(\frac{dy}{dx}\right)_3^2 [\ 1 - K\ ] \text{ where } K = \frac{(dy/dx)_2^2}{(dy/dx)_3^2} .$$

Assuming a 10% camber, for example, then the camber line slope may be approximated by

$$\left(\frac{dy}{dx}\right)_3 = \frac{0.1\ c}{0.5\ c} = 0.2$$

except very near the leading edge (Figure 52b). Therefore,

$$\frac{dr}{r} \simeq \frac{1}{2} (0.2)^2\ [K - 1]$$

$$\simeq 0.02\ [K - 1] .$$

From several numerical calculations, typically

$$K \sim 0\ (1 \pm 0.5)$$

and then,

$$\frac{dr}{r} \simeq 0.02\ [1 \pm 0.5 - 1]$$

$$\simeq \pm 0.010 .$$

Hence, the positional variation between the two- and three-dimensional theories is of the order of one percent and is negligible as far as the calculation of the induced velocity perturbation is concerned. When analyzing the geometric variation of the camber lines, however, the difference between the two- and three-dimensional cases is not, in general, negligible.